工学博士学位論文

Theoretical study on electronic states of magnetic layered semiconductors MPS_3

磁性層状半導体「遷移金属・リン・トリカルコゲナイド」

の電子状態の理論的研究

筑波大学大学院　博士課程
工学研究科　物質工学専攻

栗田　典之

昭和６３年　１２月

Contents

Chapter 1. Introduction

Recently, many kinds of interesting multi-component compounds have been investigated experimentally. These are, for example, intercalated compounds, perovskite-type compounds such as the high-Tc oxide superconductors and various transition metal compounds. Among them, transition metal chalcogeno-phosphates MPX_3(M stands for a 3d transition metal and X is either sulfur or selenium) form a large family of layered semiconducting compounds with very interesting properties. In particular, the magnetic property and the intercalation of MPX_3 are attractive to many researchers for both academic and technological reasons:[1] (a)The magnetic structure and spin ordering direction change with the transition metal element. (b)The intercalation capacity changes with the transition metal element. In particular, $NiPS_3$ and $FePS_3$ can be a good candidate for a Li-based battery, since they show a substantially high capacity for the uptake of lithium.

The band structures of these materials are essential to understand their basic physical properties. In particular, the charge redistribution among each atom seems important in these multi-component compounds. It is well known that the self-consistent liner combinations of atomic orbitals(LCAO) method is very useful for studying the charge transfer between atoms. Nevertheless, these compounds have complex structures and contain many heavy atoms, so that it is difficult to calculate the band structures by the usual LCAO method, that is, the necessary number of the matrix elements is so large that they can not be calculated within a practical computational time.

In order to overcome this difficulty, we develop a new method for such calculations.[2] The main feature of the method is the use of the norm-conserving pseudopotential, the numerical-basis-set LCAO method and the Gaussian-fitting of basis functions and crystal potential. By using the above three techniques, the number of the matrix elements is reduced, and most of them come to be calculated analytically. As a result, it becomes able to calculate the self-consistent band structure of such a complex crystal as MPX_3 without an enormous computational time.[3-5]

The imaginary part of the dielectric function $\varepsilon_2(\omega)$ is also calculated, and it is clarified that $ZnPS_3$ and $MnPS_3$ are almost isotropic in the layer, while $NiPS_3$ and $FePS_3$ are anisotropic. Furthermore, the calculated $\varepsilon_2(\omega)$ spectrum for the light polarized parallel to the layer reproduces the main features of the observed optical spectrum in the low energy region.

From the calculation of the total energies of some types of magnetic structures of $NiPS_3$ and $MnPS_3$, it is proved that the triangularly coupled magnetic structure (the experimentally observed one) is more stable than the linearly coupled one for $MnPS_3$, and that the linearly coupled magnetic structure (the experimental one) is more stable in $NiPS_3$.

By comparing the calculated band structures of MPS_3 family(M= Zn, Ni, Mn, Fe), it is found that $NiPS_3$ and $FePS_3$ are more active to the lithium intercalation than $MnPS_3$ and $ZnPS_3$, and that $NiPS_3$ is the best cathode material in secondary lithium batteries in the MPS_3 family.

In the next chapter, the various properties of MPX_3 are described. The calculating procedure is described in detail in chapter 3. The calculated results for the MPS_3 family are given in chapter 4, and their physical properties are discussed from these results in chapter 5. The conclusions of this study are given in chapter 6.

Chapter 2. Magnetic layered semiconductors MPX_3

§ 2-1. Introduction

The transition metal chalcogeno-phosphates MPX_3 form a large family of layered semiconducting compounds with very interesting properties. In particular, the magnetic property and the intercalation of MPX_3 are attractive to many researchers.[1)]

In order to investigate the above properties, the knowledge of the electronic states of MPX_3 is indispensable. A semiempirical energy level scheme was proposed from experiments.[6-9)] Furthermore, simple band calculations were performed based on the extended Hückel method.[10,11)] However, the above two simple pictures are not enough to investigate the properties of MPX_3.

In this chapter, we first describe their magnetic properties, intercalation capacities and availabilities for a cathode material in secondary lithium batteries. And then, their electronic and optical properties are described.

§ 2-2. Magnetic properties of MPX_3

The MPS_3 compounds crystallize to a monoclinic structure (its space group C2/m), and their lattice parameters are shown in Table 2-1.[12-14] This crystal structure is related to that of titanium disulfide(TiS_2) with metal(M) ions and phosphorus-phosphorus pairs (P_2) occupying the titanium sites, as shown in Fig.2-1.

A family of MPX_3(except $ZnPS_3$ and $ZnPSe_3$) is antiferromagnetic, and their Neel temperatures are listed in Table 2-2.[15] It is interesting that their magnetic structures and spin ordering directions change with the transition metal element:[16-18] (1)The magnetic ions having the same spin are triangularly coupled each other in $MnPS_3$, while they are linearly coupled in $FePS_3$, $NiPS_3$ and $CoPS_3$. (2) The spin easy axis is perpendicular to the layer in $MnPS_3$, $NiPS_3$, $FePS_3$ and $FePSe_3$, while it is parallel in $CoPS_3$ and $MnPSe_3$. The experimentally observed three-dimensional magnetic structures are shown in Fig.2-2.[1] The two-dimensional magnetic structure of $FePS_3$ is the same as those of $NiPS_3$ and $CoPS_3$. However, in $FePS_3$, the chains of a plane are antiferromagnetically coupled to the ones in the neighboring planes, implying a doubling of the c parameter of the magnetic cell (Fig.2-2(c)). Moreover, the magnetic property of MPX_3 is dramatically changed by the intercalation.[15,19]

In this study, in order to investigate the stability of magnetic structures, three types of two-dimensional magnetic structures are assumed, which are shown in Fig.2-3. The structure of type 1 consists of magnetic

ions coupled antiferromagnetically to each nearest neighbor ion(Fig.2-3(a)). The magnetic structure of $MnPS_3$ is of this type. In $FePS_3$, $NiPS_3$ and $CoPS_3$, the magnetic ions distribute as for type 2, which consists of double parallel ferromagnetic chains coupled to each other antiferromagnetically (Fig.2-3(b)). The structure of type 3 is artificial and a little different from that of type 2. In type 2 the direction of the ferromagnetic chains is parallel to the **a** axis; but in type 3 it is not parallel (Fig.2-3(c)). In other words, the magnetic ions having the same spin are triangularly coupled each other in the type 1 magnetic structure; they are linearly coupled in types 2 and 3. The three types of the two-dimensional Brillouin zones corresponding to the above magnetic structures are shown in Fig.2-4.

For the spin polarizations of the P and S ions, the following properties are expected from the symmetry of these magnetic structures:(1) in type 1, P and S ions have no spin polarization. (2) in type 2, P ion and S_1 ion surrounded by up-spin M, down-spin M and P_2, have no spin polarization. Other two S ions (S_2 and S_3) are surrounded by the two M ions with the same spin and P_2, so they have spin polarization. (3) In type 3, P and S_1 ions have no spin polarization, but other S ions have.

2-3. Intercalation properties of MPX_3

A family of MPX_3 has a layered structure (Fig.2-1) and can intercalate kali ions or molecules in its van der Waals gap. Since $FePS_3$ and $NiPS_3$ ow a substantially high capacity for the uptake of lithium, they can be a od candidate for a Li-based battery : $NiPS_3$ reacts with more than four thiums, resulting in a cell with a theoretical energy density double that TiS_2.[20] It is also interesting that the intercalation capacity of MPX_3 anges with the transition metal element. For example, in the case of emical intercalation, $NiPS_3$ is the most active material, while $ZnPS_3$ is mpletely inert.[21] Their different behavior with respect to the tercalation is related to the degree of ionicity of the transition metal ement and depends strongly on the number of available d states.[22]

As for the intercalation capacity, it has been found[15] that tercalated lithiums are in octahedral sites of the van der Waals gap as $^+$ ions, and the electrons given up to MPS_3 are donated to conduction bands MPS_3. Thus, the process of lithium intercalation into MPS_3 is ergetically favorable only in the case where unoccupied bands of MPS_3 are a sufficiently low energy to readily accommodate additional electrons.

From a simple energy diagram[22] (Fig.2-5), the smaller the band gap E_G lue is, the larger the potential difference E_{INT} is, where E_{INT} is defined the difference between the highest occupied level of a Li atom and the cepting level of MPS_3. In other words, the smaller the E_G value is, the

larger the formation energy for the lithium intercalation is; the higher the intercalation capacity is.

As for the availability of MPS_3 for a cathode material of a Li-based battery, a number of authors[20,23] have proposed the following key requirements for a useful cathode material that might react with lithium by the reversible reaction ; $xLi + MPS_3 \rightleftarrows Li_xMPS_3$.

(1) Large and constant free energy of reaction (affording a high and constant cell voltage).

(2) Good electronic conductivity (to minimize resistive heat generation and eliminate the need for a conductive additive in the electrode).

(3) High diffusibility of Li ions into MPS_3 (allowing a high power density).

(4) Wide range of x-values (resulting in a high cell capacity).

(5) Minimal structural change on reaction (resulting in a reversible reaction).

Furthermore, Thompson and Whittingham[20] have found that $NiPS_3$ reacts with more than four lithiums, resulting in a cell with a theoretical energy density double that of TiS_2. And they have expected that the Li-$NiPS_3$ battery will be a promising candidate for electric vehicle propulsion, if its high energy density is truly electrochemically reversible.

§ 2-4. Electronic and optical properties of MPX_3

§ 2-4-1. Experimental results

The variations of resistivity ρ parallel to the layers with temperature for $NiPS_3$ and $FePS_3$ were measured.[24] For $NiPS_3$, assuming a dependence of the form: $\rho = \rho_0 \exp(E/2kT)$, the value of the energy gap E was found to be 1.59±0.05 eV. This implies that $NiPS_3$ behaves as an intrinsic semiconductor. At room temperature the value of ρ_{300} is about 1×10^{11} Ωcm. On the other hand, the resistivity of $FePS_3$ is of the order of 10^5 Ωcm, varying somewhat from sample to sample, but with no temperature dependence.

Furthermore, Brec et al.[21] made dc electrical-conductivity measurements parallel to the layers, on $MnPSe_3$, $NiPS_3$, $FePS_3$ and $FePSe_3$ crystals, and on their lithium intercalated products. The crystals of $NiPS_3$ and $MnPSe_3$ had extremely high resistances (about 10^9 Ωcm) whereas those of $FePS_3$ and $FePSe_3$ had values of between 10^4 and 10^5 Ωcm. The electrical behavior of the intercalated products appears as three general categories: (a)For $MnPSe_3$, no increase in the conductivity is observed(therefore the number of electrical carriers remains very low). (b)For $FePS_3$ and $FePSe_3$, a gradual increase in the number of carriers is observed. (c)For $NiPS_3$, the number of carriers increases rapidly, resulting in the metallike behavior of Li_xNiPS_3.

Optical absorption measurements were performed on single crystals of $NiPS_3$, $FePS_3$, $FePSe_3$, $MnPS_3$, $MnPSe_3$, $ZnPS_3$ and $CdPS_3$.[21] All members of these compounds are broad band semiconductors, whose gap values are given in Table 2-3. Furthermore, in most of these compounds, there are rather intense d-d transitions which occur close to the fundamental absorption edge.

The band structures of MPX_3 are essential for investigating their properties, but they have not yet been calculated because of their complex crystal structures. Piacentini et al.[6,7] measured some optical properties (the optical absorption below the fundamental threshold, the normal-incidence reflectivity between 1.5 and 30 eV and the X-ray photoemission spectra) of $FePS_3$, $NiPS_3$ and $ZnPS_3$, and proposed a semiempirical energy level scheme, which is based on the single-layer approximation and on an ionic model[8] for these compounds: $M_2^{2+}(P_2S_6)^{4-}$. In this model, the $(P_2S_6)^{4-}$ cluster and the M^{2+} ion are treated separately. For the $(P_2S_6)^{4-}$ cluster, the energy levels of the symmetrized combinations of the P 3s and 3p states and the S 3s and 3p states are obtained from the comparison with the valence band X-ray photoemission spectra. For the M^{2+} ion, its 3d orbitals are viewed as localized and not bonded with other orbitals, and their energy levels are placed near the Fermi level, since they are partly empty (except Zn). The M^{2+} 4s and 4p orbitals are not included in this energy level scheme. Although this approach gave a reliable sequence of the valence band states, it could not give an accurate description of the localized M^{2+} 3d states and of the lower conduction band states. It is also proposed by

Khumalo and Hughes[8] that the lower conduction bands originate primarily from the M^{2+} 4s and 4p states and the P and S $3p_z$ states. On the other hand, in order to investigate the lowest conduction band, Piacentini et al.[9] measured the soft X-ray absorption spectra of $FePS_3$ and $NiPS_3$, and concluded that the lowest conduction band in $FePS_3$ and $NiPS_3$ is formed mostly by the P 3s antibonding states, which is different from the previous model.[8] After all, the accurate band structures of MPX_3 family are indispensable.

§ 2-4-2. Simple band calculations

Recently, in order to clarify the nature of the electron accepting levels in MPS_3, the electronic band structures of MPS_3 family (M= Fe, Ni, Mn, Cd and Co) were calculated employing the tight-binding band scheme, based upon the extended Hückel method, and their density of states were also calculated by employing the special k-point method.[10,11] The low lying parts of $MnPS_3$, $FePS_3$ and $NiPS_3$ are shown in Fig.2-6 (after ref.1).

The component analysis shows that: (1)Peak A is identified as the valence band of $(P_2S_6)^{4-}$ ions. (2)Peak B is largely composed of M 3d orbitals and considered as the t_{2g} subband. (3)Peak C, in which sulfur 3p orbital character is nearly as large as the M 3d contribution, is assigned to the e_g subband and is the first low lying partially filled level in $NiPS_3$. (4)A small peak above peak B in $NiPS_3$ is a bonding contribution of the P-P type. (5)The M 4s and 4p orbitals are situated at about 12 eV above the M 3d t_{2g} orbitals. (6)The 3s orbitals of sulfur and phosphorus contribute to the peaks that occur in the energy region below peak A. From this analysis, it was clarified that the accepting levels in $NiPS_3$ are constituted by the e_g subband, while those in $FePS_3$ and $MnPS_3$ are constituted by the t_{2g} subband which has a strong M 3d character.

§ 2-4-3. Problems in simple band calculations

Although the results of the above simple band calculations are compatible with the experimental results, there are some problems in these simple calculations. The spin-dependence of transition metal 3d bands must be considered, since it is essential for investigating the properties of magnetic materials. That is, for magnetic materials, the M 3d states lie near the band gap and strongly affect their properties; optical properties in low energy region, magnetic and intercalation properties. Furthermore, the above calculation is semiempirical and not self-consistent. Thus, it is not enough to investigate the properties of MPX_3, and the spin-dependent and ab-initio self-consistent band calculation is indispensable in order to get the accurate band structures of MPX_3 family.

Chapter 3. Methodology of a band calculation

§ 3-1. Introduction

The method of linear combinations of atomic orbitals(LCAO) has been shown to be very successful in band structure calculations. The essential key to this success is the ability to calculate the crystal potential accurately, that is, any artificial assumption such as muffin-tin potential is not necessary in the LCAO method. However, many atomic orbitals are needed for expressing the extended states, and a huge computational time is required for the accurate band structure calculation.

A new self-consistent technique in the LCAO method was proposed by Zunger and Freeman in the local density functional(LDF) formalism.[25] In this method, various contrivances, such as the optimization of basis functions, are introduced so as to obtain the reliable result even by using a rather small set of basis functions.

Recently, many kinds of interesting multi-component compounds have been investigated experimentally. For these compounds, the charge redistribution among each component atom seems important to understand their physical properties, and the self-consistent LCAO method is very useful for studying the charge redistribution. However, since these compounds have complex structures and contain many heavy atoms, it is still difficult to calculate the band structures, even if the method of Zunger and Freeman is employed.

In this study, we develop a new procedure of the self-consistent calculation which is adequate for the calculation of the band structure of

the complex crystal.[2] Referring to the procedure for the calculation of the electronic structure of a large-sized cluster,[26] we use three techniques in order to abbreviate a computational time. First, we use the first-principle, norm-conserving pseudopotential proposed by Bachelet et al.[27] to eliminate the effect of the core electrons on the valence electrons. Secondly, in the LCAO method, considering the charge redistribution among each component atom, we expand the crystal wavefunction in terms of numerical ionic-like orbitals rather than atomic ones. And then, these basis functions are fitted by Gaussian-type functions. The crystal potential is also expressed by the sum of Gaussian-fitted atomic-like potentials and a smooth periodic potential. As a result, most of the matrix elements come to be calculated analytically, so that a computational time is abbreviated very much.

In the following of this chapter, we first describe the main features of the method, and then we explain the overall flow of the calculational procedure and the method of a total energy calculation.

§ 3-2. Norm-conserving pseudopotential

The LDF formalism allows us an a priori treatment of the inhomogeneous interacting electron system, in which the effective potential acting on the electron is a function of the electron charge density. By using a pseudopotential in this formalism, we obtain an effective one-electron equation of the following form in Rydberg atomic unit

$$\left\{-\nabla^2+\sum_{\alpha,m} V_{ps}^{\alpha}(r-R_m-d_\alpha)+2\int \frac{\rho_{val}(r')}{|r-r'|}\,dr'+V_{xc}[\rho_{val}(r)]\right\}\Psi_j(k,r)$$

$$= E_j(k)\Psi_j(k,r). \quad (3.1)$$

Here $V_{ps}^{\alpha}(r-R_m-d_\alpha)$ means a pseudopotential of the atom situated at the site R_m+d_α, where R_m and d_α are the position vectors of the mth unit cell and the αth atomic sublattice site respectively, and $V_{xc}[\rho_{val}(r)]$ means an exchange-correlation potential. It is noted that the valence charge density $\rho_{val}(r)$ appears alone in eq.(3.1) and that it is related to the eigenfunctions $\Psi_j(k,r)$ by

$$\rho_{val}(r)=\frac{\Omega}{(2\pi)^3}\sum_{j}^{val}\int_{BZ}\Psi_j^*(k,r)\Psi_j(k,r)dk\ , \quad (3.2)$$

where the summation extends over the valence states and the integral is performed over the Brillouin zone(BZ) and Ω denotes the crystal volume. The

effective one-electron equation(3.1) is therefore to be solved self-consistently, that is , the Hartree and exchange-correlation potentials on the left-hand side of eq.(3.1) are consistently determined from the resulting valence charge density.

For the pseudopotential we use the norm-conserving pseudopotential presented by Bachelet et al.[27] There are two reasons to use it: (1)It has the norm-conserving property, that is, the pseudo wavefunction for the atom is identical to the true valence wavefunction beyond some core radius. This property is required in a self-consistent calculation. In particular, this is essential in the LDF formalism, because the potential is determined by the charge density evaluated from wavefunctions. (2)It is expressed in terms of analytic functions in the real space and useful in an analytic calculation of matrix elements. The total ionic pseudopotential is written as

$$V_{ps}^{ion}(r)= \sum_{l} |l\rangle [\, V_l^{ion}(r) + V_l^{so}(r) L\cdot S \,] \langle l| \quad , \tag{3.3}$$

where $V_l^{so}(r)$ describes the strength of spin-orbit interaction. We decompose $V_l^{ion}(r)$ into two parts; one is an l-independent long-range Coulomb part which originates from the effective core charge, and the other is an l-dependent short-range Coulomb part. Therefore , we have

$$V_l^{ion}(r) = V_{core}(r) + \Delta V_{ps}^{l}(r) \quad . \tag{3.4}$$

Both of $V_{core}(r)$ and $\Delta V_{ps}^{l}(r)$ are obtained numerically by solving the Dirac equation directly. For the sake of facilitating their use, the pseudopotentials are approximated at high-precision with a few analytic functions, such as error function and Gaussian-type function:

$$V_{core}(r) = -\frac{Z_v}{r}\left[\sum_{i=1}^{2} C_i^{core}\ \mathrm{erf}(\sqrt{\alpha_i^{core}}\ r)\right] , \qquad (3.5)$$

$$\Delta V_{ps}^{l}(r) = \sum_{i=1}^{3} (A_i^l + r^2 A_{i+3}^l)\ \exp(-\alpha_i^l\ r^2) , \qquad (3.6)$$

where Z_v is a valence charge. The spin-orbit interaction $V_l^{so}(r)$ in eq.(3.3) is also expressed as eq.(3.6). The fitting parameters in eqs.(3.5) and (3.6) for Zn, Ni, Mn, Fe, P and S atoms are given in Table 3-1, with those for $V_l^{so}(r)$. The energy eigenvalues of the pseudo atom agree with those calculated for the full-electron atom in the error of less than 1%.

As shown in Fig.3-1, the size of $V_l^{so}(r)$ is much smaller than that of $\Delta V_{ps}^{l}(r)$, so the spin-orbit interaction is neglected in the present calculation.

The exchange-correlation potential can be written as

$$V_{xc}[\rho] = \varepsilon_{xc}[\rho] - \frac{r_s}{3}\frac{d\varepsilon_{xc}[\rho]}{dr_s} , \qquad (3.7)$$

where r_s is related to the charge density through

$$[\rho(r)]^{-1} = \frac{4\pi}{3} r_s^3 \ , \tag{3.8}$$

and $\varepsilon_{xc}[\rho]$ is the exchange-correlation energy per an electron of a homogeneous system with an electron density $\rho(r)$.

In magnetic materials, the spin-polarization exists, and the spin dependency of the exchange-correlation potential must be considered:

$$\varepsilon_{xc}[\rho] = \varepsilon_{xc}^{\sigma}[\rho,\zeta] \ , \tag{3.9}$$

$$\zeta(r) = \frac{\rho^{+}(r) - \rho^{-}(r)}{\rho(r)} \ , \tag{3.10}$$

where $\rho^{+}(r)$ and $\rho^{-}(r)$ are the up- and down-spin electron densities, respectively, and the spin is denoted by σ.

As for the $\varepsilon_{xc}^{\sigma}[\rho,\zeta]$ function, we use the result of Ceperley and Alder[28] as parameterized by Perdew and Zunger,[29] since it is the same one that used in calculating the pseudopotential by Bachelet et al. The result is

$$\varepsilon_{xc}^{\sigma}[\rho,\zeta] = \varepsilon_{x}^{\sigma}[\rho,\zeta] + \varepsilon_{c}^{\sigma}[\rho,\zeta] \ , \tag{3.11}$$

$$\varepsilon_x^{\sigma}[\rho,\zeta] = -\frac{0.9164}{r_s}\left[\frac{2\,\rho^{\sigma}(r)}{\rho(r)}\right]^{1/3}, \tag{3.12}$$

$$\varepsilon_c^{\sigma}[\rho,\zeta] = \varepsilon_c^{U}(\rho) + f(\zeta)[\varepsilon_c^{P}(\rho) - \varepsilon_c^{U}(\rho)], \tag{3.13}$$

where

$$f(\zeta) = \frac{(1+\zeta)^{4/3}+(1+\zeta)^{4/3}-2}{2^{4/3}-2}, \tag{3.14}$$

and the superscripts U and P mean unpolarized (ζ=0) and polarized (ζ=1), respectively. The $\varepsilon_c^i(\rho)$ (i= U or P) is given by using r_s as

$$\varepsilon_c^i(\rho)\begin{cases} = \gamma_i/(1+\beta_1^i\sqrt{r_s}+\beta_2^i r_s) & \text{for } r_s \geq 1, \quad (3.15) \\ = A_i \ln r_s + B_i + C_i r_s \ln r_s + D_i r_s & \text{for } r_s \leq 1, \quad (3.16) \end{cases}$$

where the values of parameters are listed in Table 3-2.

§ 3-3. Numerical-basis-set LCAO method

In order to solve the effective one-electron equation(3.1), the crystal eigenfunction $\Psi_j(k,r)$ is expanded in terms of Bloch functions $\Phi_{\lambda\alpha}(k,r)$ in a standard form:

$$\Psi_j(k,r)=\sum_{\alpha=1}^{s}\sum_{\lambda=1}^{\mu} C_{j,\lambda\alpha}(k)\ \Phi_{\lambda\alpha}(k,r)\ , \tag{3.17}$$

where $\Phi_{\lambda\alpha}(k,r)$ is defined in terms of the λth basis orbital $\chi_\lambda^\alpha(r)$ situated at the site R_m+d_α :

$$\Phi_{\lambda\alpha}(k,r)=\frac{1}{\sqrt{N}}\sum_{m=1}^{N}\exp(ik\cdot R_m)\ \chi_\lambda^\alpha(r-R_m-d_\alpha)\ . \tag{3.18}$$

A central problem is the choice of optimum basis orbitals.

A usual LCAO method, in which atomic orbitals are used as basis orbitals, is not adequate for the accurate band structure calculation, because many atomic orbitals are needed for expressing the extended states. A numerical-basis-set LCAO method proposed by Zunger and Freeman[25] has overcome this problem. In this method, the basis functions are optimized to be consistent with the corresponding charge density, and the reliable result is shown to be obtained even by using a rather small set of the optimized basis functions.

The numerical basis functions are determined by the following equation in the LDF formalism:

$$\{-\nabla^2 + V_{ps}^{\alpha}(r) + 2\int \frac{\rho_M^{\alpha}(r')}{|r-r'|}\,dr' + V_{xc}[\rho_M^{\alpha}(r)]\}\,\chi_{\lambda}^{\alpha}(r) = \varepsilon_{\lambda}^{\alpha}\,\chi_{\lambda}^{\alpha}(r) \quad (3.19)$$

where $\rho_M^{\alpha}(r)$ is an allotted portion of the valence charge density $\rho_{val}(r)$ on the αth atom. The concrete form of $\rho_M^{\alpha}(r)$ used in the present procedure is given later.[eq.(3.23)]

Once the crystal potential and the basis functions are obtained, the usual secular equation

$$\sum_{\lambda=1}^{\mu}\sum_{\alpha=1}^{s}\,[\,H_{\lambda\alpha,\lambda'\alpha'}(k) - S_{\lambda\alpha,\lambda'\alpha'}(k)E_j(k)\,]\,C_{j,\lambda\alpha}(k) = 0 \quad (3.20)$$

is solved, where $H_{\lambda\alpha,\lambda'\alpha'}(k)$ is the Hamiltonian matrix element defined by

$$H_{\lambda\alpha,\lambda'\alpha'}(k) = \langle \Phi_{\lambda\alpha}(k,r)\,|\,H(r)\,|\,\Phi_{\lambda'\alpha'}(k,r)\rangle \quad , \quad (3.21)$$

and $S_{\lambda\alpha,\lambda'\alpha'}(k)$ is the overlap matrix element defined by

$$S_{\lambda\alpha,\lambda'\alpha'}(k) = \langle \Phi_{\lambda\alpha}(k,r)\,|\,\Phi_{\lambda'\alpha'}(k,r)\rangle \quad . \quad (3.22)$$

The solution of the secular equation (3.20) provides us with the eigenvalues $E_j(k)$, the corresponding eigenvectors $C_{j,\lambda\alpha}(k)$ and the eigenfunctions $\Psi_j(k,r)$ which lead to the crystal valence charge density $\rho_{val}(r)$ defined by eq.(3.2), and the Mulliken's charge density

$$\rho_M^{\alpha}(r)= \frac{\Omega}{(2\pi)^3} \sum_{j}^{val} \sum_{\lambda,\lambda'}^{\mu} \sum_{\alpha'}^{s} \int_{BZ} C^{*}_{j,\lambda'\alpha'}(k) S_{\lambda'\alpha',\lambda\alpha}(k) C_{j,\lambda\alpha}(k) \left| \chi_{\lambda}^{\alpha}(r) \right|^2 dk \quad (3.23)$$

where the summation j is carried out over the valence states. This $\rho_M^{\alpha}(r)$ is used in eq.(3.19).

§ 3-4. Calculations of matrix elements

In calculating the matrix elements, eqs.(3.21) and (3.22), we have to carry out a large number of multicenter integrals since the Bloch function $\Phi_{\lambda\alpha}(k,r)$ is expressed in terms of the single-site basis functions $\chi_{\lambda}^{\alpha}(r)$. In order to abbreviate a computational time, we fit them and the crystal potential by Gaussian-type functions and perform these integrals analytically.

§ 3-4-1. Gaussian-fitting of basis functions

The atomic-like numerical basis functions $\chi_{\lambda}^{\alpha}(r)$ is expressed as

$$\chi_{\lambda}^{\alpha}(r) = R_{\lambda}^{\alpha}(r)\, K_{\lambda}^{\alpha}(r) \ , \qquad (3.24)$$

(λ= s, p_x, p_y, p_z, d_{xy}, d_{yz}, d_{zx}, $d_{x^2-y^2}$, $d_{3z^2-r^2}$)

where $K_{\lambda}^{\alpha}(r)$ is a cubic harmonic and $R_{\lambda}^{\alpha}(r)$ is a radial function which is numerically determined by solving eqs.(3.19) and (3.23) self-consistently (using a Herman-Skillman[30] type program).

In the present method, taking into account of the form of $K_{\lambda}^{\alpha}(r)$, we fit $R_{\lambda}^{\alpha}(r)$ as

$$R_{\lambda}^{\alpha}(r) = r^{l} \sum_{n} C_{n}^{\lambda\alpha} \exp[-b_{n}^{\lambda\alpha} r^{2}] \quad , \tag{3.25}$$

where l denotes an angular momentum quantum number and the parameters, $C_{n}^{\lambda\alpha}$ and $b_{n}^{\lambda\alpha}$, are determined by the Statistical Analysis with Least Square fitting (SALS) program.[31] Thus the basis function is expressed as

$$\chi_{\lambda}^{\alpha}(r) = \sum_{n} C_{n}^{\lambda\alpha} G_{\lambda}^{\alpha}(b_{n}^{\lambda\alpha};r) \quad , \tag{3.26}$$

where $G_{\lambda}^{\alpha}(b_{n}^{\lambda\alpha};r)$ is the Gaussian-type function whose concrete form is given in Table 3-3.

As a result of the above technique, the overlap matrix element comes to be calculated as follows

$$S_{\lambda\alpha,\lambda'\alpha'}(k) = \sum_{m} \exp(ik\cdot R_{m}) \sum_{n_1,n_2} C_{n_1}^{\lambda\alpha} C_{n_2}^{\lambda'\alpha'} \int G_{\lambda}^{\alpha}(b_{n_1}^{\lambda\alpha};r-d_{\alpha}) \times G_{\lambda'}^{\alpha'}(b_{n_2}^{\lambda'\alpha'};r-R_{m}-d_{\alpha'})dr \tag{3.27}$$

where the integral is performed analytically as shown in Appendix 1. The matrix element of the kinetic energy $T_{\lambda\alpha,\lambda'\alpha'}(k)$ is also calculated as

$$T_{\lambda\alpha,\lambda'\alpha'}(k) = \sum_{m} \exp(ik\cdot R_{m}) \sum_{n_1,n_2} C_{n_1}^{\lambda\alpha} C_{n_2}^{\lambda'\alpha'} \int G_{\lambda}^{\alpha}(b_{n_1}^{\lambda\alpha};r-d_{\alpha})(-\nabla^{2}) \times G_{\lambda'}^{\alpha'}(b_{n_2}^{\lambda'\alpha'};r-R_{m}-d_{\alpha'})dr \ . \tag{3.28}$$

§ 3-4-2. Gaussian-fitting of crystal potential

In order to calculate the matrix element of the potential energy analytically, we decompose the crystal potential as following;

$$V_{cry}(r) = V_h(r) + \bar{V}_{xc}(r) + \Delta V_{ps}(r) + \Delta V_{coul}(r) \tag{3.29}$$

where each potential is defined by

$$V_h(r) = \sum_{\alpha,m} \left[V_{core}(r-R_m-d_\alpha) + 2A^\alpha \int \frac{\rho_M^\alpha(r'-R_m-d_\alpha)}{|r-r'|} dr' \right], \tag{3.30}$$

$$\bar{V}_{xc}(r) = \sum_{\alpha,m} 2(1-A^\alpha) \int \frac{\rho_M^\alpha(r'-R_m-d_\alpha)}{|r-r'|} dr' + V_{xc}[\rho_{val}(r)] \quad , \tag{3.31}$$

$$\Delta V_{ps}(r) = \sum_{\alpha,m,l} |l\rangle \Delta V_{ps}^l(r-R_m-d_\alpha) \langle l| \quad , \tag{3.32}$$

$$\Delta V_{coul}(r) = 2 \int \frac{\Delta\rho(r')}{|r-r'|} dr' \quad . \tag{3.33}$$

Here A^α is defined by

$$A^\alpha = Z_{val}^\alpha / Q_M^\alpha \tag{3.34}$$

where Z^{α}_{val} and Q^{α}_{M} are the valence charge and the Mulliken's charge of the αth atom respectively, and $\Delta\rho(r)$ is defined by

$$\Delta\rho(r)= \rho_{val}(r)- \sum_{\alpha,m} \rho^{\alpha}_{M}(r-R_{m}-d_{\alpha}) \ . \qquad (3.35)$$

The Mulliken's charge Q^{α}_{M} is determined from eigenvectors and an overlap matrix element as

$$Q^{\alpha}_{M}= \frac{\Omega}{(2\pi)^3} \sum_{j}^{val} \sum_{\lambda,\lambda'}^{\mu} \sum_{\alpha'}^{s} \int_{BZ} C^{*}_{j,\lambda'\alpha'}(k)\, S_{\lambda'\alpha',\lambda\alpha}(k)\, C_{j,\lambda\alpha}(k)\, dk \ . \qquad (3.36)$$

We deal with each potential as follows.

For neutral atoms, the electronic Coulomb potential cancels the core Coulomb potential $V_{core}(r)$ at a moderate distance from the atomic site. However, for ions, the electronic Coulomb potential does not cancel the core Coulomb potential perfectly. Thus, there is a problem how to treat the residual long-range Coulomb potential of each ion in the band structure calculation of ionic crystals. In the present method, as shown in eqs.(3.30) and (3.31), the electronic Coulomb potential of each ion is divided into two parts, so that one part in $V_{h}(r)$ cancels the core Coulomb potential $V_{core}(r)$ at a moderate distance from the atomic site. As a result, each atomic part in $V_{h}(r)$ decreases rapidly with the distance from the atomic site and is easily fitted by Gaussian functions, and thus the matrix element of $V_{h}(r)$ is calculated as

$$\{V_h(r)\}_{\lambda\alpha,\lambda'\alpha'}(k)= \sum_{m} \exp(ik\cdot R_m) \sum_{m',\beta} \sum_{n_1,n_2,n_3} C_{n_1}^{\lambda\alpha} C_{n_2}^{\beta} C_{n_3}^{\lambda'\alpha'}$$

$$\times\int G_{\lambda}^{\alpha}(b_{n_1}^{\lambda\alpha};r-d_{\alpha}) \exp[-b_{n_2}^{\beta}|r-R_{m'}-d_{\beta}|^2] G_{\lambda'}^{\alpha'}(b_{n_3}^{\lambda'\alpha'};r-R_{m'}-d_{\alpha'})dr, \quad (3.37)$$

where the integral is performed analytically as shown in Appendix 1.

The first term on the right-hand side of eq.(3.31) is calculated by using the Ewald summation technique,[32] since it includes the long-range Coulomb potential and the convergence of the lattice summation must be achieved. The second term $V_{xc}[\rho_{val}(r)]$ is a function of $\rho_{val}^{1/3}(r)$ and can not be decomposed into atomic parts, thus we divide $\tilde{V}_{xc}(r)$ into two parts:

$$\tilde{V}_{xc}(r) = \sum_{\alpha,m} V_{xc}^{Atom}(r-R_m-d_{\alpha}) + \Delta V_{xc}(r) \ . \quad (3.38)$$

Here $V_{xc}^{Atom}(r)$ is a short-range potential. We determine it so as to smooth $\Delta V_{xc}(r)$ in the unit cell as possible as we can, and express it in terms of Gaussian functions, so that the matrix element of the first term of eq.(3.38) is calculated analytically in the same way as that of $V_h(r)$.

On the other hand, since $\Delta V_{xc}(r)$ is a rather smooth function of r , it can be expanded in a rapidly convergent Fourier series, viz,

$$\Delta V_{xc}(r)= \sum_{K_v} \exp(iK_v\cdot r)(\Delta V_{xc})_v \ , \quad (3.39)$$

thus the matrix element is calculated as

$$\{\Delta V_{xc}(r)\}_{\lambda\alpha,\lambda'\alpha'}(k)= \sum_{m} \exp(ik\cdot R_m) \sum_{n_1,n_2} C_{n_1}^{\lambda\alpha} C_{n_2}^{\lambda'\alpha'} \sum_{K_v} (\Delta V_{xc})_v$$

$$\times \int G_{\lambda}^{\alpha}(b_{n_1}^{\lambda\alpha};r-d_{\alpha}) \exp(iK_v\cdot r)\ G_{\lambda'}^{\alpha'}(b_{n_2}^{\lambda'\alpha'};r-R_m-d_{\alpha'})dr \quad (3.40)$$

where the analytic result of the integral is given in Appendix 1.

In calculating the matrix element of $\Delta V_{ps}(r)$, we must perform the following integral;

$$F_{l,\lambda}^{\alpha}(r;\ r_1-r_2) = \int K_l^{\alpha}(\widehat{r-r_1})\ \chi_{\lambda}^{\alpha}(r-r_2)\ d(\widehat{r-r_1}) \quad (3.41)$$

where $\widehat{r-r_1}$ denotes the angle between the vector r and r_1. Once the basis function $\chi_{\lambda}^{\alpha}(r)$ is expressed in terms of Gaussian-type functions, this integral can be performed analytically as shown in Appendix 1. Thus the matrix element is written as

$$\{\Delta V_{ps}(r)\}_{\lambda\alpha,\lambda'\alpha'}(k)= \sum_{m} \exp(ik\cdot R_m) \sum_{m',\beta,l} \int r^2 F_{l,\lambda}^{\alpha}(r;\ R_{m'}+d_{\beta}-d_{\alpha})$$

$$\times \Delta V_{ps}^{l}(\ r-R_{m'},-d_{\beta}\ ) F_{l,\lambda'}^{\alpha'}(r;\ R_{m'}+d_{\beta}-R_m-d_{\alpha'})dr \quad (3.42)$$

where the one-dimensional integral of r remains, but it can be easily performed numerically.

The calculation of the matrix element of $\Delta V_{coul}(r)$ is similar to that of $\Delta V_{xc}(r)$. Since $\Delta\rho(r)$ is a smooth function of r, it can be expanded in a rapidly convergent Fourier series, viz,

$$\Delta\rho(r)= \sum_{K_v} \exp(iK_v\cdot r)(\Delta\rho)_v \quad . \tag{3.43}$$

And the matrix element is calculated as

$$\{\Delta V_{coul}(r)\}_{\lambda\alpha,\lambda'\alpha'}(k)= -8\pi \sum_{m} \exp(ik\cdot R_m) \sum_{n_1,n_2} C_{n_1}^{\lambda\alpha}\, C_{n_2}^{\lambda'\alpha'} \sum_{K_v} \frac{(\Delta\rho)_v}{K_v^{\,2}}$$

$$\times \int G_{\lambda}^{\alpha}(b_{n_1}^{\lambda\alpha};r-d_{\alpha})\, \exp(iK_v\cdot r)\, G_{\lambda'}^{\alpha'}(b_{n_2}^{\lambda'\alpha'};r-R_m-d_{\alpha'})dr \tag{3.44}$$

where the integral is performed analytically as in eq.(3.40).

By using the above techniques, we succeed in calculating analytically most of the matrix elements and in abbreviating a computational time.

§ 3-5. Overall flow of calculation

The flow chart of the present calculation is shown by Fig.3-2. Following up it, we explain the overall flow of the procedure. The calculation has two stages, that is, the optimization of basis functions and the self-consistent iteration using the optimized basis functions. The first one is the characteristic of the procedure.

§ 3-5-1. Optimization of basis functions

First, the initial Mulliken's charge densities $\rho_M^{I,\alpha}(r)$ of each atom are specified. By using them, the superposed charge density $\rho^{sup}(r)$(not the crystal density) are constructed, and the superposed potential $V[\rho^{sup}]$ (not the true crystal potential) is calculated. On the other hand, the numerical valence orbitals χ_λ^α are obtained from a direct solution of the atomic one-electron equation (3.19), and they are adopted as basis functions.

Next, $V[\rho^{sup}]$ and χ_λ^α are fitted by Gaussian-type functions as described in § 3-4, and the overlap and Hamiltonian matrix elements are calculated analytically, and then the solution of the secular equation provides us the resulting Mulliken's charge densities $\rho_M^{F,\alpha}(r)$.

The successive iteration is continued, until each of the resulting Mulliken's charge densities agrees with the initial one. In other words, we pass into the next stage only after the basis functions are optimized to be consistent with the corresponding charge density.

§ 3-5-2. Self-consistent iteration using optimized basis functions

At the second stage, the self-consistent band calculation is performed, using the optimized basis functions and the resulting crystal charge density $\rho^{(1)}_{cry}(r)$ obtained in the last step of the first stage.

First, we adopt $\rho^{(1)}_{cry}(r)$ as an initial crystal charge density $\rho^{I}_{cry}(r)$ and calculate the true crystal potential $V[\rho^{I}_{cry}(r)]$, and then fit it by Gaussian-type functions. After calculating the matrix elements and solving the secular equation, the resulting crystal charge density $\rho^{F}_{cry}(r)$ is obtained.

The successive iteration is also continued, until the resulting crystal charge density agrees with the initial one, that is, the crystal charge density is consistent with the crystal potential. Finally, we obtain the self-consistent band structure and charge density.

§ 3-6. Calculation of total energy

The total ground state energy in Rydberg atomic unit is given as follows:

$$E_{tot} = T + E_{ion\text{-}ele} + E_{ele\text{-}ele} + E_{ion\text{-}ion} + \int E_{xc}[\rho_{val}(r)]dr, \quad (3.45)$$

$$T = \frac{\Omega}{(2\pi)^3} \sum_j \int_{BZ} dk \ \Psi_j^*(k,r)(-\nabla^2)\Psi_j(k,r)dr \ , \quad (3.46)$$

$$E_{ion\text{-}ele} = \sum_{\alpha,m} \int V_{ps}(r-R_m-d_\alpha) \ \rho_{val}(r)dr \ , \quad (3.47)$$

$$E_{ele\text{-}ele} = \iint \frac{\rho_{val}(r)\rho_{val}(r')}{|r - r'|} drdr' \ , \quad (3.48)$$

$$E_{ion\text{-}ion} = \sum_{\alpha,m} \sum_{\beta,l} \frac{Z_\alpha Z_\beta}{|R_m+d_\alpha-R_l-d_\beta|} \ , \quad (3.49)$$

where Z_α is the number of the valence electrons of the atom α. The exchange-correlation energy $E_{xc}[\rho(r)]$ is given in the LDF formalism by

$$E_{xc}[\rho(r)] = \rho(r)\varepsilon_{xc}[\rho(r)] \ , \quad (3.50)$$

where $\varepsilon_{xc}[\rho(r)]$ is the exchange-correlation energy per electron of a homogeneous system with a electron density $\rho(r)$, and its detailed description is given § 3-2.

By using the band energy $E_j(k)$ in eq.(3.1), the total energy can be rewritten as

$$E_{tot} = \frac{\Omega}{(2\pi)^3} \sum_j \int_{BZ} E_j(k)dk + E_{ion\text{-}ion} - E_{ele\text{-}ele}$$

$$+ \int \{ E_{xc}[\rho_{val}(r)] - \rho_{val}(r)V_{xc}[\rho_{val}(r)] \} dr. \qquad (3.51)$$

In calculating the Coulomb term in eq.(3.51), which is $E_{ion\text{-}ion} - E_{ele\text{-}ele}$, we use the method of Bachelet et al.,[33] in order to achieve the convergence of the lattice summation. They have introduced an artificial ionic charge density $\rho_I(r)$ defined as

$$\rho_I(r) = \sum_{\alpha,m} g_\alpha(|r-R_m-d_\alpha|) , \qquad (3.52)$$

where $g_\alpha(r)$ is an atomic charge density with a Gaussian distribution with a decay constant A_α (whose values are 1.1 for a M atom and 0.2 for P and S atoms, in a.u.):

$$g_\alpha(r) = -Z_\alpha(A_\alpha/\pi)^{3/2}\exp(-A_\alpha r^2) . \qquad (3.53)$$

Then, the Coulomb term can be written as

$$E_{ion\text{-}ion} - E_{ele\text{-}ele} = \frac{1}{2}\left[\int V_T(r)\{\rho_I(r)-\rho_{val}(r)\}dr + \sum_{\alpha,m}\sum_{\beta,l} J_{\alpha\beta} - \sum_{\alpha,m} C_\alpha\right], \quad (3.54)$$

where

$$V_T(r) = \int \frac{dr'}{|r-r'|}[\rho_I(r')+\rho_{val}(r')] \quad (3.55)$$

is the Hartree potential generated by an overall neutral distribution of charges and where

$$J_{\alpha\beta} = \frac{Z_\alpha Z_\beta}{|R_m+d_\alpha-R_l-d_\beta|}\,\mathrm{erfc}\left[\left(\frac{A_\alpha A_\beta}{A_\alpha+A_\beta}\right)^{1/2}|R_m+d_\alpha-R_l-d_\beta|\right], \quad (3.56)$$

$$C_\alpha = Z_\alpha^2(2A_\alpha/\pi)^{1/2} . \quad (3.57)$$

The error function erfc(x) is defined as

$$\mathrm{erfc}(x) = \frac{2}{\sqrt{\pi}}\int_x^\infty \exp(-u^2)du . \quad (3.58)$$

As a result, the double lattice summations in eq.(3.54) are easily calculated, because of the rapid damping of the value of $J_{\alpha\beta}$. Furthermore, the integral in eq.(3.55) over the whole crystal converges rapidly, since the $\rho_I(r)$ and $\rho_{val}(r)$ are completely canceled each other at a large r.

Finally, the total energy per unit cell E_{tot}^{uc} can be written as

$$E_{tot}^{uc} = \frac{\Omega_{uc}}{(2\pi)^3} \sum_j \int_{BZ} E_j(k)dk + \int_{uc} \{ E_{xc}[\rho_{val}(r)] - \rho_{val}(r)V_{xc}[\rho_{val}(r)]\}dr$$

$$+ \frac{1}{2} \left[\int_{uc} V_T(r)\{\rho_I(r)-\rho_{val}(r)\}dr + \sum_\alpha \{ \sum_{\beta,l} J_{\alpha\beta} - C_\alpha \}\right], \quad (3.59)$$

where Ω_{uc} is the volume of the unit cell and the integral over a real space is performed over the unit cell.

Chapter 4. Results of calculations

§ 4-1. Graphite and Hexagonal BN

We will apply the present method for the self-consistent calculation to the band structures of transition metal chalcogeno-phosphates MPX_3. In order to investigate the reliability and efficiency of the method, we first calculate the band structures of graphite and hexagonal BN which have been investigated in detail. In each calculation, we use the 2s, $2p_x$, $2p_y$ and $2p_z$ atomic-like orbitals of carbon, boron and nitrogen, as the basis functions.

§ 4-1-1. Graphite

The initial valence charge configuration of each carbon atom is 2s(2.0)2p(2.0), and the optimized one is 2s(1.0)2p(3.0). The optimized basis functions are determined from this configuration. The atomic radial parts in these basis functions $r\times R_\lambda^\alpha(r)$ are fitted by five Gaussian-type functions within the error of 1 %, in the region where the value of $r\times R_\lambda^\alpha(r)$ is larger than 1/10 of its maximum value. The fitting parameters of 2s and 2p atomic orbitals are listed in Table 4-1. The atomic-like potential is also fitted by five Gaussian functions with more accuracy.

As shown in eqs.(3.27) and (3.37), the calculation of matrix elements involves a lattice summation, and the convergence must be achieved. It is done in the following ways.

In calculating $S_{\lambda\alpha,\lambda'\alpha'}(k)$, $T_{\lambda\alpha,\lambda'\alpha'}(k)$, $(\Delta V_{xc})_{\lambda\alpha,\lambda'\alpha'}(k)$ and $(\Delta V_{coul})_{\lambda\alpha,\lambda'\alpha'}(k)$, a single summation is involved and performed over the range defined by

$$\left| R_m + d_{\alpha'} - d_{\alpha} \right| \leq D_A^{\alpha,\lambda} + D_A^{\alpha',\lambda'}. \qquad (4.1)$$

Here the $D_A^{\alpha,\lambda}$ is the damping radius where the value of a radial function $r \times R_\lambda^\alpha(r)$ is damped 1/20 of its maximum value. The damping radii of carbon, boron and nitrogen atoms are collected in Table 4-2. The calculations have also been performed for the damping radius for the 1/10 damping. The results are very similar to those for the 1/20 damping, except for the splitting of the lower π band. For the 1/10 damping, the magnitude of this splitting is very small. Moreover, in calculating $(V_h)_{\lambda\alpha,\lambda'\alpha'}(k)$, $(V_{xc})_{\lambda\alpha,\lambda'\alpha'}(k)$ and $(\Delta V_{ps})_{\lambda\alpha,\lambda'\alpha'}(k)$, a double summation is involved. The summation of R_m is performed over the range defined by eq.(4.1), and the summation of $R_{m'}$ (this corresponds to the center of an atomic potential) is performed over the range defined by

$$\left| R_{m'} + d_{\beta} - d_{\alpha} \right| \leq D_A^{\alpha,\lambda} + D_p^{\beta} \qquad (4.2)$$

and

$$\left| R_{m'} + d_{\beta} - R_m - d_{\alpha'} \right| \leq D_A^{\alpha',\lambda'} + D_p^{\beta} \quad . \qquad (4.3)$$

Here the D_p^{β} is the damping radius where the value of an atomic potential is damped 1/100 of its maximum value.

In calculating the Mulliken's charge density $\rho_M^{\alpha}(r)$ and the crystal charge density, we must perform the integral over the BZ. In the present method, we use a special k-points algorithm,[34,35] which chooses a discrete number of points in the BZ and an associated set of weight functions, and then sums over them. We use 3 points in the 1/12 irreducible section of the BZ (or 36 points in the full zone),since the result is nearly the same as that obtained by using 1 point.

After only two cycles of the self-consistent iteration, the self-consistent band structure is obtained, which is shown in Fig.4-1. In calculating the density of states, we divide the energy range (from -30 eV to 20 eV) into the intervals with the width of 0.25 eV, and calculate the number of states lying in each interval. In doing so, the irreducible section of the BZ is divided into 512 small cells (or 6144 cells in the full zone). Finally, the histogram for the density of states thus obtained is smoothed by the Gaussian function with the width of 0.7 eV. The result is shown in Fig.4-2.

§ 4-1-2. Hexagonal BN

The initial valence charge configurations of each atom are specified as B:2s(2.0)2p(1.0),N:2s(2.0)2p(3.0), and the optimized configurations are found to be more ionic than $B^{0.5+}N^{0.5-}$. Unfortunately the atomic-like equation(3.19) have not any bound state for the 2p orbital of $N^{0.6-}$ ion. It is often employed to introduce the Watson potential[36] in order to overcome this difficulty, but it causes the unreasonable situation that the 2s and 2p orbitals of $N^{0.6-}$ ion are more localized than those of $N^{0.5-}$ ion. Thus we adopt the $B^{0.5+}N^{0.5-}$ configuration as the optimized one and determine the optimized basis functions from it. These functions are fitted in the same way as graphite. Their fitting parameters are listed in Table 4-1. The self-consistent iteration is performed using them.

As described in § 3-4-2 , in the band structure calculation of ionic compound BN, the electronic Coulomb potential of each ion is divided into two parts, so that one part in $V_h(r)$ cancels the core Coulomb potential $V_{core}(r)$ at a moderate distance from the atomic site and each atomic part in $V_h(r)$ decreases rapidly with the distance from the atomic site. In calculating $\tilde{V}_{xc}(r)$, which includes the long-range Coulomb potential, the Ewald summation technique[32] is used in order to achieve the convergence of the lattice summation.

After four cycles of the self-consistent iteration, the self-consistent band structure is obtained, which is shown in Fig.4-3. The density of states is calculated by the same way as that of graphite and is shown in Fig.4-4.

Several calculations on the band structures of graphite and hexagonal BN have been performed by other methods.[37,38] On both graphite and BN, all of the results of these calculations and of the present one are similar to each other, except that the splitting of the lower π band (0.6 eV) is smaller than that in the previous calculations. This discrepancy is mainly caused from the underestimate of the damping radius, because the splitting is very small for the smaller damping radius, as mentioned in §4-1-1. If we fit the tail of basis function with more accuracy and choose the larger damping radius, we expect to get the larger splitting for the lower π band. It is then concluded that the present method for the self-consistent calculation of the band structure gives easily a reliable result within a reasonable computational time.

§ 4-2. Band structures of MPS_3 family

There is a van der Waals gap between the layers of MPS_3 as shown in Fig.2-1. Then, the interlayer interaction is expected to be weak, and we neglect it and calculate the two-dimensional band structure within the single-layer approximation as the first attempt to the band calculation. The effect of the interlayer interaction will be studied in the future. The two-dimensional unit cells for three types of magnetic structures (see, § 2-2) are shown in Fig.2-3. The unit cell for the nonmagnetic $ZnPS_3$ is the same as that for the type 1 magnetic structure. The thickness of the layer is set to be 6.35 Å above and below the metal plane, so that the crystal charge density decreases to less than 1/100 of its maximum value at the edge of the layer. The corresponding two-dimensional Brillouin zones(BZs) are shown in Fig.2-4.

For the basis functions in the LCAO method. we use the Zn 3d, Zn 4s, P 3s, P 3p, S 3s and S 3p atomic-like orbitals, in calculating the band structure of $ZnPS_3$. The Zn 4p orbital is not included, because the neutral Zn atom have not a 4p bound state in the LDF formalism. The influence of the Zn 4p orbital on the electronic property of $ZnPS_3$ is not so large; its detailed result is given in § 4-2-1. For other MPS_3 compounds (M= Ni, Mn and Fe), the M 4p atomic-like orbital is included in the basis functions, in order to get more accurate band structures.

The calculations of the integral over the BZ and of the long-range Coulomb potential of each ion are performed in the same way as described in § 4-1-1 and 4-1-2. In the present calculations, the damping radius of a

basis function is defined by the distance where the value is damped 1/20 of its maximum value, and that of an atomic potential is defined by the distance of 1/100 damping as in the case of graphite and hexagonal BN. In Table 4-3, the damping radii of zinc, nickel, manganese, iron, phosphorus and sulfur atoms are collected.

§ 4-2-1. Nonmagnetic material $ZnPS_3$

The initial valence charge configurations of each atom in $ZnPS_3$ are specified as the neutral ones: $Zn(12.0)P(5.0)S_1(6.0)[S_2(6.0)]_2$, where S_1 and S_2 denote the two inequivalent S atoms in the unit cell, as shown in Fig.2-3(a). The optimized configurations result in $Zn(10.8)P(4.3)S_1(6.7)[S_2(6.6)]_2$, that is, the valency of Zn ion is +1.2. The optimized basis functions are determined from these configurations, and they are fitted by five or six Gaussian-type functions in the same way as described in § 4-1-1. Their fitting parameters are listed in Table 4-1. The atomic-like potentials are also fitted by five Gaussian functions with more accuracy.

Through the use of the optimized basis functions, after only two cycles of the self-consistent iteration, the self-consistent band structure is obtained, which is shown in Fig.4-5. The overall features of the band structure are the following: the indirect band gap between the Γ and A or A' points in the BZ is 2.0 eV; the direct band gap at the Γ point is 2.1 eV; the higher valence bands are constructed mainly from the S 3p states; the lower conduction bands originate mainly from the Zn 4s, P 3s, S $3p_x$ and S $3p_y$ states; the Zn 3d band splits into two groups and each of them lies in 7.0 eV and 8.1 eV lower energy region than the top of the valence band and their band widths are about 0.5 eV; the effective masses of the highest valence band and of the lowest conduction band are $0.25m_e$ and $0.12m_e$ respectively and isotropic in a layer.

As shown in Fig.4-5, each band of $ZnPS_3$ is rather flat, because of the low-symmetry of the crystal structure of $ZnPS_3$. However, the S 3p and Zn 4s bands are fairly broad, whose band widths are about 5 eV(S 3p bands) and 3 eV(Zn 4s bands). The Zn 4p bands may be more broad. The band structures of other MPS_3 compounds also have this feature.

The features of the band structure near the band gap and the self-consistent Mulliken's charges of each ion are given in Tables 4-4 and 4-5, respectively. From Table 4-5, it is proved that the self-consistent valency of Zn ion is +1.3, and that $ZnPS_3$ is a rather ionic crystal and the Zn ion interacts somewhat with the S ions around them.

In order to ascertain that the Zn 4p state has not large influence for the electronic property of $ZnPS_3$, we add the Zn 4p orbital to the above optimized basis functions and calculate the non-self-consistent band structure. The result is the following: the Zn 4p bands lie in the higher energy region than the Zn 4s bands, the lower conduction bands have not the Zn 4p character, the band structure near and below the band gap is hardly changed.

§ 4-2-2. $NiPS_3$ for three types of magnetic structures

In order to investigate the relation between the magnetic structures and the electronic properties of $NiPS_3$, band structures are calculated for three types of magnetic structures. Their two-dimensional structures and the corresponding BZs are shown in Figs.2-3 and 2-4, respectively.

The initial valence charge configurations of each atom in $NiPS_3$ are specified as Ni:3d(up-5,down-3)4s(2)4p(0), P:3s(2.0)3p(3.0), S:3s(2.0)3p(4.0), that is, the neutral configurations. The optimized configurations obtained from the self-consistent calculation are as follows: [1] For the type 1 magnetic structure, Ni:3d(up-5,down-3)4s(1)4p(0), P:3s(1.5)3p(3.0), S:3s(2.0)3p(4.5). [2] For types 2 and 3, Ni:3d(up-5,down-3)4s(1)4p(0), P:3s(1.5)3p(3.0), S_1:3s(2.0)3p(4.3), S_2 and S_3:3s(2.0)3p(4.6). The optimized basis functions are determined from these configurations. These basis functions are fitted by five or six Gaussian-type functions, and their fitting parameters are listed in Table 4-1.

In the case of $ZnPS_3$, through the use of the optimized basis functions, the self-consistent band structure has obtained after only two cycles of the self-consistent iteration. However, in the case of $NiPS_3$, the value of an atomic charge of Ni ion oscillates during the self-consistent iteration, because the Ni 3d bands lie near the band gap. As a result, it needs seven or eight cycles of the self-consistent iteration to obtain the self-consistent band structure. The results are shown in Fig.4-6, in which three types of band structures are given for the type 1 BZ, in order to make the comparison of all results easy.

The main features of the band structures near the band gap and the self-consistent Mulliken's charges of each ion are collected in Tables 4-4 and 4-5. The results for types 2 and 3 are very similar; the result for type 1 is much different from those for types 2 and 3. In particular, the character of the lower conduction bands and the Mulliken's charge of Ni atom are strikingly different for type 1 from other types.

To ascertain which magnetic structure is stable, the total energies are calculated for the three types of magnetic structures. The calculated energies per unit of $(NiPS_3)_4$ are -517.7 Ry, -553.2 Ry and -550.7 Ry for types 1, 2 and 3, respectively. After all, the experimentally observed magnetic structure (type 2) proves to be much more stable than type 1 and a little stable than type 3. In other words, for $NiPS_3$, the linearly coupled magnetic structures (type 2 and type 3) are much more stable than the triangularly coupled one (type 1).

For the experimentally observed magnetic structure, the overall features of the band structure are the following: the indirect band gap is 0.5 eV; the higher valence bands are constructed mainly from the up-spin Ni 3d e_g states; the lower conduction bands originate mainly from the P 3s, S 3p and down-spin Ni 3d e_g states; the Ni 3d band splits into four narrow groups by both the exchange interaction and the ligand field of the surrounding S and P ions, and all of them lie near the band gap; the S 3s and P 3s states lie in about 12.0 eV and 17.0 eV lower energy region than the top of the valence band, respectively; the main component of the complicated bands between -5 eV and -10 eV are the S 3p states, and they also contribute the higher conduction bands; the Ni 4s, Ni 4p and P 3p states are contained in the higher conduction bands.

It is noted that the lowest conduction band is constructed mainly from the P 3s, S 3p and down-spin Ni 3d e_g states.

§ 4-2-3. $MnPS_3$ for two types of magnetic structures

As in the case of $NiPS_3$, band structures of $MnPS_3$ are calculated for two types of magnetic structures to investigate the relation between the magnetic structures and the electronic properties. The initial valence charge configurations of each atom in $MnPS_3$ are specified as the neutral ones. The optimized configurations are as follows: Mn:3d(up-5,down-0) 4s(1)4p(0), P:3s(1.5)3p(3.0), S:3s(2.0)3p(4.5). The fitting parameters of basis functions of each ion are listed in Table 4-1. Since the Mn 3d bands lie near the band gap in $MnPS_3$, it needs seven or eight cycles of the self-consistent iteration to obtain the self-consistent band structure. The results are given in Fig.4-7 for the type 1 BZ. The main features of the band structures near the band gap and the self-consistent Mulliken's charges of each ion are collected in Tables 4-4 and 4-5.

In order to ascertain which magnetic structure is stable, the total energies are calculated for the two types of magnetic structures. The calculated energies per unit of $(MnPS_3)_4$ are -404.3 Ry and -392.0 Ry for the type 1 and type 2 magnetic structures, respectively. After all, the experimentally observed magnetic structure (type 1) proves to be more stable than type 2. In other words, for $MnPS_3$, the triangularly coupled magnetic structure (type 1) is more stable than the linearly coupled one (type 2). This result contrasts with the result for $NiPS_3$, where the linearly coupled magnetic structure is more stable.

For the experimentally observed magnetic structure, the overall features of the band structure are the following: the direct band gap is 1.7

eV; the higher valence bands are constructed mainly from the up-spin Mn 3d e_g states; the lower conduction bands originate mainly from the up-spin Mn 4s and 4p, P 3s and S 3p states; by the exchange interaction, the Mn 3d bands split into below and above the band gap; the up-spin and down-spin Mn 3d bands construct the higher valence and the higher conduction bands, respectively; the S 3s and P 3s states lie in about 15.0 eV and 10.0 eV lower energy region than the top of the valence band, respectively; the main component of the complicated bands between -4 eV and -8 eV are the S 3p states.

§ 4-2-4. $FePS_3$

As described in § 2-3, $FePS_3$ and $NiPS_3$ show a substantially high capacity for the uptake of lithium, and can be good candidates for a Li-based battery. In order to compare the intercalation properties of $NiPS_3$ and $FePS_3$, the band structure of $FePS_3$ is calculated for the experimentally observed magnetic structure. The initial valence charge configurations of each atom in $FePS_3$ are specified as the neutral ones. The optimized configurations are as follows : Fe:3d(up-5,down-1)4s(1)4p(0), P:3s(1.5)3p(3.0), S:3s(2.0)3p(4.5). The fitting parameters of basis functions of each ion are listed in Table 4-1. Since the Fe 3d bands lie near the band gap in $FePS_3$, it needs seven or eight cycles of the self-consistent iteration to obtain the self-consistent band structure. The result is given in Fig.4-8 for the type 1 BZ.

The overall features of the band structure are the following: the band gap is 0 eV, that is, $FePS_3$ is a semimetal in this calculation; the higher valence bands are constructed mainly from the up-spin Fe 4s states and a little from the down-spin Fe 3d t_{2g} states; the lower conduction bands originate mainly from the down-spin Fe 3d t_{2g} states; the Fe 3d band splits into four narrow groups by both the exchange interaction and the ligand field of the surrounding S and P ions; the up-spin Fe 3d e_g and t_{2g} states lie 2.5 eV and 7.0 eV lower energy region than the Fermi level(E_F); the down-spin Fe e_g and t_{2g} states lie above 5.0 eV than the E_F and just above

the E_F, respectively; the S 3s and P 3s states lie in about 18.0 eV and 12.0 eV lower than the E_F, respectively; the main component of the complicated bands between -5 eV and -11 eV are the S 3p states. The result that $FePS_3$ is not a semiconductor but a semimetal comes from the local density approximation, and which is discussed in detail in § 5-2.

The main features of the band structure near the band gap(or Fermi level) and the self-consistent Mulliken's charges of each ion are collected in Tables 4-4 and 4-5. It is noted that the lowest conduction band is constructed from the down-spin Fe 3d t_{2g} states.

§ 4-3. Density of states of MPS_3 family

In calculating the density of states (DOS), we divide a energy range into the intervals with the width of 0.15 eV, and calculate the number of states lying in each interval. In doing so, the irreducible section of the BZ is divided into 192 small cells (or 768 cells in the full zone). Finally the histogram for the DOS thus obtained are smoothed by the Gaussian function with the width of 0.36 eV.

For the experimentally observed magnetic structure, the DOSs of MPS_3 family (M= Zn, Ni, Mn and Fe) are calculated, and the results are shown in Fig.4-9. The character of each peak in the DOS is given in Table 4-6.

In Fig.4-9, the peaks D_1^+ and D_2^+ originate mainly from the up-spin M 3d t_{2g} and e_g states, respectively; the down-spin M 3d t_{2g} and e_g states contribute to the peaks D_1^- and D_2^-, respectively. For $ZnPS_3$, which is a nonmagnetic material, the Zn 3d band splits into only two narrow groups by the ligand field (LF) of the surrounding S and P ions. For other MPS_3 compounds, the M 3d band splits into four narrow groups by both the exchange interaction and the LF.

The size of these splittings and the energy levels of D_1^+, D_2^+, D_1^- and D_2^- states of MPS_3 family change with the transition metal element. On the other hand, the P 3s and S 3s states appear in the lowest energy region in all MPS_3 compounds. Above this energy region, the S 3p states are located (in $ZnPS_3$, the Zn 3d states exist too).

§ 4-4. Optical properties of MPS_3 family

The imaginary part of the dielectric function $\varepsilon_2^{\mu}(\omega)$ (μ denotes the polarization of the light, and μ=x,y,z) is calculated in the same way as the DOS. The detail of the analytic calculation of $\varepsilon_2^{\mu}(\omega)$ is given in Appendix 2.

For the experimentally observed magnetic structure, the $\varepsilon_2^{x}(\omega)$, $\varepsilon_2^{y}(\omega)$ and $\varepsilon_2^{z}(\omega)$ of MPS_3 family (M= Zn, Ni, Mn and Fe) are calculated, and the results are shown in Fig.4-10. In order to compare the calculated results with the observed spectra, we average $\varepsilon_2^{x}(\omega)$ and $\varepsilon_2^{y}(\omega)$ and obtain $\varepsilon_2^{xy}(\omega)$ for the light polarized parallel to the layer, which are shown in Fig.4-11 with the experimental results by Piacentini et al.[6,7] The main features in the $\varepsilon_2^{xy}(\omega)$ spectrum are listed in Table 4-7 with the experimental results. (For $ZnPS_3$, there may exist more structures which are related to the Zn 4p bands above about 7 eV.) Moreover, in order to investigate the matrix element effect(MEE)* on the $\varepsilon_2^{xy}(\omega)$ spectrum, the joint density of states (JDOS) is calculated, which is shown in Fig.4-12. For $FePS_3$, the value of $JDOS/\omega^2$ is very large near the 0 eV, because the band gap of $FePS_3$ is 0 eV in the present calculation.

---

* The $\varepsilon_2^{\mu}(\omega)$ depends on the matrix elements of a momentum which vary according to the character of the transition. Thus, the difference between the $\varepsilon_2^{\mu}(\omega)$ and the joint density of states is attributed to the MEE.

As shown in Fig.4-11, the features of peaks in the $\varepsilon_2^{xy}(\omega)$ spectra of MPS_3 family are similar in the high energy region(beyond about 15 eV). These peaks correspond to the transitions from the S 3s and P 3s states to the conduction band states, and their intensities are stressed by the MEE. On the other hand, in the low energy region, the features of the peaks change with the transition metal element, and they are explained in detail below.

For $ZnPS_3$, as shown in Fig.4-11(a) and Table 4-7(a), the spectrum at 3.4 eV corresponds to the transitions from the S 3p states to the Zn 4s states, and its intensity is much suppressed by the MEE. The spectra at 4.9 eV, 5.3 eV, 6.6 eV and 7.2 eV correspond to the transitions from the S 3p states to the S 3p or P 3p states, and their intensities remain strong not being suppressed by the MEE. The spectra corresponding to the transitions from the Zn 3d states lie in the energy region between about 9.0 eV and 15.0 eV, and their intensities are suppressed by the MEE. Thus, the MEE is found to depend strongly on the character of the transition.

For $FePS_3$, as shown in Fig.4-11(b) and Table 4-7(b), the calculated spectra at 1.7 eV and 2.5 eV correspond to the transitions from the up-spin Fe 3d e_g and/or the up-spin Fe 4s states to the down-spin Fe 3d t_{2g} states. The transitions from the highest valence bands to the lowest conduction bands (the transitions between the down-spin Fe 3d t_{2g} states) are strongly suppressed by the MEE, so that no spectra appear near 0 eV. The peak at 5.4

eV corresponds to the transitions from the S 3p states, which locate between the up-spin Fe 3d t_{2g} and e_g states, to the down-spin Fe 3d t_{2g} states. The spectra corresponding to the transitions from the up-spin Fe 3d e_g states to the higher conduction bands lie in the energy region between about 6 eV and 10 eV; those from the lower S 3p and the up-spin Fe 3d t_{2g} states to the lower conduction bands lie in a little higher energy region. Since these transitions contain various band characters, the intensities of these peaks are not affected by the MEE so much.

For $NiPS_3$, as shown in Fig.4-11(c) and Table 4-7(c), the calculated spectra at 1.1 eV and 1.7 eV correspond to the transitions from the up-spin Ni 3d e_g states to the down-spin Ni 3d e_g states, and their intensity is much suppressed by the MEE. The spectra at 2.7 eV, 3.5 eV and 4.3 eV correspond to the transitions between the down-spin Ni 3d t_{2g} and e_g states, their intensities remain strong not being suppressed by the MEE. The spectra corresponding to the transitions from the Ni 3d states to the higher conduction bands lie in the energy region between about 3.0 eV and 13.0 eV, and those from the S 3p states lie in the energy region between about 7.0 eV and 18.0 eV.

For $MnPS_3$, as shown in Fig.4-11(d) and Table 4-7(d), the spectra at 2.1 eV and 3.3 eV correspond to the transitions from the up-spin Mn 3d e_g states to the up-spin Mn 4s and 4p states, their intensities remain strong not being suppressed by the MEE. The spectra at 4.9 eV, 5.9 eV and 6.5 eV correspond to the transitions from the S 3p states lying between the up-spin

Mn 3d t_{2g} and e_g states to the lower conduction bands, which are constructed by the up-spin Mn 4s, 4p, P 3s and S 3p states. The strongest spectra at 8.4 eV and 8.9 eV correspond to the transitions from the up-spin Mn 3d t_{2g} states to the up-spin Mn 4s and 4p states, and their intensities is not suppressed by the MEE. The spectra corresponding to the transitions from the lower S 3p states to the conduction bands lie in the energy region between about 9.0 eV and 17.0 eV.

Chapter 5. Discussion

§ 5-1. Reliability and efficiency of the computational method of band structures

In order to investigate the reliability and efficiency of the present computational method, the band structures of graphite and hexagonal BN are first calculated. By using the following three techniques: (a)the norm-conserving pseudopotential, (b)the numerical-basis-set LCAO method and (c)the Gaussian-fitting of basis functions and crystal potential, their self-consistent band structures are easily calculated within a reasonable computational time.

On both graphite and BN, the results and those by other methods[37,38] are similar to each other, except that the splitting of the lower π band (0.6 eV) is smaller than that in the previous results. As mentioned in § 4-1-2, if we fit the tail of basis function with more accuracy and choose the larger damping radius, we expect to get the larger splitting for the lower π band. It is then concluded that the present method gives a reliable result. Therefore, the present method is sufficiently practical for the calculation of the band structures of more complex crystals.

§ 5-2. Comparison with experimental results for MPS_3 family

In this subsection, we discuss our calculated results, comparing with the experimental ones which are described in § 2-4-1. The experimentally observed absorption edges[21] and magnetic moments[1] of transition metals for the MPS_3 family are collected in Table 5-1, with the calculated ones.

The valencies of each ion obtained from the self-consistent calculation are collected in Table 4-5 for the MPS_3 family, which are different from the ionic model[8] $M_2^{2+}(P_2S_6)^{4-}$. This discrepancy comes from mainly the large covalent mixing between the M ion 4s and 4p orbitals and the S ion 3p orbitals, as also suggested by Piacentini et al. It is noted that the M ion 3d orbitals are not so localized as the M^{2+} 3d orbitals and the S ion 3p orbitals are rather extended, so that both orbitals interact each other to some degree. Furthermore, for the magnetic materials such as $NiPS_3$, $MnPS_3$ and $FePS_3$, the M 3d bands lie near the band gap and have much effect on the optical spectrum in the low energy region. This means that the ionic model $M_2^{2+}(P_2S_6)^{4-}$ is inadequate and the M 3d states must be treated accurately.

As shown in Table 5-1, the calculated band gaps for the MPS_3 family are much smaller than the experimental ones. These discrepancies are caused by the local density(LD) approximation of the exchange-correlation energy term. It is generally known that the band gap of semiconductors calculated by using the LD approximation is narrower by the amount of about 2/3 than

the observed one. In particular, the LD approximation is not accurate enough to describe the localized M 3d states. The result that $FePS_3$ is not a semiconductor but a semimetal in the present calculation may be related to the LD approximation.

Furthermore, in our pseudopotential approach, M 3s and 3p states are included into core states, so that the exchange-correlation effects may be overestimated in the local-spin-density(LSD) approximation;[39] if the M 3s and 3p states are included into the valence states, the dependence of the exchange-correlation potential on the spin-directions becomes smaller. In this context, the total energy calculations of La_2CuO_4 have been performed recently,[40,41] using both a Cu(3d) pseudopotential in which 3d states are treated as the valence states as well as 4s and 4p states and a Cu(3s,3p,3d) pseudopotential, and it has been found that the magnetic state of La_2CuO_4 is affected largely by including the Cu 3s and 3p states into the valence states. In the case of $NiPS_3$, it is also likely that the magnitude of the Ni spin becomes smaller by including the Ni 3s and 3p states into the valence states. However, in the LSD approximation, our pseudopotential approach ignoring the effect of the Ni 3s and 3p states gives the result comparable with the experimental one for $NiPS_3$, as in the case of La_2CuO_4. It needs a full-electron band calculation in the LSD approximation to make clear whether the inclusion of the core effect in the LSD approximation is better or not. We suppose from our result and the results for La_2CuO_4 that it is needed not only to include the core effect but also to improve the LSD approximation.

In spite of these discrepancies in band gaps, the tendency of the calculated gap size coincides with that of the observed one; the size of band gap is getting larger with $FePS_3$, $NiPS_3$, $MnPS_3$ and $ZnPS_3$. Thus, our calculation is enough to compare the properties of the MPS_3 family,

For the magnetic moments of transition metals in the MPS_3 compounds, as shown in Table 5-1, the calculated spin-polarizations of transition metals are smaller than the observed magnetic moments. These discrepancies are caused by ignoring the spin-orbit interaction. Although the influence of this interaction on the atomic energy levels is very small(see, Fig.3-1), it is expected to enlarge the magnetic moment of a transition metal in a MPS_3 crystal. Thus, from these discrepancies, the strength of the spin-orbit interaction in a crystal can be expected that it is much larger for $NiPS_3$ than for $MnPS_3$ and $FePS_3$. On the other hand, as for the band gaps, the tendency of the size of the calculated spin-polarization coincides with that of the observed one; the size of magnetic moment is getting larger with $ZnPS_3$, $NiPS_3$, $FePS_3$ and $MnPS_3$.

As shown in Fig.4-10, for $ZnPS_3$ and $MnPS_3$ having the type 1 magnetic structure, the $\varepsilon_2^x(\omega)$ and $\varepsilon_2^y(\omega)$ are very similar; they are almost isotropic in the xy plane. On the other hand, for $NiPS_3$ and $FePS_3$ having the type 2 magnetic structure, the $\varepsilon_2^x(\omega)$ and $\varepsilon_2^y(\omega)$ are quite different. In particular, the structures in the low-energy absorption spectrum, which corresponds to

the transitions between the Ni or Fe 3d states, are much different. This anisotropy between the $\varepsilon_2^x(\omega)$ and $\varepsilon_2^y(\omega)$ reflects that of the type 2 magnetic structure. Thus, it is desired that the experimental study of the anisotropy in the xy plane should be carried out for investigating the physical properties of the MPX_3 having the type 2 magnetic structure.

As shown in Fig.4-11 and Table.4-7, the peak positions and intensity in the calculated $\varepsilon_2^{xy}(\omega)$ spectra for the light polarized parallel to the layer almost reproduce those in the observed one for $ZnPS_3$, $FePS_3$ and $NiPS_3$, in spite of the discrepancy of the direct band gap. Moreover, the calculated intensity of the spectrum has the same value as the observed one in the low energy region. For the relative intensity of peaks, the intensity of the observed peaks in the low energy region is much stronger than that in the high energy region (beyond 15 eV), and there is no explicit peak in the high energy region. On the other hand, the intensity of the calculated peaks in the low energy region is about twice or three times that in the high energy region, and several explicit peaks appear in the high energy region. Although the reason for this disagreement is not clear, we presume it is caused by the single-layer approximation. In fact, the spectrum in the high energy region corresponds to the transitions from the S 3s and P 3s states, and the S 3s states as well as the S 3p states are effected by the interlayer interaction and become more extended. Thus, the intensity of the spectrum in the high energy region is expected to become weaker by introducing the interlayer interaction.

§ 5-3. Relation between transition metal elements and magnetic properties

In order to investigate the stability of magnetic structures of $MnPS_3$ and $NiPS_3$, we calculate the band structures for some types of magnetic structures(Fig.2-3). By comparing the total energies, it is proved that the triangularly coupled magnetic structure (type 1) are more stable than the linearly coupled one (type 2) for $MnPS_3$. On the other hand, the linearly coupled magnetic structure is more stable in $NiPS_3$.

The reason for this stability of the type 1 magnetic structure in $MnPS_3$ might be as follows. As shown in Table 4-5, the Mulliken's charges of S ions are larger than that of a Mn ion in $MnPS_3$, so that the influence of S electrons on the direct electron-electron Coulomb energy ($E_{ele-ele}$) is larger than that of Mn electrons. In $MnPS_3$, the self-consistent charge density $\rho(r)$ for type 2 is more gathered around the S ions than that for type 1, so that the $E_{ele-ele}$ for type 2 is larger than that for type 1, and the type 2 magnetic structure is less stable than the type 1 one. On the other hand, in $NiPS_3$, Ni electrons have more influence on the $E_{ele-ele}$ than S electrons. Thus, the magnetic structure, which makes the charge density more localized on the Ni atoms, are less stable.

The sizes of the exchange splitting (Δ_S) and the ligand field splitting (Δ_L) of the transition metal 3d states are estimated from the average energy

of up-spin M 3d e_g states, that of up-spin M 3d t_{2g} states, that of down-spin M 3d e_g states and that of down-spin M 3d t_{2g} states. Their values for the MPS_3 family are shown in Table 5-2.

In the following, the relation between the sizes of Δ_S and Δ_L and the magnetic properties of the MPS_3 family is explained. For $MnPS_3$, the size of Δ_S is much larger than that of Δ_L, so that the up-spin Mn 3d bands completely separate from the down-spin Mn 3d bands, as shown in Fig.4-9(d). Since the band gap locates slightly above the up-spin Mn 3d e_g bands(D_2^+), the up-spin Mn 3d bands are filled with electrons, while the down-spin Mn 3d bands are empty. Thus, each Mn ion has a large spin-polarization (4.66 μ_B) in $MnPS_3$. For $FePS_3$, the size of Δ_S is a little larger than that of Δ_L, and the situation is similar to that for $MnPS_3$. However, since the separation of the up-spin and the down-spin Fe 3d bands is smaller than that for $MnPS_3$, as shown in Fig.4-9(b), the spin-polarization of each Fe ion (3.95 μ_B) is smaller than that of Mn ion. For $NiPS_3$, since the size of Δ_S is smaller than that of Δ_L, the up-spin and the down-spin Ni 3d bands are overlapped each other, as shown in Fig.4-9(c). And the band gap locates between the up-spin Ni 3d $e_g(D_2^+)$ and the down-spin Ni 3d $e_g(D_2^-)$ states, so that the spin-polarization of each Ni ion (1.03 μ_B) is much smaller than those of Mn and Fe ions. After all, in the MPS_3, whose size of Δ_S is larger than that of Δ_L, each transition metal ion has a large spin-polarization, as shown in Table 5-2.

The size of Δ_S depends mainly on the spin-polarization of the transition metal 3d electrons; the more polarized the 3d electrons are, the larger the size of Δ_S is. On the other hand, the size of Δ_L are determined from the size of the overlap of the M 3d orbitals and the surrounding S ions 3p orbitals; the more the M 3d and S 3p orbitals are overlapped, the larger the size of Δ_L is.

§ 5-4. Relation between transition metal elements and intercalation properties

The one aim of this study is to investigate the relation between transition metal elements and intercalation capacities of MPS_3 family. Moreover, we will make clear why $NiPS_3$ is more available for a cathode material in secondary lithium batteries than $FePS_3$. In the following, we discuss these subjects by using the calculated band structures of the MPS_3 family (M=Zn, Ni, Mn, Fe).

As for the intercalation capacity, it has been found[15] that intercalated lithiums are in octahedral sites of the van der Waals gap as Li^+ ions, and the electrons given up to MPS_3 are donated to conduction bands of MPS_3. Thus, the process of lithium intercalation into MPS_3 is energetically favorable only in the case where unoccupied bands of MPS_3 are at a sufficiently low energy to readily accommodate additional electrons.

From a simple energy diagram[22] (Fig.2-5), the smaller the band gap E_G value is, the larger the potential difference E_{INT} is, where E_{INT} is defined as the difference between the highest occupied level of a Li atom and the accepting level of MPS_3. In other words, the smaller the E_G value is, the larger the formation energy for the lithium intercalation is; the higher the intercalation capacity is. As shown in Table 5-1, the size of calculated band gap is getting larger with $FePS_3$, $NiPS_3$, $MnPS_3$ and $ZnPS_3$, which coincides with the observed trend. Thus, it is concluded that the

intercalation capacity of $FePS_3$ is higher than that of $NiPS_3$, and that $MnPS_3$ and $ZnPS_3$ practice very little lithium intercalation.

As for the availability of MPS_3 for a cathode material, the key requirements for a useful cathode material were proposed,[20,23] which are described in § 2-3.

As for the requirement(1), it is concluded from our results that the size of E_{INT} is larger for $FePS_3$ than for $NiPS_3$, so that the cell voltage of $FePS_3$ is higher than that of $NiPS_3$ in the early stage of intercalations.

As for the requirement(2), it is important to make clear the nature of the electron accepting levels in MPS_3 reducible by electron donors. The calculated results are as follows: The lower conduction bands of $NiPS_3$ are constructed from the P 3s, S 3p and down-spin Ni 3d e_g states, and those of $FePS_3$ are from the down-spin Fe 3d t_{2g} states. Thus, the electrons given up to $NiPS_3$ from intercalated lithiums occupy the extended conduction band states, so that they are distributed extendedly in space; on the other hand, the electrons given up to $FePS_3$ occupy the more localized states, so that they are localized near Fe ions. After all, the electronic conductivity in Li_xNiPS_3 is expected to be larger than that in Li_xFePS_3.

As for the requirement(3), the intercalated lithium ions Li^+ feel the potential of both the MPS_3 host and the given electrons to MPS_3 from the intercalated lithiums as follows:

$$V^{Li}(r) = V_{ion}(r) + V_{ele}(r) + V^{Li}_{ele}(r) \quad , \tag{5.1}$$

$$V_{ion}(r) = 2 \sum_{\alpha,m} \frac{Z_\alpha}{|r-R_m-d_\alpha|} \quad , \tag{5.2}$$

$$V_{ele}(r) = 2 \int \frac{\rho_{val}(r')}{|r - r'|} \, dr' \quad , \tag{5.3}$$

$$V^{Li}_{ele}(r) = 2 \int \frac{\rho^{Li}(r')}{|r - r'|} \, dr' \quad , \tag{5.4}$$

where Z_α and $\rho_{val}(r)$ are the valence charge of the αth atom and the valence charge density of MPS_3, respectively. The distribution of the electrons given up to MPS_3 from the intercalated lithiums, $\rho^{Li}(r)$, is calculated by using a rigid-band model, in which the electrons given up to MPS_3 are believed to occupy the conduction bands of MPS_3 without strongly modifying their structures.

For Li-$FePS_3$ and Li-$NiPS_3$ systems, the potentials $V^{Li}(r)$ are calculated in the middle layer of the van der Waals gap. The activation energy of the Li^+ diffusion is estimated from the difference between the lowest potential value in the layer and the highest one between the lowest potential points, that is, the height of the potential wall to be overcome when Li^+ ions diffuse. The results for both systems are very similar and their values are about 1 eV. Therefore, in the rigid-band model, the diffusibility of Li^+ ions in $NiPS_3$ is almost the same as that in $FePS_3$. On the other hand, it was observed that $NiPS_3$ intercalates more lithiums than $FePS_3$, then it is

inferred that the diffusibility of Li^+ ions in $NiPS_3$ is higher than that in $FePS_3$. This discrepancy is mainly caused from the rigid-band model, and it needs a band structure of Li-MPS_3 system to investigate the diffusibility of the Li^+ ions in MPS_3 quantitatively.

Therefore, we conclude from our calculated results that $NiPS_3$ is more available than $FePS_3$ in the standpoint of the requirement(2), although the cell voltage of $NiPS_3$ is a little lower than that of $FePS_3$ in the early stage of intercalations.

Chapter 6. Conclusions

In this study, we develop a new procedure of the self-consistent calculation which is adequate for the calculation of the band structure of such a complex crystal as MPS_3.[2] The main feature of the procedure is the use of the norm-conserving pseudopotential, the numerical-basis-set LCAO method and the Gaussian-fitting of basis functions and crystal potential. The reliability and efficiency of the procedure are confirmed by calculating the band structures of graphite and hexagonal BN. As a result, it becomes able to calculate the self-consistent band structure of MPS_3 without an enormous computational time.

For the sake of investigating the relation between transition metal elements and physical properties of the MPS_3 family, we have first calculated the self-consistent two-dimensional band structures of $ZnPS_3$, $NiPS_3$, $MnPS_3$ and $FePS_3$ for some types of magnetic structures.[3-5]

By comparing the total energies of some types of magnetic structures of $NiPS_3$ and $MnPS_3$, it has been proved that the triangularly coupled magnetic structure (the experimentally observed one) is more stable than the linearly coupled one for $MnPS_3$, and that the linearly coupled magnetic structure is more stable in $NiPS_3$.

The main features of the calculated band structures and self-consistent Mulliken's charges of each ion for some magnetic structures are listed in Tables 4-4 and 4-5. For the magnetic materials such as $MnPS_3$, $FePS_3$ and

$NiPS_3$, the transition metal 3d bands lie near the band gap and have much effect on their magnetic properties, intercalation properties and optical spectra in the low energy region. Thus, the previously proposed ionic model[8] $M_2^{2+}(P_2S_6)^{4-}$ is inadequate and the M 3d states must be treated accurately.

The imaginary part of the dielectric function $\varepsilon_2(\omega)$ has been also calculated, and it has been clarified that $ZnPS_3$ and $MnPS_3$ are almost isotropic in the layer, while $NiPS_3$ and $FePS_3$ are anisotropic. This anisotropy reflects that of the type 2 magnetic structure.

The calculated $\varepsilon_2(\omega)$ spectrum for the light polarized parallel to the layer reproduces the main features of the observed optical spectrum[6,7] in the low energy region. However, in the high energy region, the calculated spectrum does not agree with the observed one. This disagreement is supposed to come from the single-layer approximation.

By comparing the calculated band gaps of the MPS_3 family, it has been clarified that the capacity for lithium intercalation of $FePS_3$ is higher than that of $NiPS_3$, and that $MnPS_3$ and $ZnPS_3$ practice very little lithium intercalation.

Lastly, there is a technologically important problem why $NiPS_3$ is more available for a cathode material in secondary lithium batteries than $FePS_3$. In order to answer this problem, it is indispensable to make clear the nature of the electron accepting levels in MPS_3 reducible by electron

donors. Then, the calculated results are as follows: The lower conduction bands (the electron accepting levels) of $NiPS_3$ are constructed from the P 3s, S 3p and down-spin Ni 3d e_g states, and those of $FePS_3$ are from the down-spin Fe 3d t_{2g} states. As a result, the electrons given up to $NiPS_3$ from intercalated lithiums are distributed more extendedly in space than those to $FePS_3$, so that the electronic conductivity in Li_xNiPS_3 is larger than that in Li_xFePS_3.

As for the diffusibility of the intercalated Li^+ ions in MPS_3, the potential which the Li^+ ions feel in the middle layer of the van der Waals gap are considered for Li-$FePS_3$ and Li-$NiPS_3$ systems, in the rigid-band model. The activation energy of the Li^+ diffusion is estimated as about 1 eV and the diffusibility of the Li^+ ions in $NiPS_3$ is nearly the same as that in $FePS_3$. However, in order to investigate the diffusibility of the Li^+ ions quantitatively, the rigid-band model is not good and the band calculation of the Li-MPS_3 system is indispensable. It is concluded from our calculated results that $NiPS_3$ is more available for a cathode material in secondary lithium batteries than $FePS_3$, in the viewpoint of the electronic conductivity.

Acknowledgement

I would like to thank Prof. Kenji Nakao for a continuous guidance and critical readings of this manuscript. The calculations in the present thesis have been done by using the FACOM M-780/20 computer systems at the University of Tsukuba.

Appendix 1. Analytic calculations of matrix elements

One of the key points of the present method is the analytic calculation of matrix elements. The expressions for some integrals have been given in refs.42 and 43. These integrals appear in the matrix elements of the overlap, the kinetic energy and the term containing $\cos(K\cdot r)$. In this Appendix, we present the expressions for the following five types of integrals used in the present calculation:

(i) overlap

$$\langle i,j\rangle = \int G_i(C_1;r-r_1)\, G_j(C_2;r-r_2)\, dr \ , \tag{A.1}$$

(ii) kinetic energy

$$\langle i,T,j\rangle = \int G_i(C_1;r-r_1)\left(-\frac{1}{2}\nabla^2\right)G_j(C_2;r-r_2)\, dr \ , \tag{A.2}$$

(iii) Fourier expansion term in the potential energy

$$\langle i,E,j\rangle = \int G_i(C_1;r-r_1)\, \exp(ik\cdot r)\, G_j(C_2;r-r_2)\, dr \ , \tag{A.3}$$

(iv) Gaussian term in the potential energy

$$\langle i,G,j\rangle = \int G_i(C_1;r-r_1)\, \exp[-C_3|r-r_3|^2]\, G_j(C_2;r-r_1)\, dr \ , \tag{A.4}$$

(v) angular integral for the l-dependent pseudopotential

$$(i,j)=\int K_i(\hat{r'})\ G_j(\alpha;r'-r)\ d(\hat{r'})\ , \qquad (A.5)$$

where $G_i(C;r-r_0)$ is the Gaussian-type function situated at the site r_0 and its decay constant is C, whose concrete form is given in Table 3-3. In eq.(A.5), $K_i(\hat{r'})$ is a cubic harmonic.

Here, only independent expressions for each integral are given; others can be obtained by appropriate permutations. It is noted that the expressions given here must be multiplied by the appropriate constants resulting from the normalization of the cubic harmonics.

A-1-1. Matrix elements of overlap and kinetic energy

First, we give the results for the integral (A.1), which is used in calculating the overlap matrix elements. In this subsection, the following abbreviations are used:

$$X= x_1-x_2 \ , \ Y= y_1-y_2 \ , \ Z= z_1-z_2 \ , \ R^2= X^2+ Y^2+ Z^2 \ ,$$

$$P= C_1C_2/(C_1+C_2), \ V= 1/(C_1+C_2), \ W= [\pi/(C_1+C_2)]^{3/2}\exp(-PR^2).$$

The results of analytic calculations are

$$\langle s,s\rangle = W,$$

$$\langle s,p_x\rangle = WXVC_1,$$

$$\langle s,d_{xy}\rangle = WXYV^2C_1^2,$$

$$\langle s,d_{x^2-y^2}\rangle = W(X^2-Y^2)V^2C_1^2 \ ,$$

$$\langle s,d_{3z^2-r^2}\rangle = W(3Z^2-R^2)V^2C_1^2 \ ,$$

$$\langle p_x,p_x\rangle = WV(0.5-PX^2) \ ,$$

$$\langle p_x,p_y\rangle = -WXYPV \ ,$$

$$\langle p_x,d_{xy}\rangle = 0.5WY(1-2PX^2)V^2C_1,$$

$$\langle p_x,d_{yz}\rangle = -WXYZPV^2C_1,$$

$$\langle p_x,d_{x^2-y^2}\rangle = WX\{1-P(X^2-Y^2)\}V^2C_1,$$

$$\langle p_x, d_{3z^2-r^2} \rangle = WX\{P(X^2+Y^2-2Z^2)-1\}V^2C_1,$$

$$\langle p_z, d_{x^2-y^2} \rangle = -WZ(X^2-Y^2)PV^2C_1,$$

$$\langle p_z, d_{3z^2-r^2} \rangle = WZ\{2+P(X^2+Y^2-2Z^2)\}V^2C_1,$$

$$\langle d_{xy}, d_{xy} \rangle = 0.25W(1-2PX^2)(1-2PY^2)V^2,$$

$$\langle d_{xy}, d_{yz} \rangle = -0.5W(1-2PY^2)XZPV^2,$$

$$\langle d_{xy}, d_{x^2-y^2} \rangle = WXY(X^2-Y^2)P^2V^2,$$

$$\langle d_{xy}, d_{3z^2-r^2} \rangle = WXY\{2+P(3Z^2-R^2)\}PV^2,$$

$$\langle d_{yz}, d_{x^2-y^2} \rangle = WYZ\{1+P(X^2-Y^2)\}PV^2,$$

$$\langle d_{yz}, d_{3z^2-r^2} \rangle = -WYZ\{1+P(X^2+Y^2-2Z^2)\}PV^2,$$

$$\langle d_{x^2-y^2}, d_{x^2-y^2} \rangle = W\{1-2P(X^2+Y^2)+P^2(X^2-Y^2)^2\}V^2,$$

$$\langle d_{x^2-y^2}, d_{3z^2-r^2} \rangle = W(X^2-Y^2)\{2+P(2Z^2-X^2-Y^2)\}PV^2,$$

$$\langle d_{3z^2-r^2}, d_{3z^2-r^2} \rangle = W\{3-2P(X^2+Y^2+4Z^2)+P^2(X^2+Y^2-2Z^2)^2\}V^2.$$

Next, the matrix elements of kinetic energy are calculated by using the analytic expressions of the integral (A.2), which are given as

$$\langle s, T, s \rangle = WP(3-2PR^2),$$

$$\langle s,T,p_x\rangle = WXPVC_1(5-2PR^2),$$

$$\langle s,T,d_{xy}\rangle = WXYPV^2C_1^2(7-2PR^2),$$

$$\langle s,T,d_{x^2-y^2}\rangle = W(X^2-Y^2)PV^2C_1^2(7-2PR^2),$$

$$\langle s,T,d_{3z^2-r^2}\rangle = W(2Z^2-X^2-Y^2)(7-2PR^2)PV^2C_1^2,$$

$$\langle p_x,T,p_x\rangle = W(2.5-7PX^2-PR^2+2P^2X^2R^2)PV,$$

$$\langle p_x,T,p_y\rangle = -WXY(7-2PR^2)P^2V,$$

$$\langle p_x,T,d_{xy}\rangle = -WY(3.5-9PX^2-PR^2+2P^2X^2R^2)PV^2C_1,$$

$$\langle p_x,T,d_{yz}\rangle = WXYZ(9-2PR^2)P^2V^2C_1,$$

$$\langle p_x,T,d_{x^2-y^2}\rangle = -WX\{7-2PR^2+P(X^2-Y^2)(2PR^2-9)\}PV^2C_1,$$

$$\langle p_x,T,d_{3z^2-r^2}\rangle = -WX\{2PR^2-7+P(2PR^2-9)(3Z^2-R^2)\}PV^2C_1,$$

$$\langle p_z,T,d_{x^2-y^2}\rangle = WZ(X^2-Y^2)(9-2PR^2)P^2V^2C_1,$$

$$\langle p_z,T,d_{3z^2-r^2}\rangle = -WZ\{2(7-2PR^2)+P(2PR^2-9)(2Z^2-X^2-Y^2)\}PV^2C_1,$$

$$\langle d_{xy},T,d_{xy}\rangle = 0.5W\{(3.5-9PY^2)(1-2PX^2)+P(2PY^2-1)(2X^2+R^2-2PX^2R^2)\}PV^2,$$

$$\langle d_{xy},T,d_{yz}\rangle = WXZ\{-4.5+P(11Y^2+R^2-2PY^2R^2)\}P^2V^2,$$

$$\langle d_{xy},T,d_{x^2-y^2}\rangle = WXY(X^2-Y^2)(11-2PR^2)P^3V^2,$$

$$\langle d_{xy},T,d_{3z^2-r^2}\rangle = WXY\{18-4PR^2+P(2Z^2-X^2-Y^2)(11-2PR^2)\}P^2V^2,$$

$$\langle d_{yz}, T, d_{x^2-y^2} \rangle = WYZ\{9+11P(X^2-Y^2)-2PR^2-2P^2R^2(X^2-Y^2)\}P^2V^2,$$

$$\langle d_{yz}, T, d_{3z^2-r^2} \rangle = WYZ\{-9+2PR^2+P(11-2PR^2)(2Z^2-X^2-Y^2)\}P^2V^2,$$

$$\langle d_{x^2-y^2}, T, d_{x^2-y^2} \rangle = W\{7-2PR^2+2P(X^2+Y^2)(2PR^2-9)+P^2(X^2-Y^2)^2(11-2PR^2)\}PV^2,$$

$$\langle d_{x^2-y^2}, T, d_{3z^2-r^2} \rangle = W(X^2-Y^2)\{18-4PR^2+P(11-2PR^2)(2Z^2-X^2-Y^2)\}P^2V^2,$$

$$\langle d_{3z^2-r^2}, T, d_{3z^2-r^2} \rangle = WPV^2\{21-6PR^2+2P(2PR^2-9)(X^2+Y^2+4Z^2) + P^2(11-2PR^2)(2Z^2-X^2-Y^2)^2\}.$$

A-1-2. Matrix elements containing exp(ik·r)

In calculating the matrix elements of potential energy, it is needed to perform the integral (A.3). By using the following abbreviations:

$$A=\frac{1}{C_1+C_2}\ ,\ X=x_1-x_2\ ,\ Y=y_1-y_2\ ,\ Z=z_1-z_2\ ,$$

$$B=(\pi A)^{3/2}\exp[-AC_1C_2|r_1-r_2|^2]\ \exp[iAk\cdot(C_1r_1+C_2r_2)]\ ,$$

the analytic expressions of the integral (A.3) are given as

$$\langle s,E,s\rangle = B,$$

$$\langle s,E,p_X\rangle = BA(C_1X+i0.5k_X)\ ,$$

$$\langle s,E,d_{XY}\rangle = BA^2\{(C_1^2XY-0.25k_Xk_y)+i0.5C_1(k_XY+k_yX)\},$$

$$\langle s,E,d_{x^2-y^2}\rangle = BA^2[\{C_1^2(X^2-Y^2)-0.25(k_X^2-k_y^2)\}+iC_1(k_XX-k_yY)],$$

$$\langle s,E,d_{3z^2-r^2}\rangle = BA^2[\{C_1^2(2Z^2-X^2-Y^2)-0.25(2k_Z^2-k_X^2-k_y^2)\}+iC_1(2k_ZZ-k_XX-k_yY)],$$

$$\langle p_X,E,p_X\rangle = BA^2\{(-C_1C_2X^2-0.25k_X^2+0.5/A)+i0.5k_X(C_1-C_2)X\},$$

$$\langle p_X,E,p_y\rangle = BA^2\{(-C_1C_2XY-0.25k_Xk_y)+i0.5(C_1k_XY-C_2k_yX)\},$$

$$\langle p_X,E,d_{XY}\rangle = BA^3[\{-C_1^2C_2X^2Y+0.25C_1Y(2/A-k_X^2)-0.25(C_1-C_2)k_Xk_yX\}$$
$$+i\{0.5C_1(C_1-C_2)k_XXY-0.5C_1C_2k_yX^2+(-k_X^2k_y+2k_y/A)/8\}],$$

$$\langle p_X,E,d_{yZ}\rangle = BA^3[\{C_2X(-C_1^2YZ+0.25k_yk_Z)-0.25C_1k_X(k_yZ+k_ZY)\}$$
$$+i\{0.5k_X(C_1^2YZ-0.25k_yk_Z)-0.5C_1C_2X(k_yZ+k_ZY)\}],$$

$$<p_x,E,d_{x^2-y^2}>= BA^3[-C_1^2C_2X(X^2-Y^2)-0.5C_1k_x(k_xX-k_yY)+X\{C_1/A+0.25C_2(k_x^2-k_y^2)\}$$

$$+i\{0.5C_1^2k_x(X^2-Y^2)-C_1C_2X(k_xX-k_yY)+k_x(4/A-k_x^2+k_y^2)/8\}],$$

$$<p_x,E,d_{3z^2-r^2}>= BA^3[-C_1^2C_2X(2Z^2-X^2-Y^2)-0.5C_1k_x(2k_zZ-k_xX-k_yY)$$

$$+X\{-C_1/A+0.25C_2(2k_z^2-k_x^2-k_y^2)\}$$

$$+i\{0.5C_1^2k_x(2Z^2-X^2-Y^2)-C_1C_2X(2k_zZ-k_xX-k_yY)$$

$$-k_x(2k_z^2-k_x^2-k_y^2+4/A)/8\}],$$

$$<p_z,E,d_{x^2-y^2}>= BA^3[C_2Z\{-C_1^2(X^2-Y^2)+0.25(k_x^2-k_y^2)\}-0.5C_1k_z(k_xX-k_yY)$$

$$+i\{0.5C_1^2k_z(X^2-Y^2)-C_1C_2Z(k_xX-k_yY)-k_z(k_x^2-k_y^2)/8\}],$$

$$<p_z,E,d_{3z^2-r^2}>= BA^3[\{-C_1^2C_2Z(2Z^2-X^2-Y^2)-0.5C_1k_z(2k_zZ-k_xX-k_yY)+2C_1Z/A$$

$$+0.25C_2Z(2k_z^2-k_x^2-k_y^2)\}$$

$$+i\{0.5C_1^2k_z(2Z^2-X^2-Y^2)-C_1C_2Z(2k_zZ-k_xX-k_yY)+k_z/A$$

$$-k_z(2k_z^2-k_x^2-k_y^2)/8\}],$$

$$<d_{xy},E,d_{xy}>= BA^4[C_1^2C_2^2X^2Y^2+0.25C_1C_2\{(k_y^2-2/A)X^2+(k_x^2-2/A)Y^2\}$$

$$-0.25(C_1-C_2)^2k_xk_yXY-(k_x^2+k_y^2)/(8A)+k_x^2k_y^2/16+0.25/A^2$$

$$+i0.5(C_1-C_2)\{(-C_1C_2XY-0.25k_xk_y)(k_xY+k_yX)+0.5(k_xX+k_yY)/A\}],$$

$$<d_{xy},E,d_{yz}>= BA^4[(C_2^2XY-0.25k_xk_y)(C_1^2YZ-0.25k_yk_z)+0.25C_1C_2(k_xY+k_yX)(k_yZ+k_zY)$$
$$-(4C_1C_2XZ+k_xk_z)/(8A)$$
$$+i0.125\{-C_2(k_xY+k_yX)(4C_1^2YZ-k_yk_z)+C_1(4C_2^2XY-k_xk_y)(k_yZ+k_zY)$$
$$+2(C_1k_xZ-C_2k_zX)/A\}],$$

$$<d_{xy},E,d_{x^2-y^2}>= BA^4[\{C_1^2C_2^2XY+0.25k_xk_y(2C_2-C_1)\}(X^2-Y^2)$$
$$+\{4C_2(2C_1-C_2)XY+k_xk_y\}(k_x^2-k_y^2)/16$$
$$+i[C_2(k_xY+k_yX)\{(k_x^2-k_y^2)-4C_1^2(X^2-Y^2)\}/8$$
$$-(k_xY-k_yX)/(2A^2)+C_1(C_2^2XY-k_xk_y/4)(k_xX-k_yY)]],$$

$$<d_{xy},E,d_{3z^2-r^2}>= BA^4[(4C_2^2XY-k_xk_y)\{4C_1^2(2Z^2-X^2-Y^2)-(2k_z^2-k_x^2-k_y^2)\}/16$$
$$+0.5C_1C_2(k_xY+k_yX)(2k_zZ-k_xX-k_yY)+2C_1C_2XY/A+k_xk_y/(2A)$$
$$+i[(k_xY+k_yX)\{-0.5C_1^2C_2(2Z^2-X^2-Y^2)+C_2(2k_z^2-k_x^2-k_y^2)/8$$
$$-(C_1-C_2)/(2A)\}+C_1(C_2^2XY-k_xk_y/4)(2k_zZ-k_xX-k_yY)]],$$

$$<d_{yz},E,d_{x^2-y^2}>= BA^4[C_1^2(X^2-Y^2)(C_2^2YZ-k_yk_z/4)+(k_x^2-k_y^2)(k_yk_z-4C_2^2YZ)/16$$
$$+C_1C_2(k_yZ+k_zY)(k_xX-k_yY)/2+C_1C_2YZ/A+k_yk_z/(4A)$$
$$+i[C_2(k_yZ+k_zY)\{-4C_1^2(X^2-Y^2)+(k_x^2-k_y^2)\}/8$$
$$+C_1(4C_2^2YZ-k_yk_z)(k_xX-k_yY)/4-(C_1k_zY-C_2k_yZ)/(2A)]],$$

$$<d_{yz},E,d_{3z^2-r^2}>= BA^4[C_1^2(2Z^2-X^2-Y^2)(C_2^2YZ-k_yk_z/4)+(2k_z^2-k_x^2-k_y^2)(k_yk_z-4C_2^2YZ)/16$$

$$+C_1C_2(k_yZ+k_zY)(2k_zZ-k_xX-k_yY)/2-C_1C_2YZ/A-k_yk_z/(4A)$$

$$+i[C_2(k_yZ+k_zY)\{-4C_1^2(2Z^2-X^2-Y^2)+2k_z^2-k_x^2-k_y^2\}/8$$

$$+C_1(4C_2^2YZ-k_yk_z)(2k_zZ-k_xX-k_yY)/4$$

$$+\{(2C_1+C_2)k_yZ-(C_1+2C_2)k_zY\}/(2A)]],$$

$$<d_{x^2-y^2},E,d_{x^2-y^2}>= BA^4[C_1^2C_2^2(X^2-Y^2)^2-(C_1^2+C_2^2)(k_x^2-k_y^2)(X^2-Y^2)/4+C_1C_2(k_xX-k_yY)^2$$

$$-2C_1C_2(X^2+Y^2)/A+(k_x^2-k_y^2)^2/16-(k_x^2+k_y^2)/(2A)+1/A^2$$

$$+i[-(C_1-C_2)(k_xX-k_yY)\{C_1C_2(X^2-Y^2)+(k_x^2-k_y^2)/4\}$$

$$+(C_1-C_2)(k_xX-k_yY)/A]],$$

$$<d_{x^2-y^2},E,d_{3z^2-r^2}>= BA^4[\{(k_x^2-k_y^2)-4C_2^2(X^2-Y^2)\}(2k_z^2-k_x^2-k_y^2)/16$$

$$+C_1^2\{4C_2^2(X^2-Y^2)-(k_x^2-k_y^2)\}(2Z^2-X^2-Y^2)/4+2C_1C_2(X^2-Y^2)/A$$

$$+C_1C_2(k_xX-k_yY)(2k_zZ-k_xX-k_yY)+(k_x^2-k_y^2)/(2A)$$

$$+i[(k_xX-k_yY)\{C_2(2k_z^2-k_x^2-k_y^2)/4-C_1^2C_2(2Z^2-X^2-Y^2)$$

$$-(C_1-C_2)/A\}$$

$$+C_1\{C_2^2(X^2-Y^2)-(k_x^2-k_y^2)/4\}(2k_zZ-k_xX-k_yY)]],$$

$$<d_{3z^2-r^2},E,d_{3z^2-r^2}>=BA^4[C_1^2C_2^2(2Z^2-X^2-Y^2)^2-2C_1C_2(4Z^2+X^2+Y^2)/A+3/A^2$$

$$-(C_1^2+C_2^2)(2Z^2-X^2-Y^2)(2k_z^2-k_x^2-k_y^2)/4$$

$$+C_1C_2(2k_zZ-k_xX-k_yY)^2+(2k_z^2-k_x^2-k_y^2)^2/16$$

$$-(4k_z^2+k_x^2+k_y^2)/(2A)$$

$$+i(C_2-C_1)[(2k_zZ-k_xX-k_yY)\{C_1C_2(2Z^2-X^2-Y^2)$$

$$+(2k_z^2-k_x^2-k_y^2)/4\}-(4k_zZ+k_xX+k_yY)/A]].$$

A-1-3. Matrix elements containing $\exp(-\alpha r^2)$

In calculating the matrix elements of potential energy, it is also needed to perform the integral (A.4), whose analytic expressions are given in this subsection. The following abbreviations are used:

$$C=C_1+C_2+C_3 ,$$

$$\lambda= \frac{1}{4\pi}\left[\frac{\pi}{C}\right]^{3/2}\exp\left[- \frac{C_1C_2|r_1-r_2|^2}{C_1+C_2}\right] \exp\left[- \frac{C_3|(C_1+C_2)r_3-C_1r_1-C_2r_2|^2}{C(C_1+C_2)}\right] ,$$

$$X_a=-(C_2+C_3)x_1+C_2x_2+C_3x_3 , \quad X_b=C_1x_1-(C_1+C_3)x_2+C_3x_3 ,$$

$$Y_a=-(C_2+C_3)y_1+C_2y_2+C_3y_3 , \quad Y_b=C_1y_1-(C_1+C_3)y_2+C_3y_3 ,$$

$$Z_a=-(C_2+C_3)z_1+C_2z_2+C_3z_3 , \quad Z_b=C_1z_1-(C_1+C_3)z_2+C_3z_3 .$$

The results of analytic calculations are

$$\langle s,G,s\rangle = \lambda ,$$

$$\langle s,G,p_x\rangle = \lambda X_b/C ,$$

$$\langle s,G,d_{xy}\rangle = \lambda X_bY_b/C^2 ,$$

$$\langle s,G,d_{x^2-y^2}\rangle = \lambda(X_b^2-Y_b^2)/C^2 ,$$

$$\langle s,G,d_{3z^2-r^2}\rangle = \lambda(2Z_b^2-X_b^2-Y_b^2)/C^2 ,$$

$$\langle p_x,G,p_x\rangle = \lambda(X_aX_b+0.5C)/C^2 ,$$

$$\langle p_x, G, p_y \rangle = \lambda X_a Y_b / C^2 \ ,$$

$$\langle p_x, G, d_{xy} \rangle = \lambda Y_b (X_a X_b + 0.5C) / C^3 \ ,$$

$$\langle p_x, G, d_{yz} \rangle = \lambda X_a Y_b Z_b / C^3 \ ,$$

$$\langle p_x, G, d_{x^2-y^2} \rangle = \lambda [X_a (X_b^2 - Y_b^2) + C X_b] / C^3 \ ,$$

$$\langle p_x, G, d_{3z^2-r^2} \rangle = \lambda [X_a (2Z_b^2 - X_b^2 - Y_b^2) - C X_b] / C^3 \ ,$$

$$\langle p_z, G, d_{x^2-y^2} \rangle = \lambda Z_a (X_b^2 - Y_b^2) / C^3 \ ,$$

$$\langle p_z, G, d_{3z^2-r^2} \rangle = \lambda [Z_a (2Z_b^2 - X_b^2 - Y_b^2) + 2C Z_b] / C^3 \ ,$$

$$\langle d_{xy}, G, d_{xy} \rangle = \lambda (X_a X_b + 0.5C)(Y_a Y_b + 0.5C) / C^4 \ ,$$

$$\langle d_{xy}, G, d_{yz} \rangle = \lambda X_a Z_b (Y_a Y_b + 0.5C) / C^4 \ ,$$

$$\langle d_{xy}, G, d_{x^2-y^2} \rangle = \lambda [X_a Y_a (X_b^2 - Y_b^2) - C(X_a Y_b - X_b Y_a)] / C^4 \ ,$$

$$\langle d_{xy}, G, d_{3z^2-r^2} \rangle = \lambda [X_a Y_a (2Z_b^2 - X_b^2 - Y_b^2) - C(X_a Y_b + X_b Y_a)] / C^4 \ ,$$

$$\langle d_{yz}, G, d_{x^2-y^2} \rangle = \lambda Z_a [Y_a (X_b^2 - Y_b^2) - C Y_b] / C^4 \ ,$$

$$\langle d_{yz}, G, d_{3z^2-r^2} \rangle = \lambda [Y_a Z_a (2Z_b^2 - X_b^2 - Y_b^2) - C(Y_b Z_a - 2 Y_a Z_b)] / C^4 \ ,$$

$$\langle d_{x^2-y^2}, G, d_{x^2-y^2} \rangle = \lambda [(X_a^2 - Y_a^2)(X_b^2 - Y_b^2) + 2C(X_a X_b + Y_a Y_b) + C^2] / C^4 \ ,$$

$$\langle d_{x^2-y^2}, G, d_{3z^2-r^2} \rangle = \lambda [(X_a^2 - Y_a^2)(2Z_b^2 - X_b^2 - Y_b^2) - 2C(X_a X_b - Y_a Y_b)] / C^4 \ ,$$

$$\langle d_{3z^2-r^2}, G, d_{3z^2-r^2} \rangle = \lambda [(2Z_a^2 - X_a^2 - Y_a^2)(2Z_b^2 - X_b^2 - Y_b^2) + 2C(4 Z_a Z_b + X_a X_b + Y_a Y_b) + 3C^2] / C^4 .$$

A-1-4. Matrix elements of l-dependent pseudopotential energy

In calculating the matrix elements of the l-dependent part of pseudopotential energy, it is needed to perform the integral (A.5). The following abbreviations are used:

$$R = r', \quad Q = \sqrt{X^2+Y^2+Z^2},$$

$$E = 4\pi\{\exp[-\alpha(R-Q)^2]+\exp[-\alpha(R+Q)^2]\},$$

$$F = 4\pi\{\exp[-\alpha(R-Q)^2]-\exp[-\alpha(R+Q)^2]\},$$

$$D(X^l Y^m Z^n) = \frac{\partial^{l+m+n}}{\partial X^l \partial Y^m \partial Z^n}(s,s),$$

where X, Y and Z are the x, y and z components of r.
And the results for the integral (A.5) are given as follows:

$$(s,s) = F/(4\alpha QR),$$

$$(s,p_x) = X[2\alpha Q(ER-FQ)-F]/(8\alpha^2 Q^3 R),$$

$$(s,d_{xy}) = XY\{4\alpha^2Q^2[F(Q^2+R^2)-2EQR]-2\alpha Q(3ER-2FQ)+3F\}/(16\alpha^3Q^5R),$$

$$(s,d_{x^2-y^2}) = (s,d_{xy})(X^2-Y^2)/(XY),$$

$$(s,d_{3z^2-r^2}) = (s,d_{xy})(2Z^2-X^2-Y^2)/(XY),$$

$$(p_x,p_x) = [4\alpha^2X^2Q^2R(FR-EQ)-2\alpha X^2Q(3ER-FQ)+2\alpha Q^3RE+(3X^2-Q^2)F]/(16\alpha^3Q^5R^2),$$

$$(p_x,p_y) = XY[4\alpha^2Q^2R(FR-EQ)-2\alpha Q(3ER-FQ)+3F]/(16\alpha^3Q^5R^2),$$

$$(p_X, d_{xy}) = Y\{8\alpha^3X^2Q^3R[E(Q^2+R^2)-2FQR]+4\alpha^2Q^2[Q^2R(FR-EQ)-X^2(6FR^2-6EQR+FQ^2)]$$

$$+2\alpha Q[3X^2(5ER-2FQ)-Q^2(3ER-FQ)]+3(Q^2-5X^2)F\}/(32\alpha^4Q^7R^2) ,$$

$$(p_X, d_{yz}) = XYZ\{8\alpha^3Q^3R[E(Q^2+R^2)-2FQR]-4\alpha^2Q^2(6FR^2-6EQR+FQ^2)$$

$$+6\alpha Q(5ER-2FQ)-15F\}/(32\alpha^4Q^7R^2) ,$$

$$(p_X, d_{x^2-y^2}) = X\{(X^2-Y^2)[8\alpha^3Q^3R(EQ^2+ER^2-2FQR)-4\alpha^2Q^2(6FR^2-6EQR+FQ^2)$$

$$+6\alpha Q(5ER-2FQ)-15F]+8\alpha^2Q^4R(FR-EQ)-4\alpha Q^3(3ER-FQ)+6FQ^2\}/(32\alpha^4Q^7R^2),$$

$$(p_X, d_{3z^2-r^2}) = X\{(2Z^2-X^2-Y^2)[8\alpha^3Q^3R(EQ^2+ER^2-2FQR)-4\alpha^2Q^2(6FR^2-6EQR+FQ^2)$$

$$+6\alpha Q(5ER-2FQ)-15F]-8\alpha^2Q^4R(FR-EQ)+4\alpha Q^3(3ER-FQ)-6FQ^2\}/(32\alpha^4Q^7R^2),$$

$$(p_Z, d_{x^2-y^2}) = Z(X^2-Y^2)[8\alpha^3Q^3R(EQ^2+ER^2-2FQR)-4\alpha^2Q^2(6FR^2-6EQR+FQ^2)$$

$$+6\alpha Q(5ER-2FQ)-15F]/(32\alpha^4Q^7R^2) ,$$

$$(p_Z, d_{3z^2-r^2}) = Z\{(2Z^2-X^2-Y^2)[8\alpha^3Q^3R(EQ^2+ER^2-2FQR)-4\alpha^2Q^2(6FR^2-6EQR+FQ^2)$$

$$+6\alpha Q(5ER-2FQ)-15F]+16\alpha^2Q^4R(FR-EQ)-8\alpha Q^3(3ER-FQ)+12FQ^2\}/(32\alpha^4Q^7R^2),$$

$$(d_{xy}, d_{xy}) = \{D(X^2Y^2)+2\alpha[XD(XY^2)+YD(X^2Y)+D(X^2)+D(Y^2)]$$

$$+4\alpha^2[XYD(XY)+XD(X)+YD(Y)+(s,s)]\}/(16\alpha^5R^3) ,$$

$$(d_{xy}, d_{yz}) = \{D(XY^2Z)+2\alpha[XD(Y^2Z)+YD(XYZ)+D(XZ)]+4\alpha^2X[D(Z)+YD(YZ)]\}/(16\alpha^5R^3),$$

$$(d_{xy}, d_{x^2-y^2}) = \{D(X^3Y)-D(XY^3)+2\alpha[YD(X^3)-XD(Y^3)+XD(X^2Y)-YD(XY^2)]$$

$$+4\alpha^2[2YD(X)-2XD(Y)+XYD(X^2)-XYD(Y^2)]\}/(16\alpha^5R^3) ,$$

$$(d_{xy}, d_{3z^2-r^2}) = (2D(XYZ^2)-D(X^3Y)-D(XY^3)+2\alpha\{Y[2D(XZ^2)-D(X^3)-D(XY^2)]$$

$$+X[2D(YZ^2)-D(X^2Y)-D(Y^3)]-4D(XY)\}+4\alpha^2XY[2D(Z^2)-D(X^2)$$

$$-D(Y^2)]-8\alpha^2[XD(Y)+YD(X)])/(16\alpha^5R^3) ,$$

$$(d_{yz}, d_{x^2-y^2}) = (D(X^2YZ)-D(Y^3Z)+2\alpha\{Y[D(X^2Z)-D(Y^2Z)+Z[D(X^2Y)-D(Y^3)]$$

$$-2D(YZ)\}+4\alpha^2Z\{Y[D(X^2)-D(Y^2)]-2D(Y)\})/(16\alpha^5R^3) ,$$

$$(d_{yz}, d_{3z^2-r^2}) = (2D(YZ^3)-D(X^2YZ)-D(Y^3Z)+2\alpha\{Y[2D(Z^3)-D(X^2Z)-D(Y^2Z)]$$

$$+Z[2D(YZ^2)-D(X^2Y)-D(Y^3)]+2D(YZ)\}+4\alpha^2\{YZ[2D(Z^2)-D(X^2)$$

$$-D(Y^2)]+4YD(Z)-2ZD(Y)\})/(16\alpha^5R^3) ,$$

$$(d_{x^2-y^2}, d_{x^2-y^2}) = (D(X^4)-2D(X^2Y^2)+D(Y^4)+4\alpha\{2[D(X^2)+D(Y^2)]$$

$$+X[D(X^3)-D(XY^2)]+Y[D(Y^3)-D(X^2Y)]\}$$

$$+4\alpha^2\{4[(s,s)+XD(X)+YD(Y)]+(X^2-Y^2)[D(X^2)-D(Y^2)]\})$$

$$/(16\alpha^5R^3) ,$$

$$(d_{x^2-y^2}, d_{3z^2-r^2}) = (2[D(X^2Z^2)-D(Y^2Z^2)]-D(X^4)+D(Y^4)+4\alpha\{X[2D(XZ^2)$$

$$-D(XY^2)-D(X^3)]-Y[2D(YZ^2)-D(X^2Y)-D(Y^3)]-2[D(X^2)-D(Y^2)]\}$$

$$+4\alpha^2\{(X^2-Y^2)[2D(Z^2)-D(X^2)-D(Y^2)]-4[XD(X)-YD(Y)]\})$$

$$/(16\alpha^5R^3) ,$$

$$(d_{3z^2-r^2}, d_{3z^2-r^2}) = (4[D(Z^4)-D(X^2Z^2)-D(Y^2Z^2)]+D(X^4)+D(Y^4)+2D(X^2Y^2)$$

$$+4\alpha\{2Z[2D(Z^3)-D(X^2Z)-D(Y^2Z)]-X[2D(XZ^2)-D(X^3)-D(XY^2)]$$

$$-Y[2D(YZ^2)-D(X^2Y)-D(Y^3)]+2[4D(Z^2)+D(X^2)+D(Y^2)]\}$$

$$+4\alpha^2\{(2Z^2-X^2-Y^2)[2D(Z^2)-D(X^2)-D(Y^2)]+4[4ZD(Z)+XD(X)$$

$$+YD(Y)+3(s,s)]\})/(16\alpha^5R^3) .$$

Appendix 2. Analytic calculation of $\varepsilon_2^{\mu}(\omega)$.

The imaginary part of the dielectric function $\varepsilon_2^{\mu}(\omega)$ (μ=x,y,z) is given by

$$\varepsilon_2^{\mu}(\omega)=\frac{1}{\pi}\left[\frac{e}{m\omega}\right]^2 \sum_{i'}^{con} \sum_{i}^{val} \int_{BZ} \left| P^{\mu}_{i,i'}(k) \right|^2 \delta(E_{i'}(k)-E_i(k)-\hbar\omega)dk, \qquad (A.6)$$

where the summation i' and i are carried out over the empty conduction band states and the occupied valence band states, respectively. In the LCAO method, the matrix elements of the momentum $P^{\mu}_{i',i}(k)$ can be written , by using eqs.(3.17) and (3.18), as

$$P^{\mu}_{i',i}(k)=-i\hbar \sum_{\alpha,\alpha'} \sum_{\lambda,\lambda'} C^{*}_{i',\lambda'\alpha'}(k)\, C_{i,\lambda\alpha}(k) \sum_{m} \exp(ik\cdot R_m)$$

$$\times \int \chi^{\alpha'}_{\lambda'}(r-R_m-d_{\alpha'}) \frac{\partial}{\partial r_{\mu}} \chi^{\alpha}_{\lambda}(r-d_{\alpha})\, dr. \qquad (A.7)$$

In the present procedure, the basis function $\chi^{\alpha}_{\lambda}(r)$ is expressed in terms of Gaussian-type functions, so that the three-dimensional integral in eq.(A.7) can be performed analytically, that is, the matrix element $P^{\mu}_{i,i'}(k)$ is calculated analytically.

This analytical calculation is one of the advantages of the present procedure. In this appendix, we present the expressions for the integral:

$$\langle i,x,j\rangle = \int G_i(C_1;r-r_1)\ \frac{\partial}{\partial x}\ G_j(C_2;r-r_2)\ dr\ ,$$

where $G_i(C_1;r)$ is the Gaussian-type functions, whose concrete form is given in Table 3-3. The other integrals, <i,y,j> and <i,z,j>, are calculated in the same way as <i,x,j>.

The following abbreviations are used below:

$$A=C_1C_2/(C_1+C_2)\ ,\quad B=1/(C_1+C_2)\ ,$$

$$X=x_1-x_2\ ,\quad Y=y_1-y_2\ ,\quad Z=z_1-z_2\ ,\quad R=X^2+Y^2+Z^2\ ,$$

$$\lambda=\left[\frac{\pi}{C_1+C_2}\right]^{3/2}\exp[-AR]\ .$$

Only independent expressions are given; others can be obtained by appropriate permutations. It is noted that the expressions given here must be multiplied by the appropriate constants resulting from the normalization of the cubic harmonics.

$$\langle s,x,s\rangle=-2\lambda AX\ ,$$

$$\langle s,x,p_x\rangle=\lambda C_1B(1-2AX^2)\ ,$$

$$\langle s,x,p_y\rangle=-2\lambda C_1ABXY\ ,$$

$$\langle s,x,d_{xy}\rangle=\lambda C_1^2B^2Y(1-2AX^2)\ ,$$

$$\langle s,x,d_{yz}\rangle=-2\lambda C_1^2AB^2XYZ\ ,$$

$$\langle s,x,d_{x^2-y^2}\rangle=2\lambda C_1^2B^2X\{1-A(X^2-Y^2)\}\ ,$$

$$\langle s,x,d_{3z^2-r^2}\rangle=-2\lambda C_1^2 B^2 X\{1+A(2Z^2-X^2-Y^2)\} ,$$

$$\langle p_x,x,p_x\rangle=-\lambda ABX(3-2AX^2) ,$$

$$\langle p_x,x,p_y\rangle=-\lambda ABY(1-2AX^2) ,$$

$$\langle p_x,x,d_{xy}\rangle=-\lambda C_1 AB^2 XY(3-2AX^2) ,$$

$$\langle p_x,x,d_{yz}\rangle=-\lambda C_1 AB^2 YZ(1-2AX^2) ,$$

$$\langle p_x,x,d_{x^2-y^2}\rangle=\lambda C_1 B^2 [(1-2AX^2)\{1-A(X^2-Y^2)\}-2AX^2] ,$$

$$\langle p_x,x,d_{3z^2-r^2}\rangle=-\lambda C_1 B^2 [(1-2AX^2)\{1+A(2Z^2-X^2-Y^2)\}-2AX^2] ,$$

$$\langle p_y,x,p_y\rangle=-\lambda ABX(1-2AY^2) ,$$

$$\langle p_y,x,p_z\rangle=2\lambda A^2 BXYZ ,$$

$$\langle p_y,x,d_{xy}\rangle=0.5\lambda C_1 B^2 (1-2AX^2)(1-2AY^2) ,$$

$$\langle p_y,x,d_{yz}\rangle=-\lambda C_1 AB^2 XZ(1-2AY^2) ,$$

$$\langle p_y,x,d_{zx}\rangle=-\lambda C_1 AB^2 YZ(1-2AX^2) ,$$

$$\langle p_y,x,d_{x^2-y^2}\rangle=2\lambda C_1 A^2 B^2 XY(X^2-Y^2) ,$$

$$\langle p_y,x,d_{3z^2-r^2}\rangle=2\lambda C_1 AB^2 XY\{2+A(2Z^2-X^2-Y^2)\} ,$$

$$\langle p_z,x,d_{x^2-y^2}\rangle=-2\lambda C_1 AB^2 XZ\{1-A(X^2-Y^2)\} ,$$

$$\langle p_z,x,d_{3z^2-r^2}\rangle=-2\lambda C_1 AB^2 XZ\{1-A(2Z^2-X^2-Y^2)\} ,$$

$$\langle d_{xy},x,d_{xy}\rangle=-0.5\lambda AB^2 X(3-2AX^2)(1-2AY^2) ,$$

$$\langle d_{xy},x,d_{yz}\rangle=-0.5\lambda AB^2 Z(1-2AX^2)(1-2AY^2) ,$$

$$\langle d_{xy}, x, d_{zx} \rangle = \lambda A^2 B^2 XYZ(3-2AX^2) ,$$

$$\langle d_{xy}, x, d_{x^2-y^2} \rangle = \lambda A^2 B^2 Y\{(1-2AX^2)(X^2-Y^2)+2X^2\} ,$$

$$\langle d_{xy}, x, d_{3z^2-r^2} \rangle = \lambda AB^2 Y[(1-2AX^2)\{2+A(2Z^2-X^2-Y^2)\}-2AX^2] ,$$

$$\langle d_{yz}, x, d_{yz} \rangle = -0.5\lambda AB^2 X(1-2AY^2)(1-2AZ^2) ,$$

$$\langle d_{yz}, x, d_{zx} \rangle = -0.5\lambda AB^2 Y(1-2AZ^2)(1-2AX^2) ,$$

$$\langle d_{yz}, x, d_{x^2-y^2} \rangle = -2\lambda A^3 B^2 XYZ(X^2-Y^2) ,$$

$$\langle d_{yz}, x, d_{3z^2-r^2} \rangle = -2\lambda A^3 B^2 XYZ(2Z^2-X^2-Y^2) ,$$

$$\langle d_{zx}, x, d_{x^2-y^2} \rangle = -\lambda AB^2 Z[(1-2AX^2)\{1-A(X^2-Y^2)\}-2AX^2] ,$$

$$\langle d_{zx}, x, d_{3z^2-r^2} \rangle = -\lambda AB^2 Z[(1-2AX^2)\{1-A(2Z^2-X^2-Y^2)\}+2AX^2] ,$$

$$\langle d_{x^2-y^2}, x, d_{x^2-y^2} \rangle = -2\lambda AB^2 X\{3-4AX^2+A^2(X^2-Y^2)^2\} ,$$

$$\langle d_{x^2-y^2}, x, d_{3z^2-r^2} \rangle = 2\lambda AB^2 X\{2+2A(Z^2-2X^2+Y^2)-A^2(2Z^2-X^2-Y^2)(X^2-Y^2)\} ,$$

$$\langle d_{3z^2-r^2}, x, d_{3z^2-r^2} \rangle = 2\lambda AB^2 X\{-5+4A(X^2+Y^2+Z^2)-A^2(2Z^2-X^2-Y^2)^2\} .$$

References

1) R.Brec: Intercalation in Layered Materials, ed. M.S.Dresselhaus(Plenum Press, New York, 1986) p.93.

2) N.Kurita and K.Nakao : J. Phys. Soc. Jpn. **56** (1987) 4442.

3) N.Kurita and K.Nakao : J. Phys. Soc. Jpn. **56** (1987) 4456.

4) N.Kurita and K.Nakao : to be published in J. Phys. Soc. Jpn. **58** (1989) No.1.

5) N.Kurita and K.Nakao : to be published in J. Phys. Soc. Jpn. **58** (1989) No.2.

6) M.Piacentini, F.S.Khumalo, C.G.Olson, J.W.Anderegg and D.W.lynch : Chemical Physics **65** (1982) 289.

7) M.Piacentini, F.S.Khumalo, G.Leveque, C.G.Olson and D.W.Lynch : Chemical Physics **72** (1982) 61.

8) F.S.Khumalo and H.P.Hughes : Phys. Rev. **B23** (1981) 5375.

9) M.Piacentini, V.Grasso, S.Santangelo, M.Fanfoni, S.Modesti and A.Savoia : Solid State Commun. **51**(1984) 467.

10) M.H.Whangbo, R.Brec, G.Ouvrard and J.Rouxel : Inorg. Chem. **24** (1985) 2459.

11) H.Mercier, Y.Mathey and E.Canadell : Inorg. Chem. **26** (1987) 963.

12) G.Ouvrard, R.Brec and J.Rouxel : Mater. Res. Bull. **20** (1985) 1181.

13) W.Klingen, G.Eulenberger and H.Hahn : Naturwissenschaften **57** (1970) 88.

14) E.Prouzet, G.Ouvrard and R.Brec : Mater. Res. Bull. **21** (1986) 195.

15) C.Berthier, Y.Chabre and M.Minier : Solid State Commun. **28** (1978) 327.

16) K.Kurosawa, S.Saito and Y.Yamaguchi: J. Phys. Soc. Jpn. **52** (1983) 3919.

17) G.Le Flem, R.Brec, G.Ouvrard, A.Louisy and P.Segransan : J. Phys. Chem. Solids **43** (1982) 455.

18) A.Wiedenmann, J.Rossat Mignod, A.Louisy, R.Brec and J.Rouxel: Solid State Commun. **40** (1981) 1067.

19) R.Clement, J.J.Girerd and I.Morgenstern-Badarau : Inorg. Chem. **19** (1980) 2852.

20) A.H.Thompson and M.S.Whittingham : Mater. Res. Bull. **12** (1977) 741.

21) R.Brec, D.M.Schleich, G.Ouvrard, A.Louisy and J.Rouxel : Inorg. Chem. **18** (1979) 1814.

22) R.Brec, G.Ouvrard, A.Louisy, J.Rouxel and A.LeMehaute : Solid State Ionics **6** (1982) 185.

23) D.W.Murphy and P.A.Christian : Science **205** (1979) 651.

24) P.J.S.Foot, J.Suradi and P.A.Lee : Mater. Res. Bull. **15** (1980) 189.

25) A.Zunger and A.J.Freeman : Phys. Rev. B**15** (1977) 4716.

26) S.Itoh and K.Nakao : J. Phys. Soc. Jpn. **54** (1985) 4648.

27) G.B.Bachelet , D.R.Hamann and M.Schluter : Phys. Rev. B**26** (1983) 4199.

28) D.M.Ceperley and B.J.Alder : Phys. Rev. Lett. **45** (1980) 566.

29) J.Perdew and A.Zunger : Phys. Rev. B**23** (1981) 5048.

30) F.Herman and S.Skillman : Atomic Structure Calculations (Prentice-Hall, Englewood Cliffs, N.J.,1963)

31) T.Nakagawa and Y.Oyanagi : Program System SALS for Nonlinear Least-Squares Fitting in Experimental Sciences (North Holland Publishing Company ,1980) P. 221.

32) P.P.Ewald : Ann. Phys.(Germany) **64** (1921) 753.

33) G.B.Bachelet, H.S.Greenside, G.A.Baraff and M.Schluter : Phys. Rev. **B24** (1981) 4745.

34) D.J.Chadi and M.L.Cohen : Phys. Rev. B**8** (1973) 5747.

35) H.J.Monkhorst and J.D.Pack : Phys. Rev. B**13** (1976) 5188.

36) R.E.Watson : Phys. Rev. **111** (1958) 1108.

37) R.C.Tatar and S.Rabii : Phys. Rev. B25 (1982) 4126.

38) E.Doni and G.Pastori Parravicini : Nuovo Cimento **63B** (1969) 117.

39) S.G.Louie, S.Froyen and M.L.Cohen : Phys. Rev. **B26** (1982) 1738.

40) K.Shiraishi, A.Oshiyama, N.Shima, T.Nakayama and H.Kamimura : Solid State Commun. **66** (1988) 629.

41) H.Kamimura, T.Nakayama, A.Oshiyama, N.Shima and K.Shiraishi : Proc. 19th Int. Conf. Physics of Semiconductors, Warsaw, 1988.

42) R.C.Chaney , T.K.Tung , C.C.Lin and E.E.Lafon : J. Chem. Phys. **52** (1970) 361.

43) J.Langlinais and J.Callaway : Phys. Rev. B5 (1972) 124.

Fig.2-1. Crystal structure of MPX_3. Signs o, • and 8 denote a X atom(X is either sulfur or selenium), a M atom and a pair of phosphorus atoms, respectively.

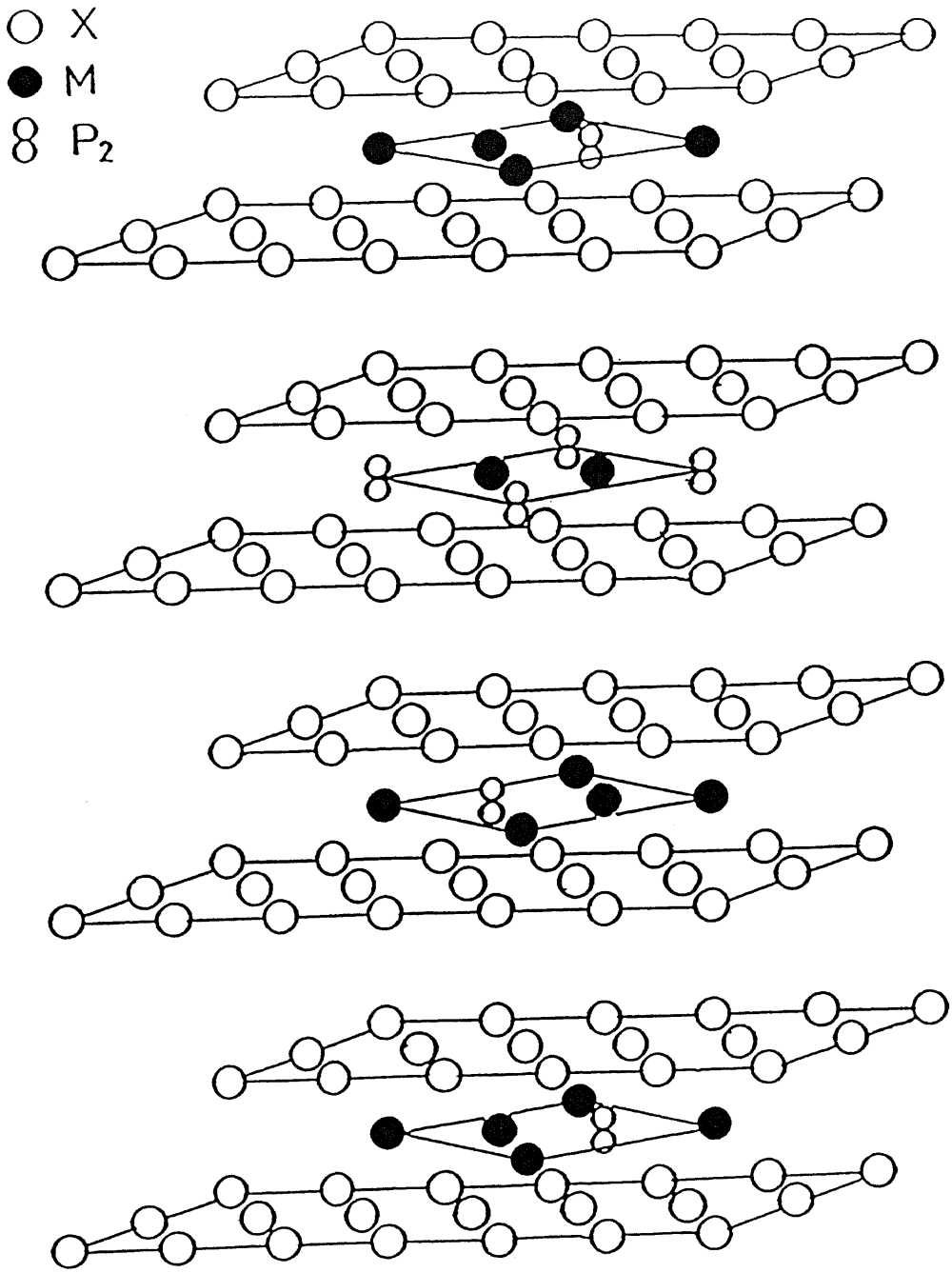

Fig.2-2. Three-dimensional magnetic structures of MPS_3 family: (a)$NiPS_3$ and $CoPS_3$, (b)$MnPS_3$ and (c)$FePS_3$. Black and white circles are up- and down-spins of transition metal atoms.

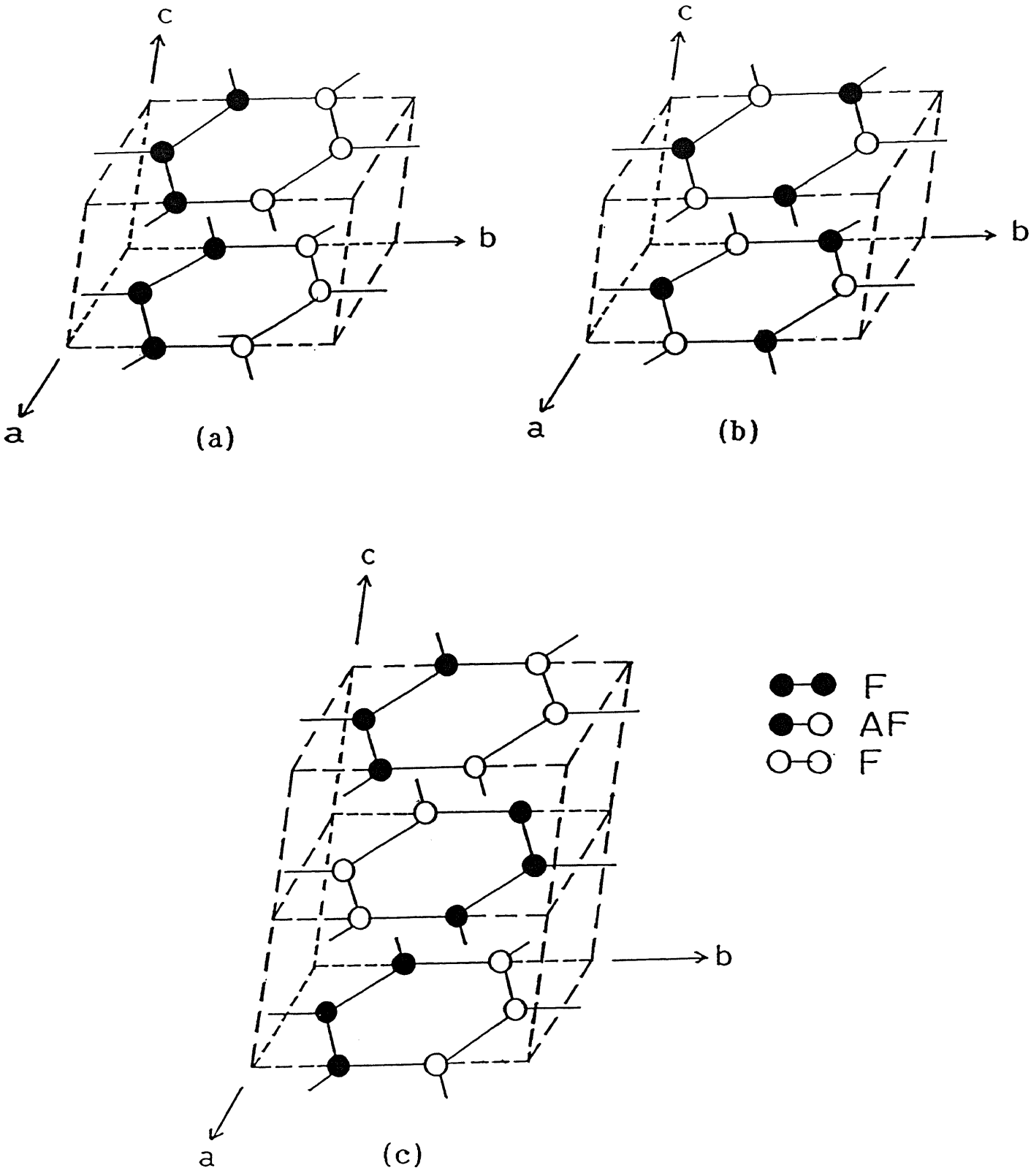

Fig.2-3. Two-dimensional magnetic structures of MPS_3 assumed in our calculation: (a)type 1, (b)type 2, (c)type 3. Positions of the atoms in MPS_3 are projected on the basal plane. The S atoms are located in each corner of slightly distorted hexagons, and the inequivalent S atoms in the unit-cell are indicated by S_1,S_2, S_3, S_4 and S_5. The M atoms are located in the z=0 plane; the P atoms occupy the z=±1.07 Å planes; the S atoms occupy the z=±1.54 Å planes. The two-dimensional unit cells are indicated by dashed squares. The monoclinic **a** and **b** axes are also shown.

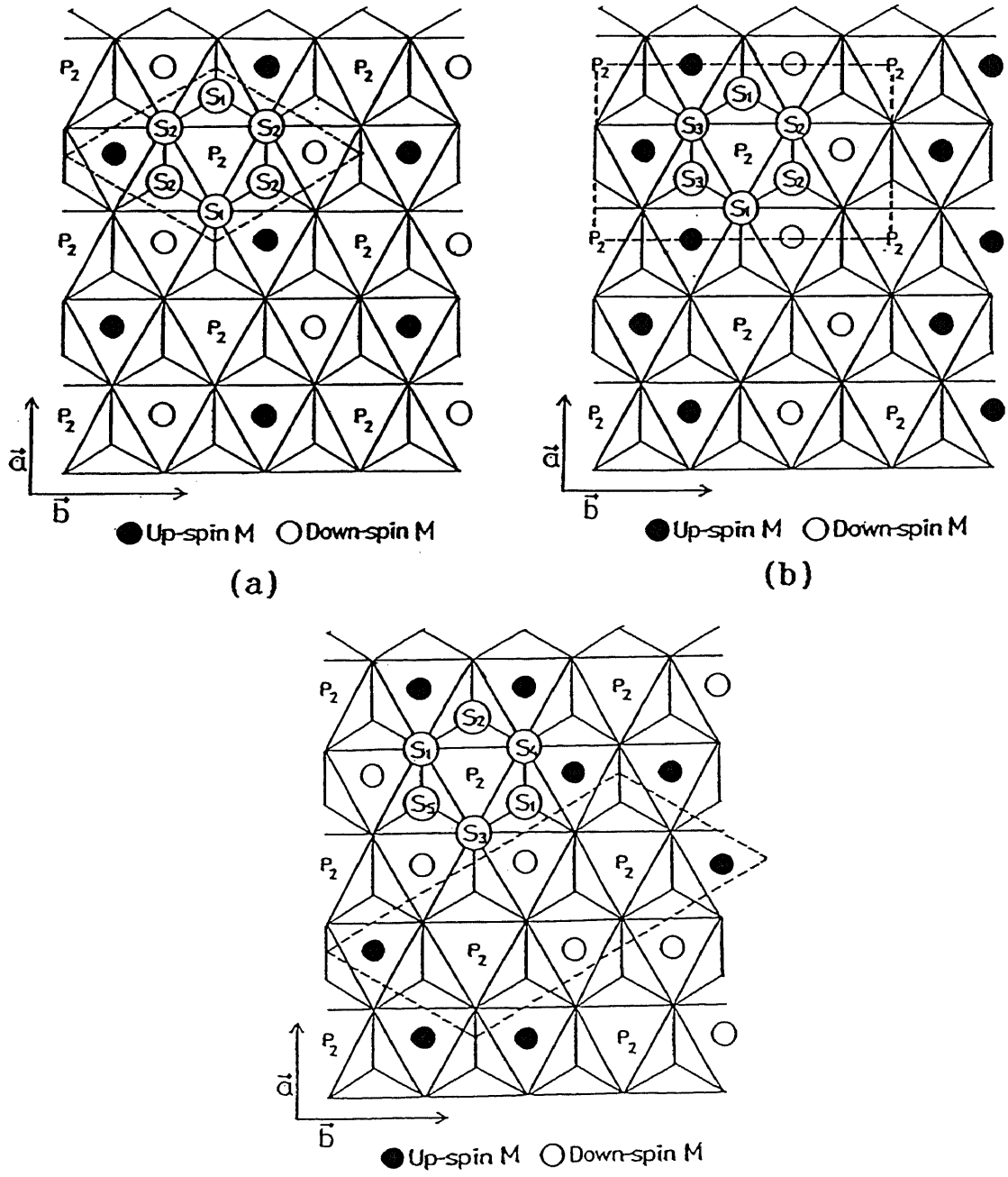

Fig.2-4. Three types of the two-dimensional Brillouin zone of MPS_3. The solid, broken and dotted lines are for the type 1, type 2 and type 3 magnetic structures, respectively.

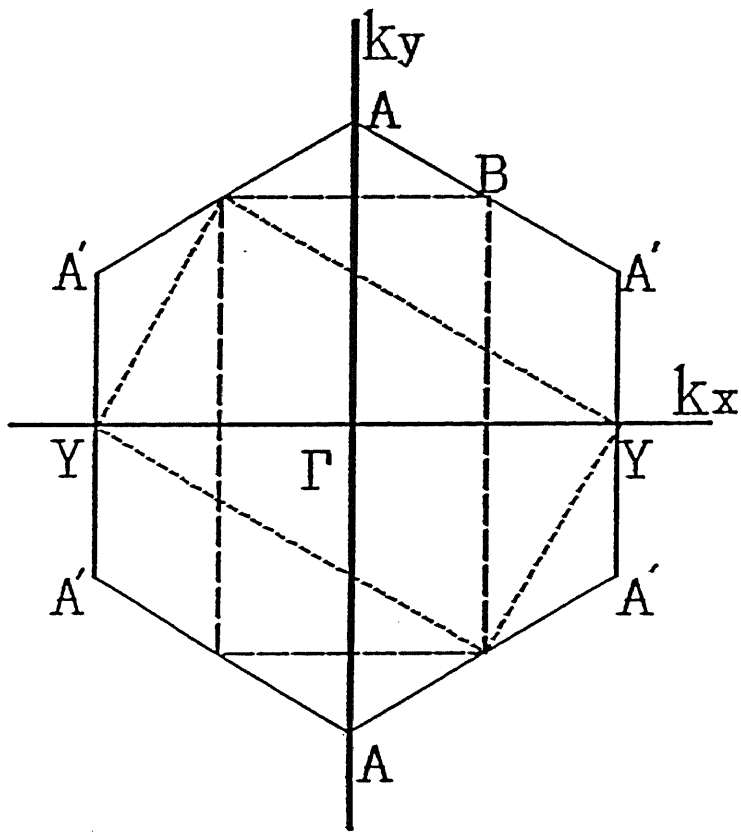

Fig.2-5. A simple energy diagram of Li_xMPS_3 systems (after ref.22). E_{INT} is the potential difference between the highest occupied level of a Li atom and the accepting level of MPS_3. The band gap of MPS_3 is indicated by E_G.

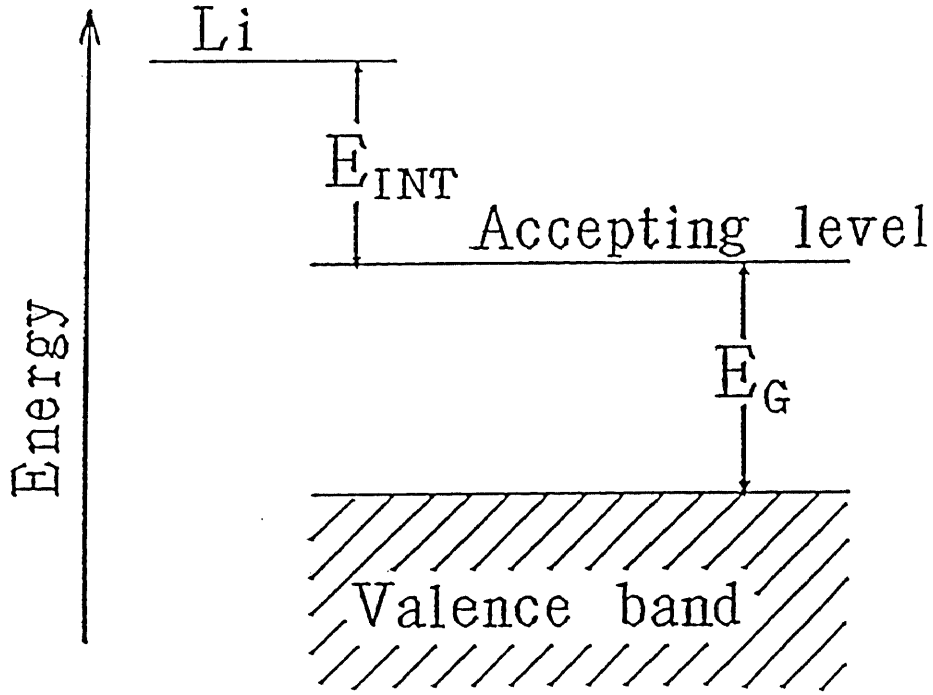

Fig.2-6. Density of states of MPS_3 family calculated by using the extended Hückel method (only low lying orbitals are represented): (a)$MnPS_3$, (b)$FePS_3$ and (c)$NiPS_3$. The character of each peak is described in § 2-4-2.

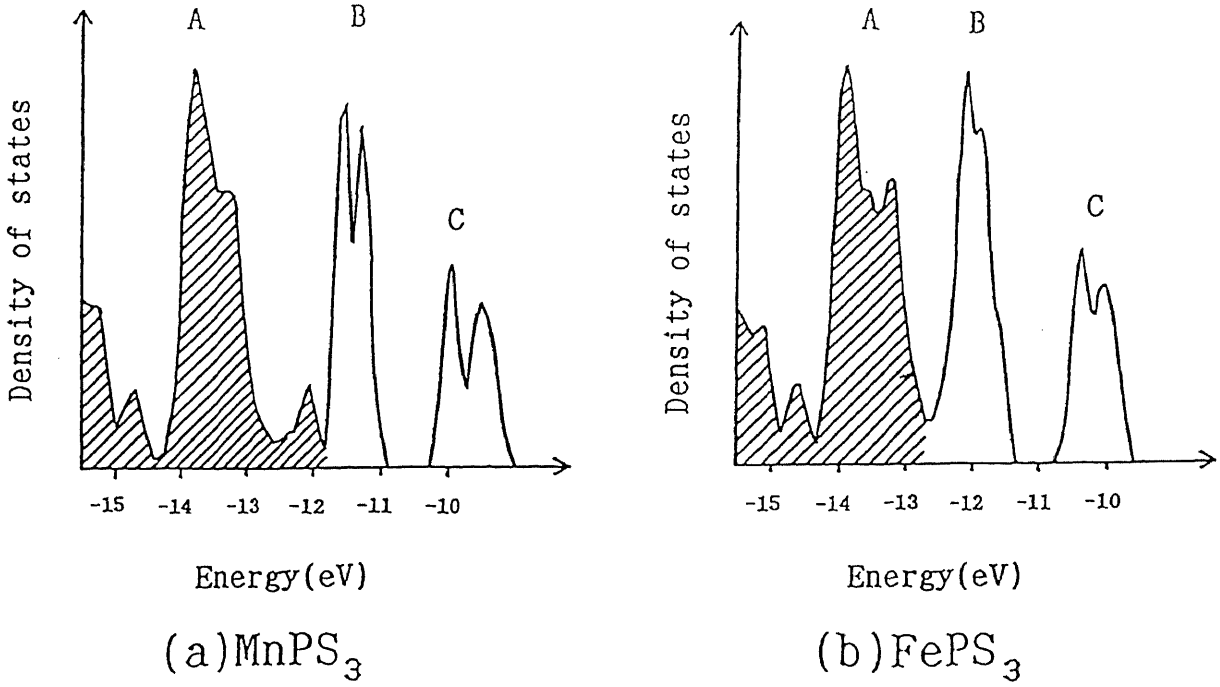

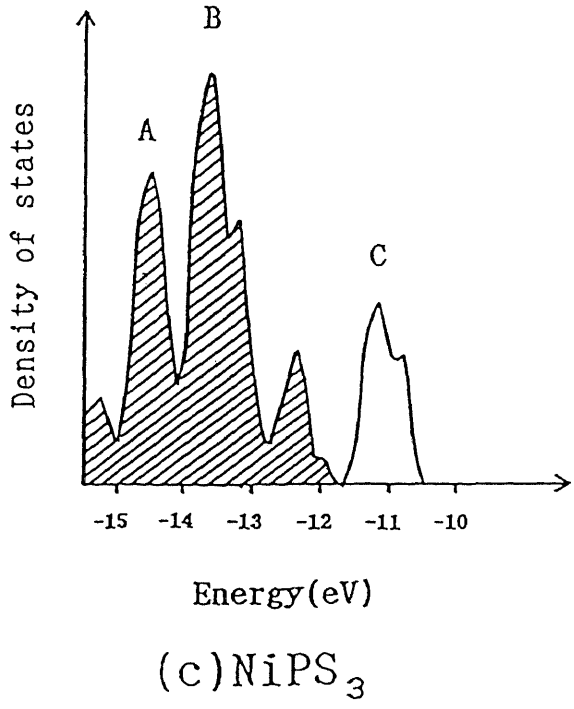

Fig.3-1. Pseudopotential for Ni atom: (a)the l-dependent short-range Coulomb part $\Delta V_{ps}^{l}(r)$ in eq.(3.4), (b)the spin-orbit interaction part $V_{l}^{so}(r)$ in eq.(3.3).

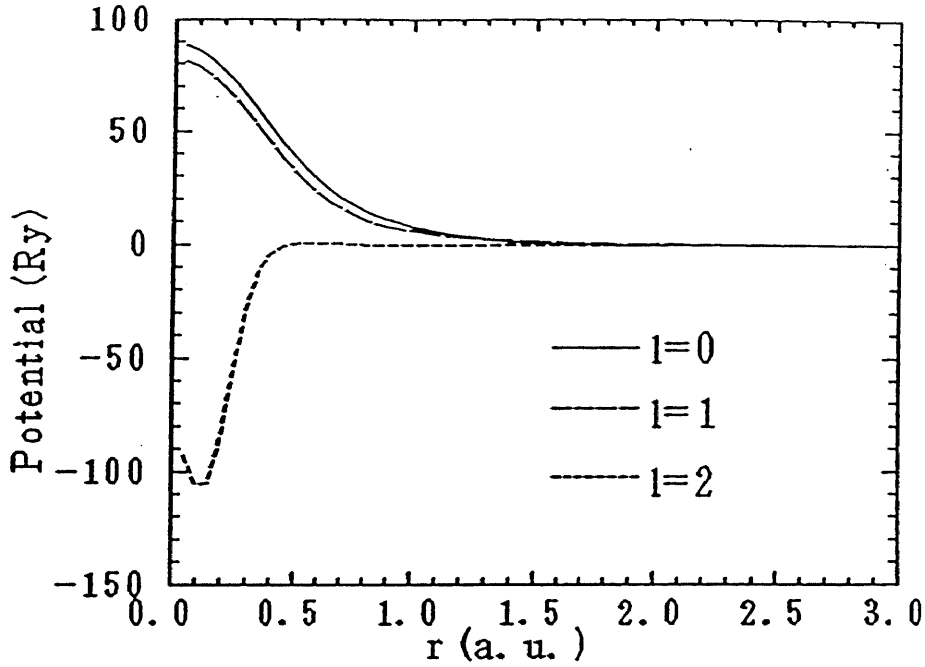

(a)

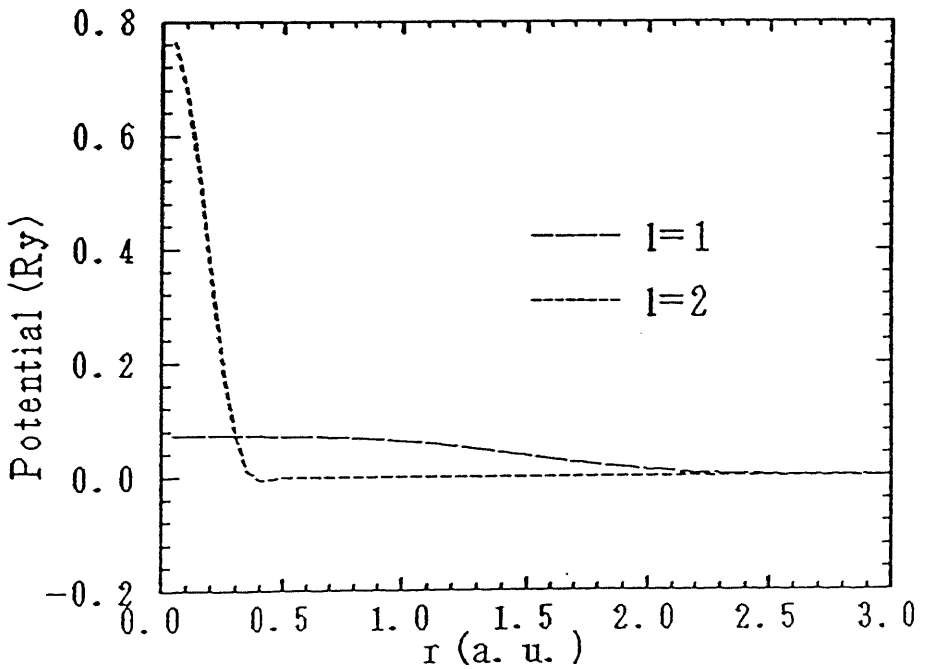

(b)

Fig.3-2. Flow chart of the procedure for solving self-consistently the effective one-electron equation(eq.(3.1)) by the iterative method. [1]Optimization of basis functions. [2]Self-consistent iteration using the optimized basis functions.

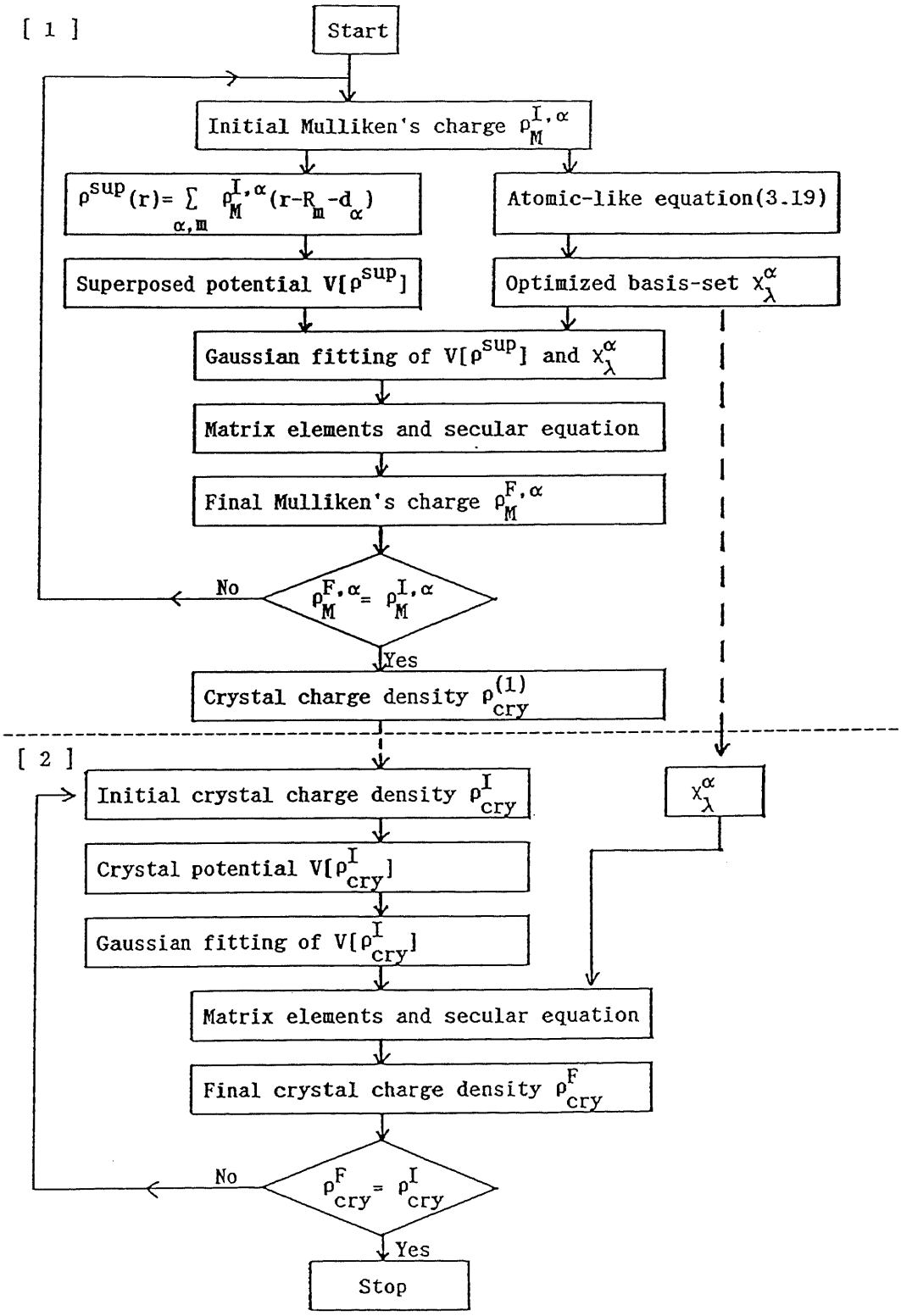

Fig.4-1. Band structure of graphite.

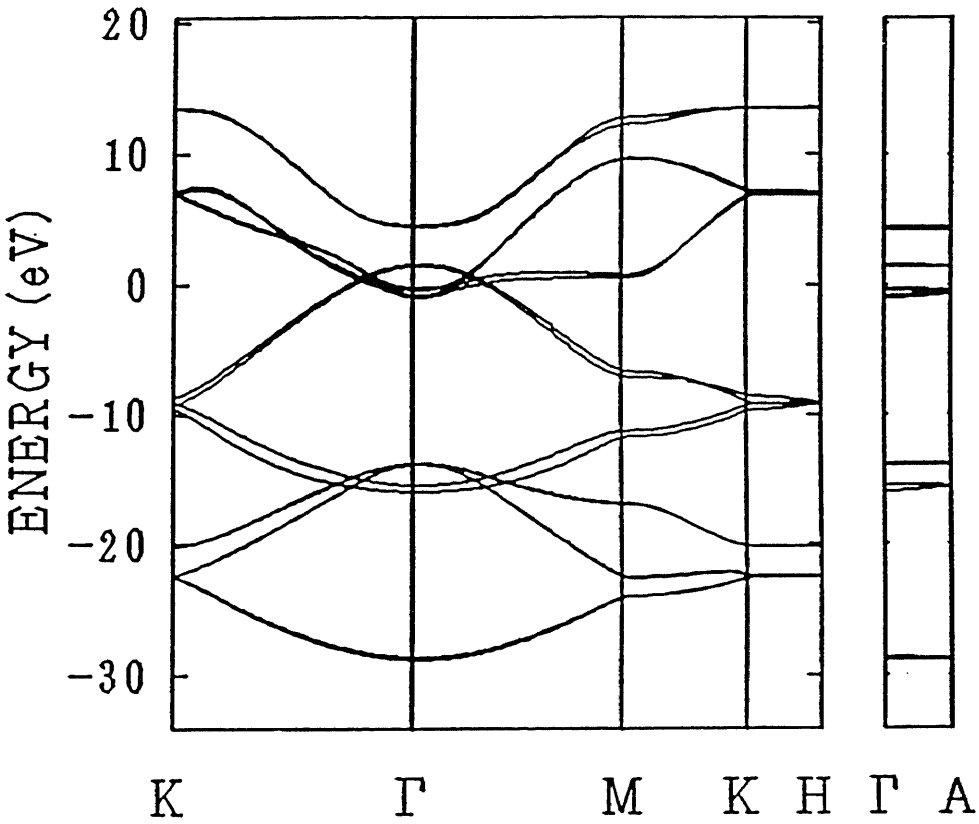

Fig.4-2. Density of states of graphite.

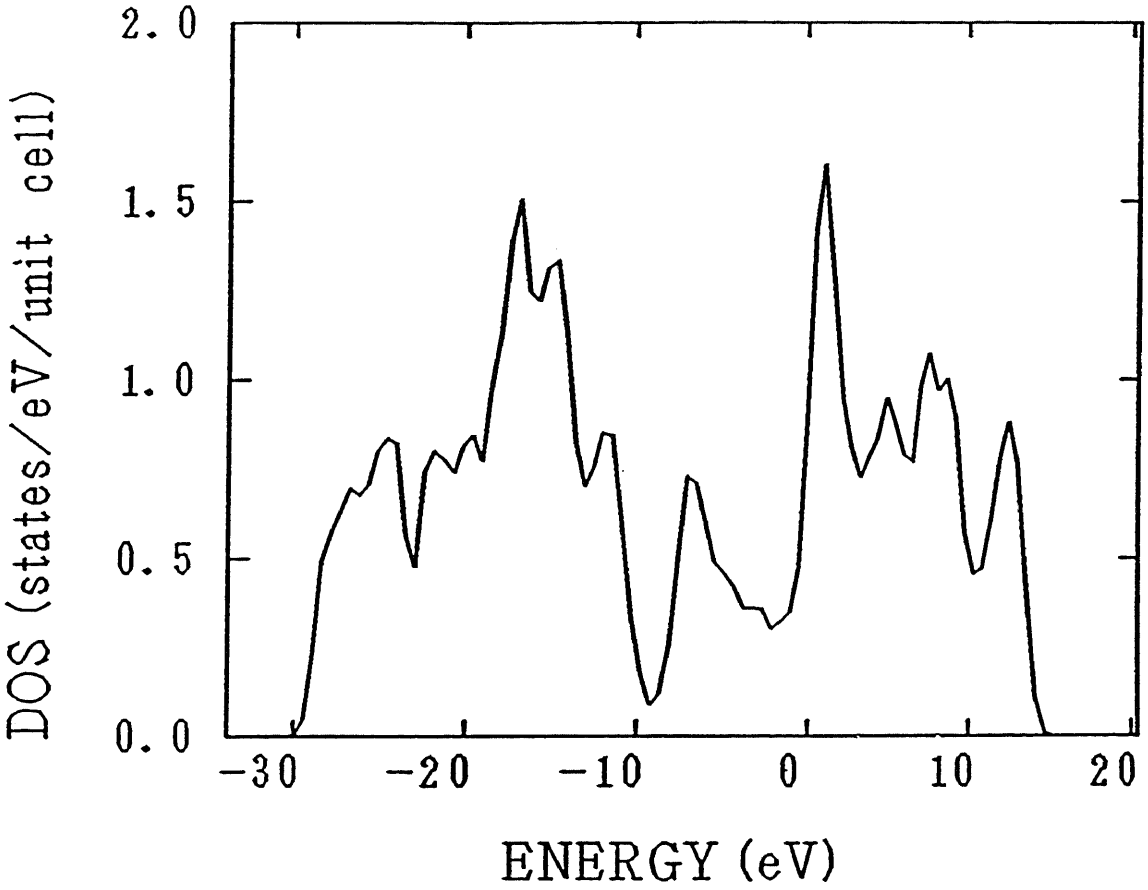

Fig.4-3. Band structure of hexagonal BN.

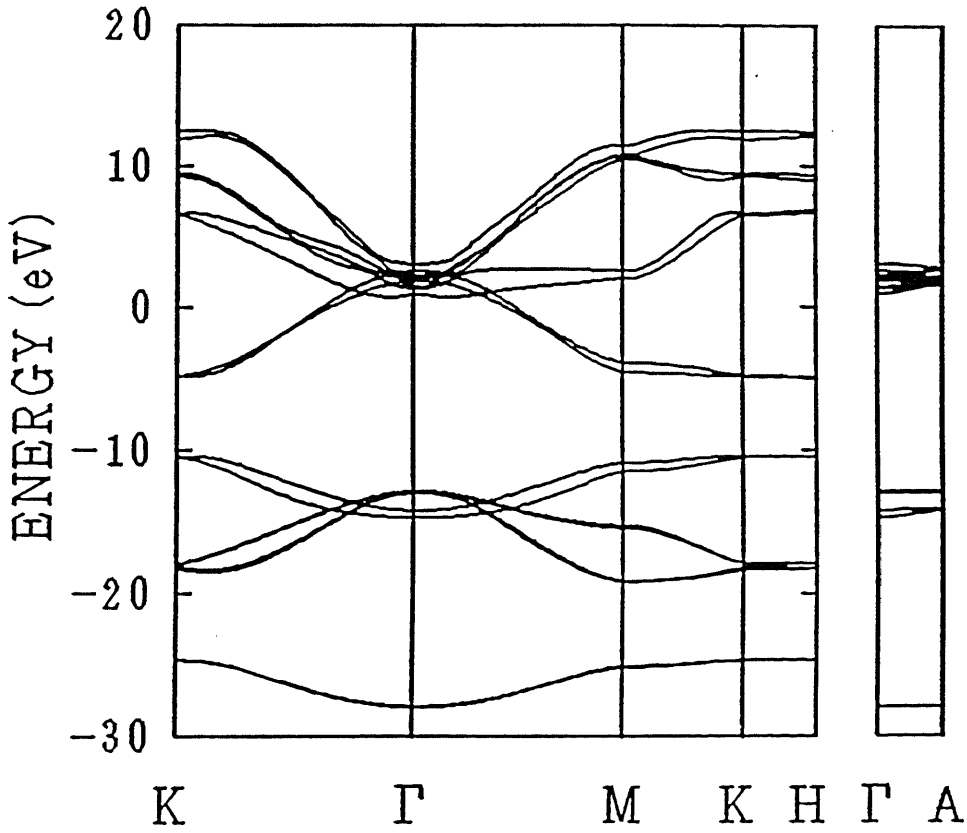

Fig.4-4. Density of states of hexagonal BN.

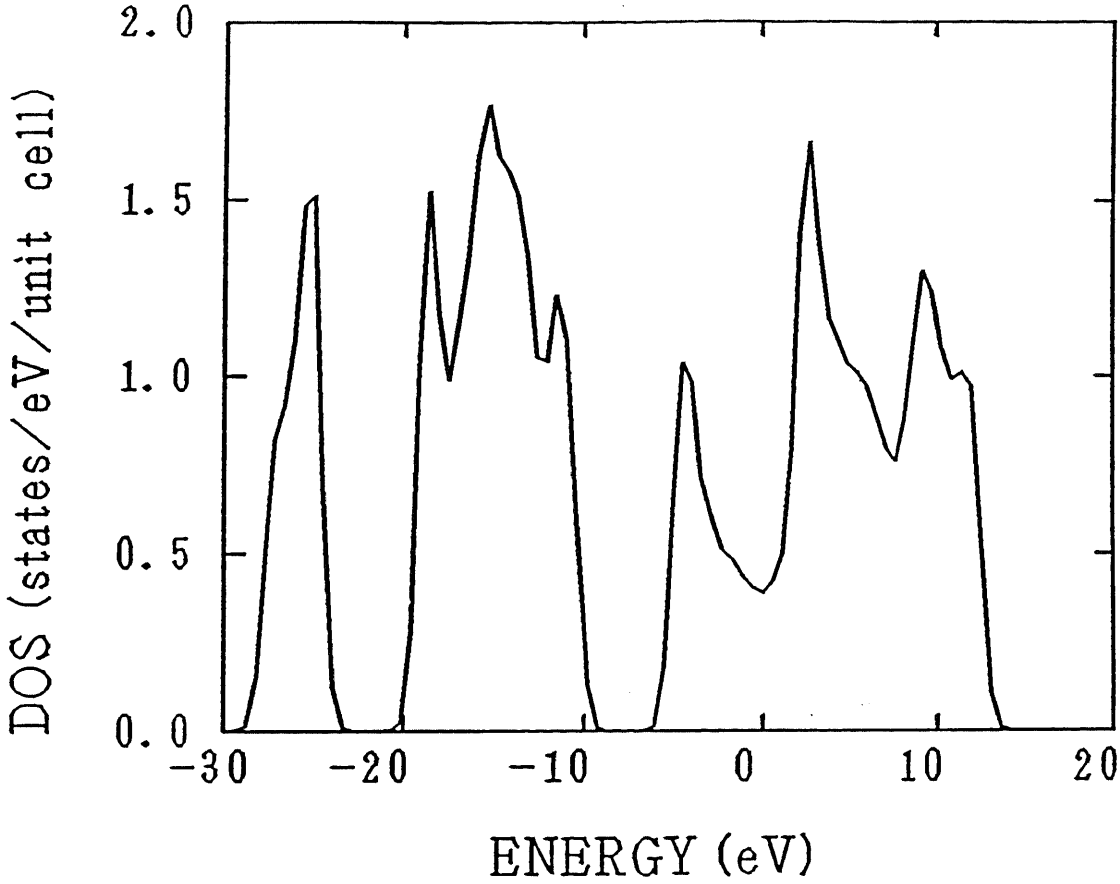

Fig.4-5. Two-dimensional band structure of $ZnPS_3$. The top of the valence band is taken as the zero of energy, and several high-symmetry points of type 1 structure are indicated.

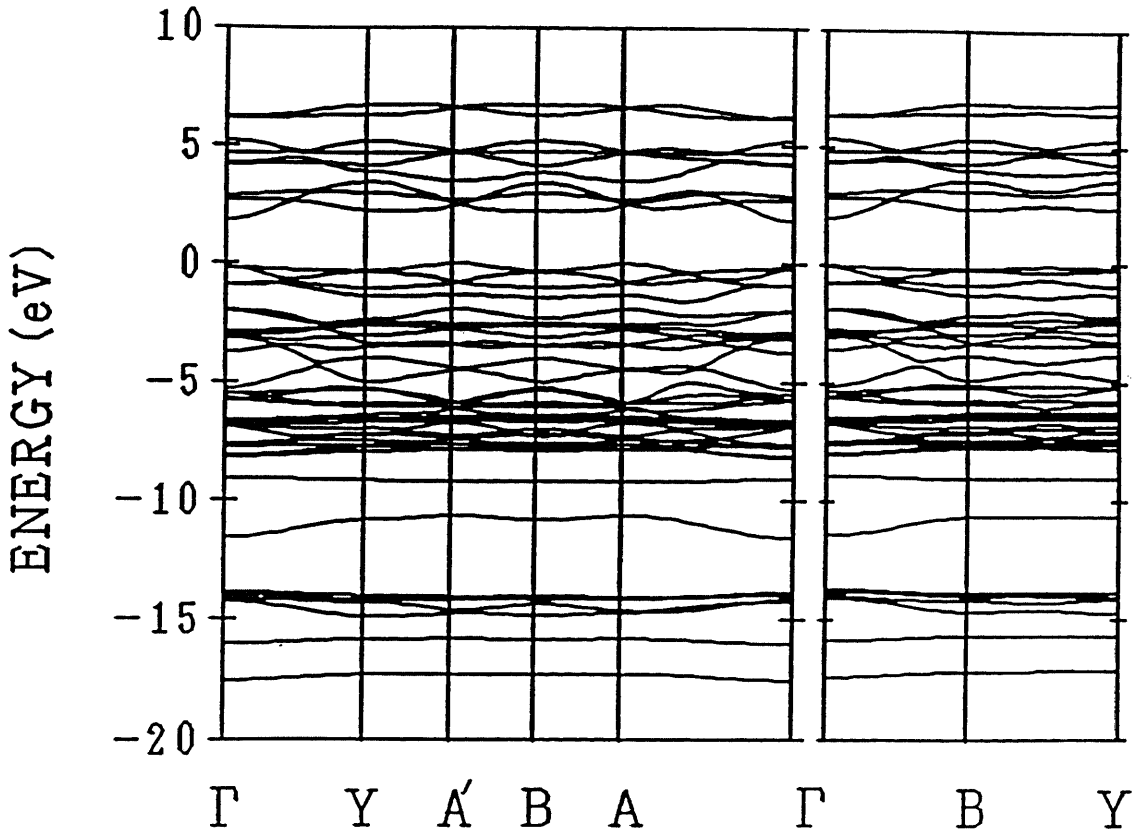

Fig.4-6. Two-dimensional band structures of $NiPS_3$ for the three types of magnetic structures: (a),(b) and (c) are for the type 1, type 2 and type 3 magnetic structure, respectively. The top of the valence band is taken as the zero of energy, and several high-symmetry points of type 1 structure are indicated.

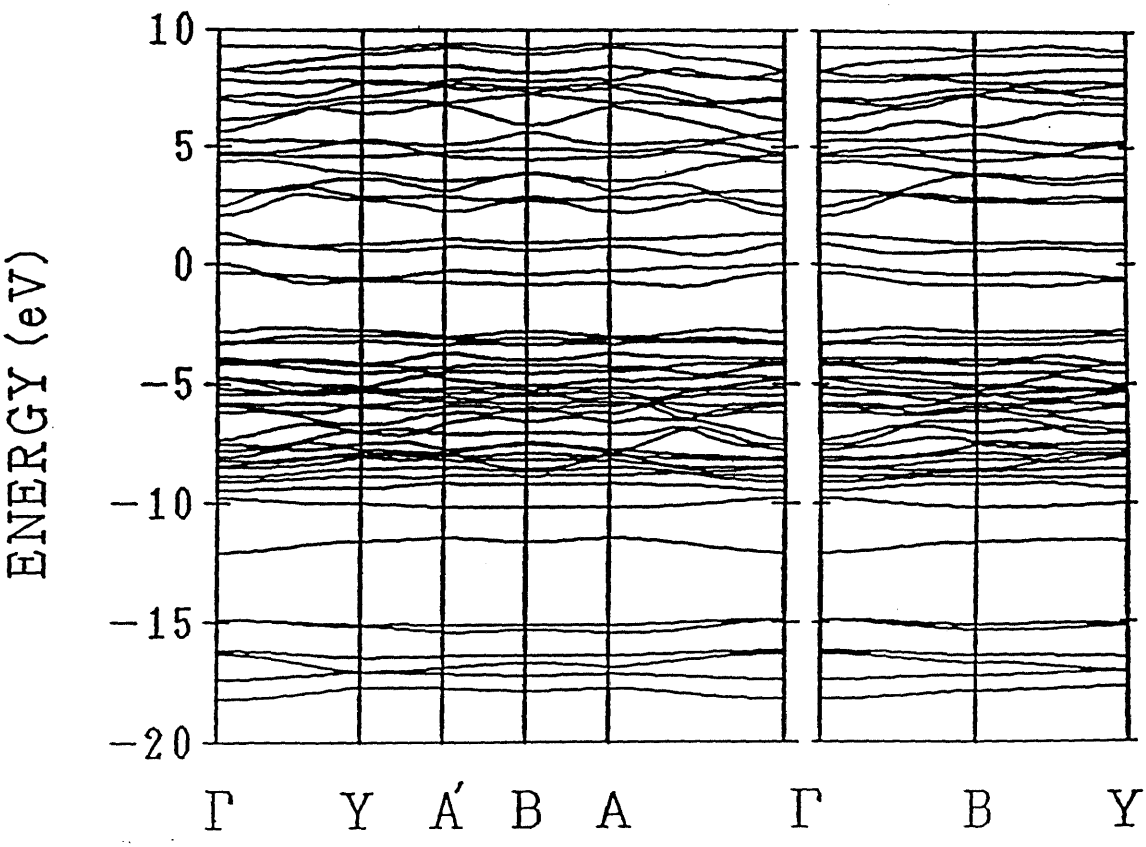

(a)

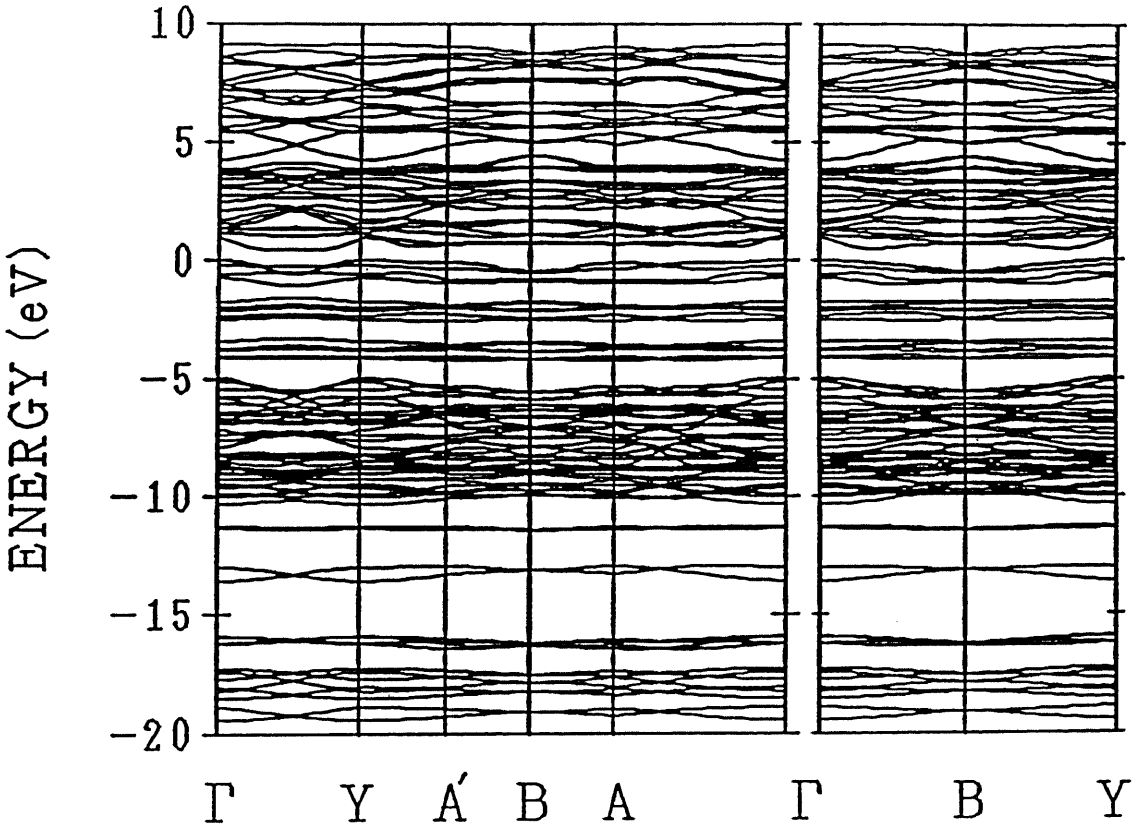

(b)

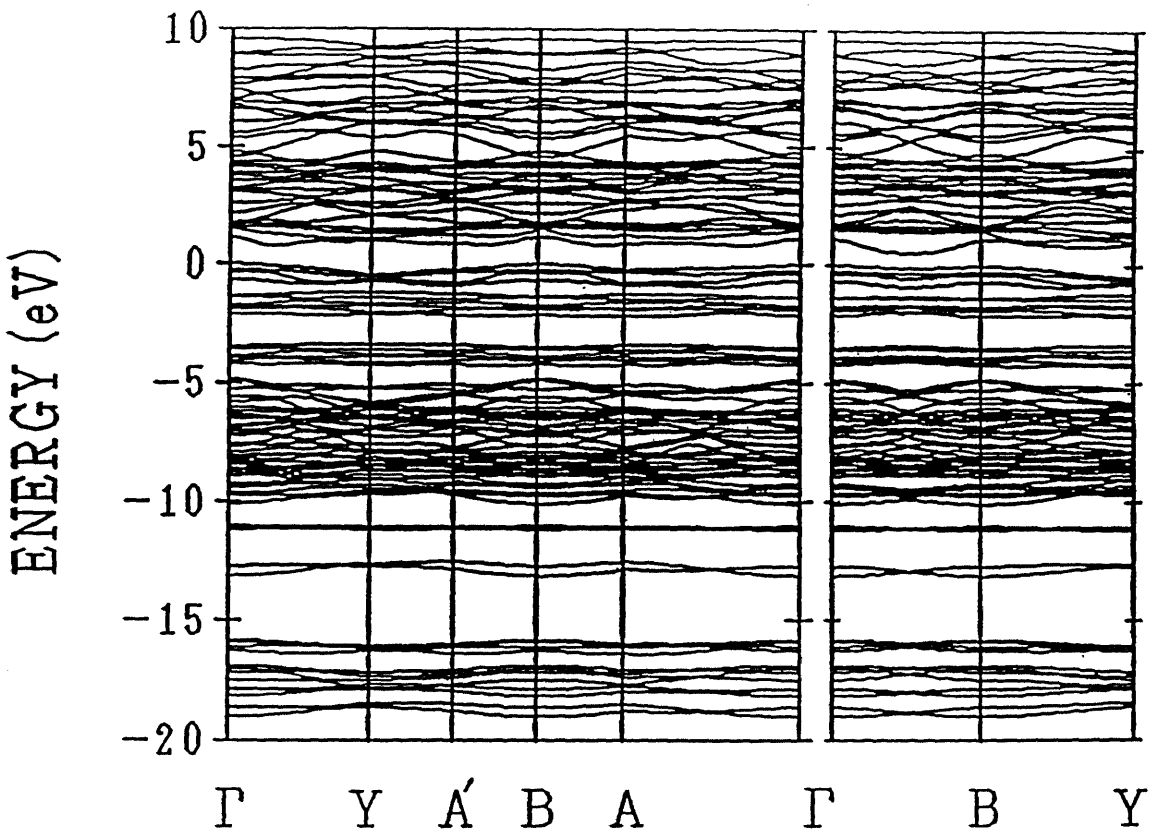

(c)

Fig.4-7. Two-dimensional band structures of $MnPS_3$ for the two types of magnetic structures: (a) and (b) are for the type 1 and type 2 magnetic structure, respectively. The top of the valence band is taken as the zero of energy, and several high-symmetry points of type 1 structure are indicated.

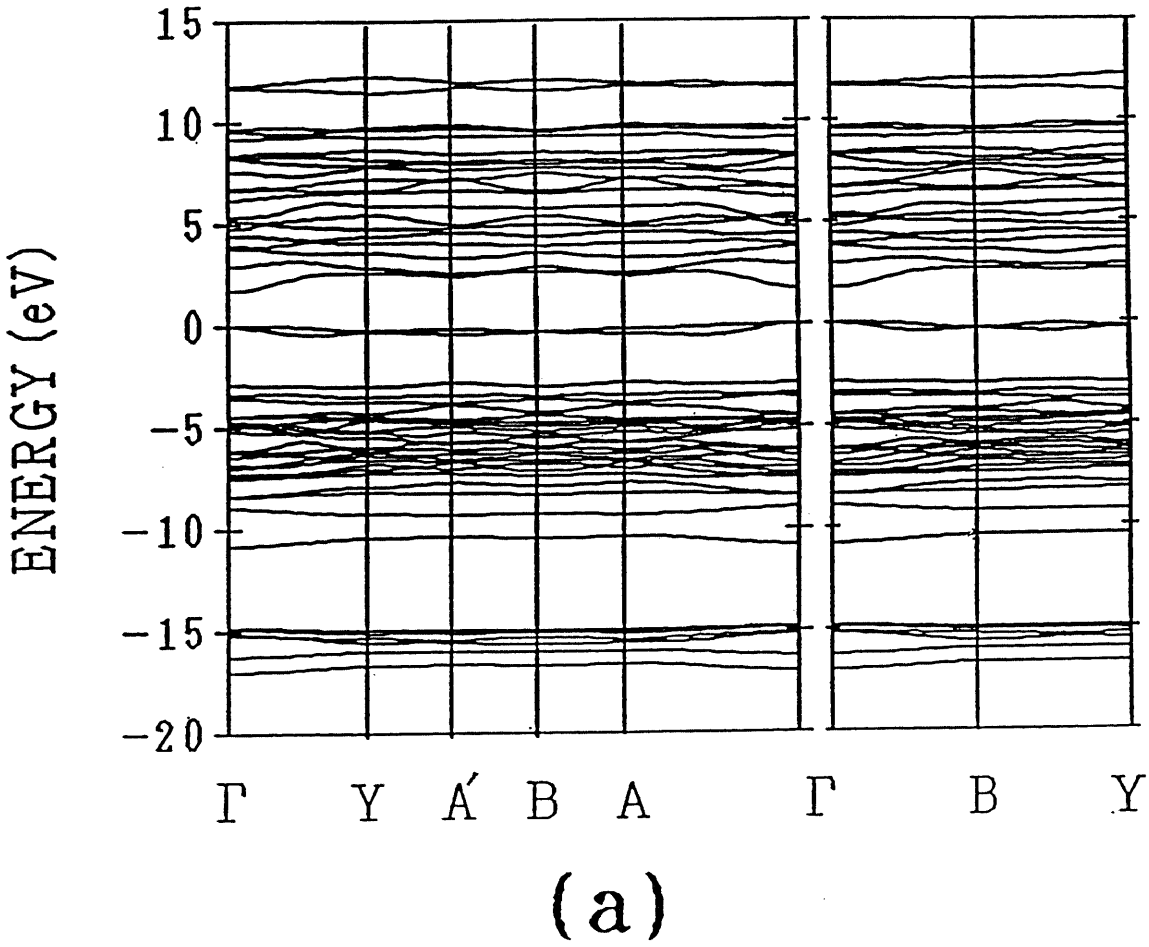

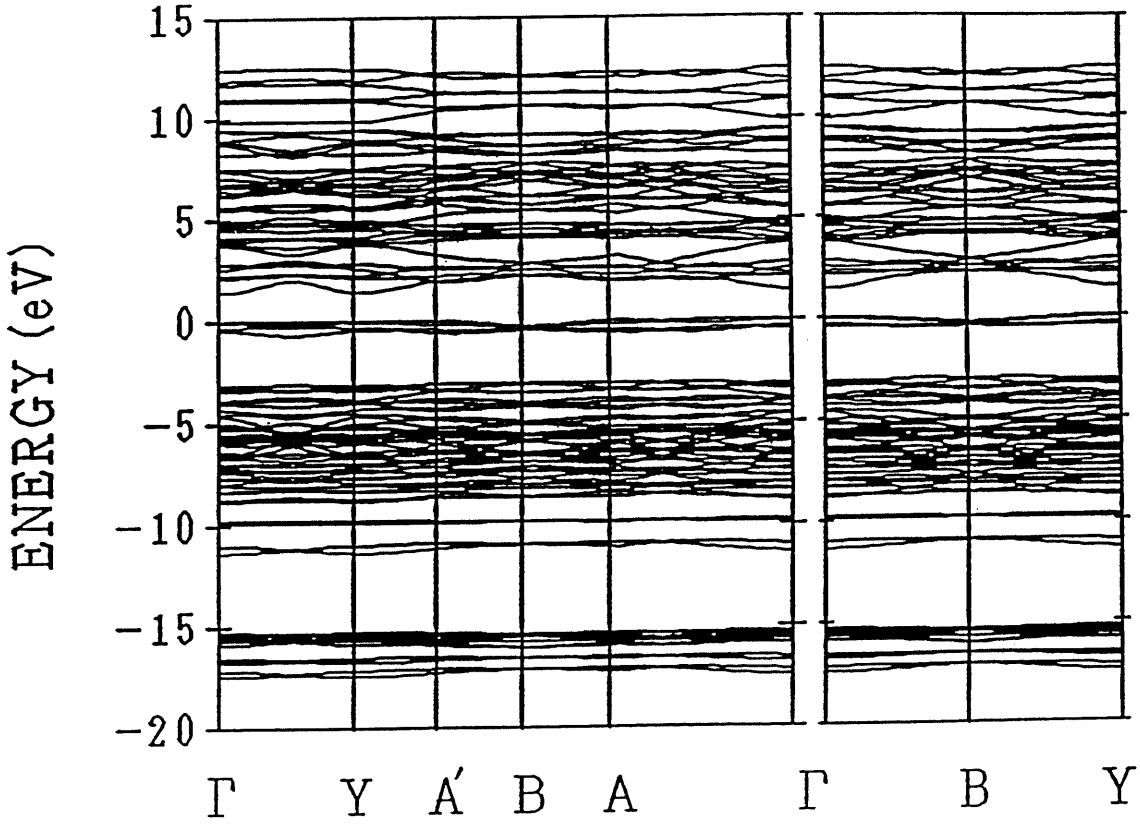

(b)

Fig.4-8. Two-dimensional band structure of $FePS_3$ for the type 2 magnetic structure. The top of the valence band is taken as the zero of energy, and several high-symmetry points of type 1 structure are indicated.

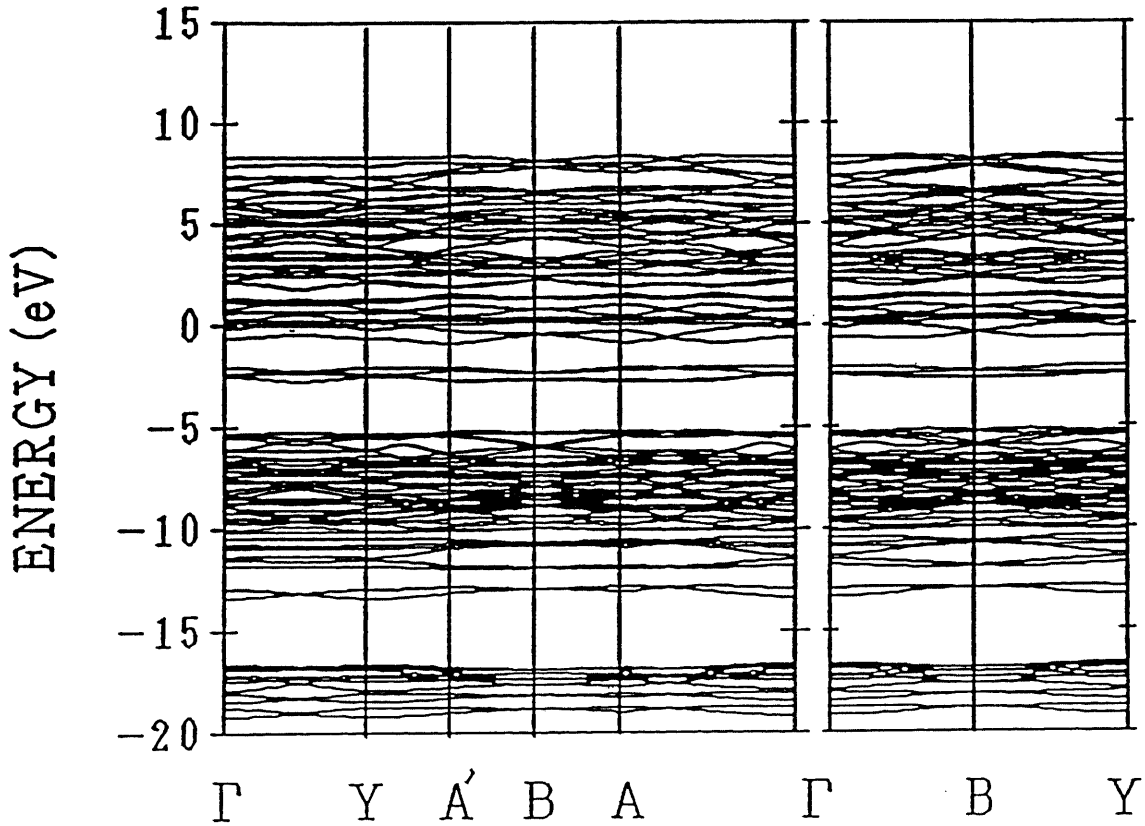

Fig.4-9. Density of states of MPS_3 family for the experimentally observed magnetic structure: (a)$ZnPS_3$, (b)$FePS_3$, (c)$NiPS_3$ and (d)$MnPS_3$. The top of the valence band is taken as the zero of energy. The character of each peak is described in Table 4-6.

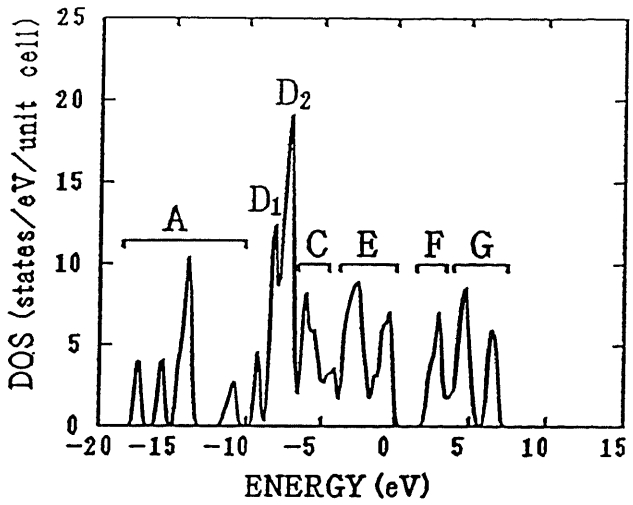

(a)$ZnPS_3$

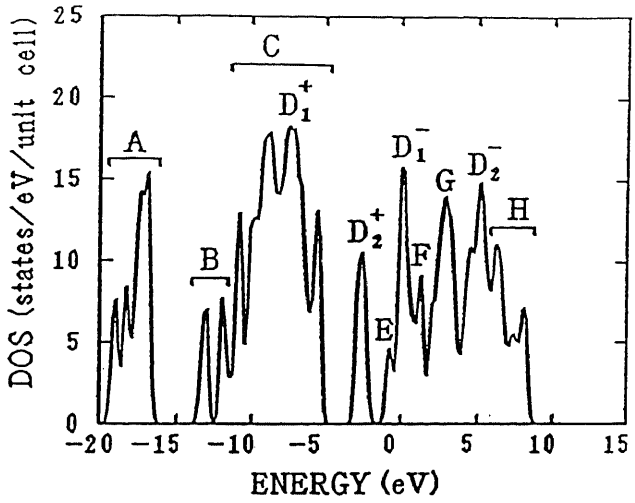

(b)$FePS_3$

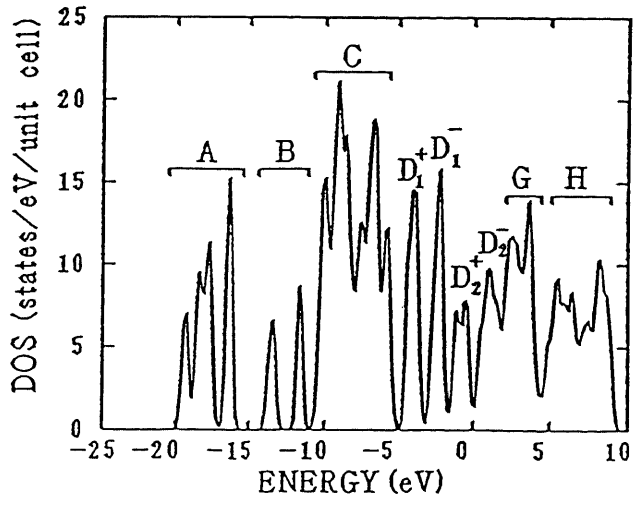

(c)$NiPS_3$

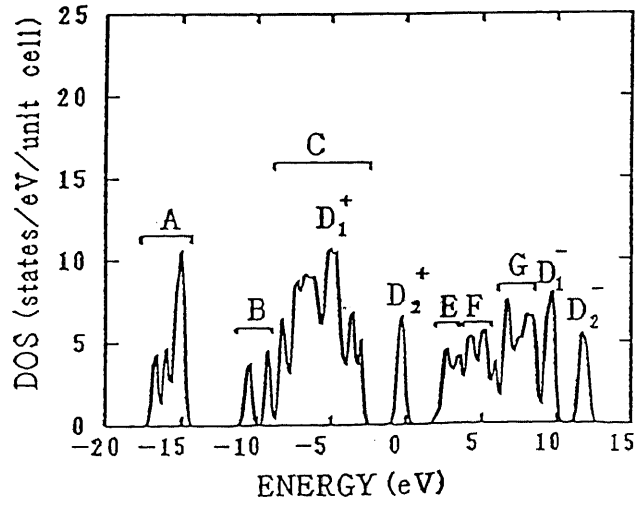

(d)$MnPS_3$

Fig.4-10. Imaginary part of the dielectric function $\varepsilon_2^{\mu}(\omega)$ of MPS_3 family for the experimentally observed magnetic structure: (a)$ZnPS_3$, (b)$FePS_3$, (c)$NiPS_3$ and (d)$MnPS_3$. The spectra for the light polarized parallel to the x, y and z axis (perpendicular to the layer)are shown. The polarization vector of light is indicated by E.

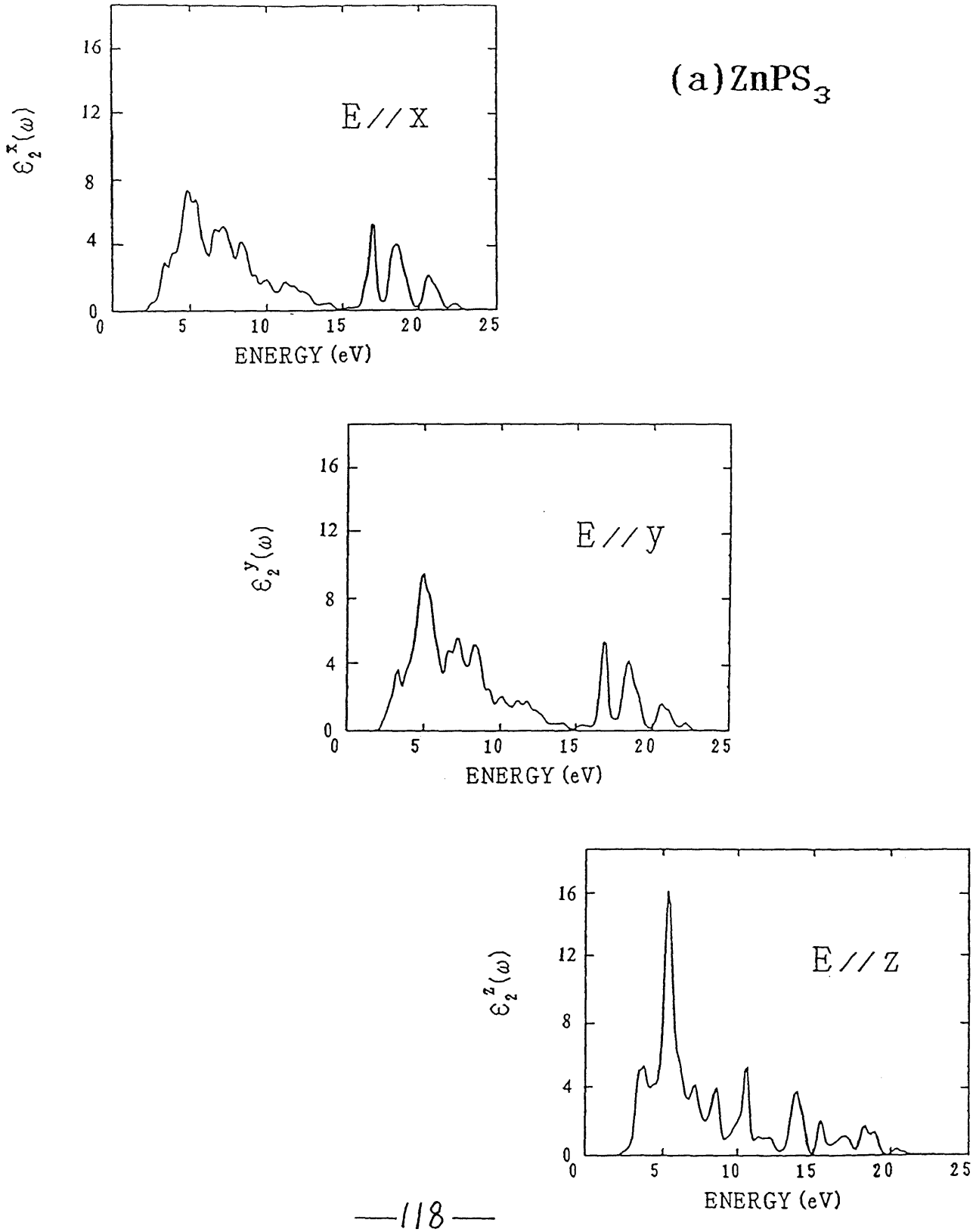

(b)$FePS_3$

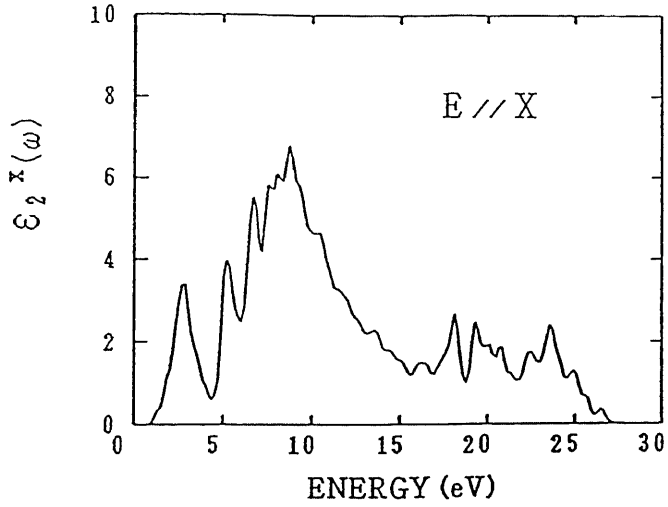
E // X
$\varepsilon_2^x(\omega)$
ENERGY (eV)

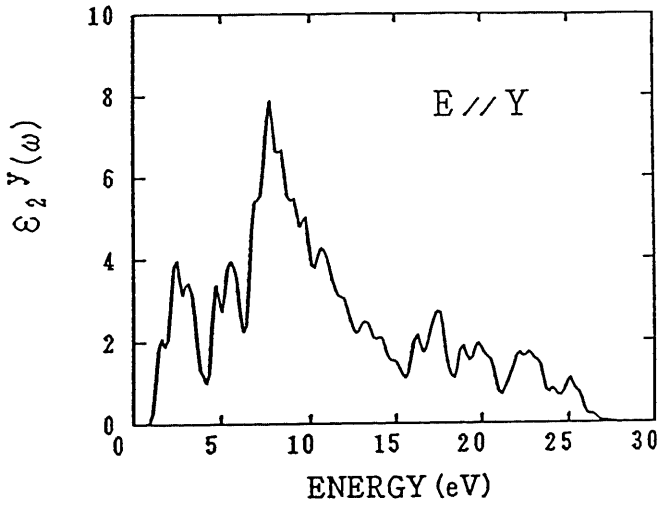
E // Y
$\varepsilon_2^y(\omega)$
ENERGY (eV)

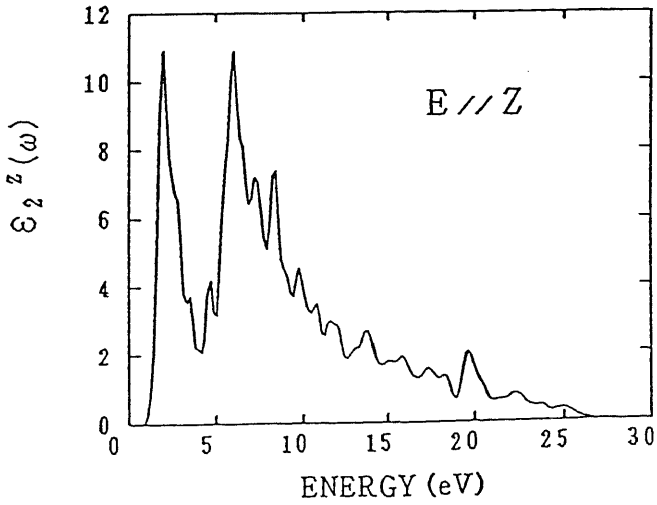
E // Z
$\varepsilon_2^z(\omega)$
ENERGY (eV)

(c)$NiPS_3$

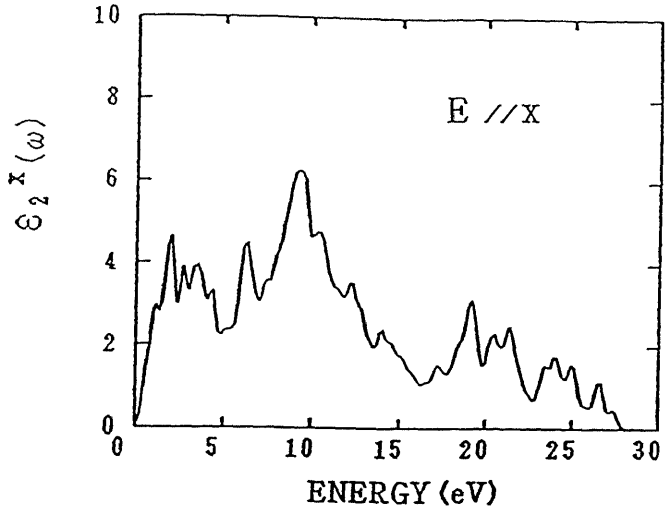
E //x
$\varepsilon_2^x(\omega)$
ENERGY (eV)

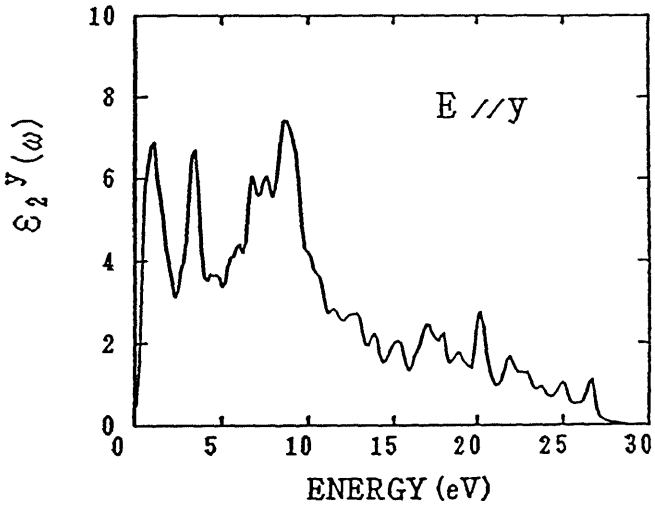
E //y
$\varepsilon_2^y(\omega)$
ENERGY (eV)

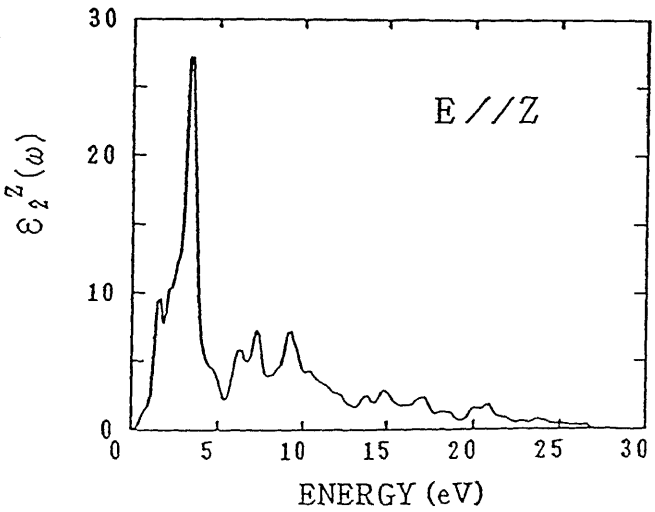
E //Z
$\varepsilon_2^z(\omega)$
ENERGY (eV)

(d)$MnPS_3$

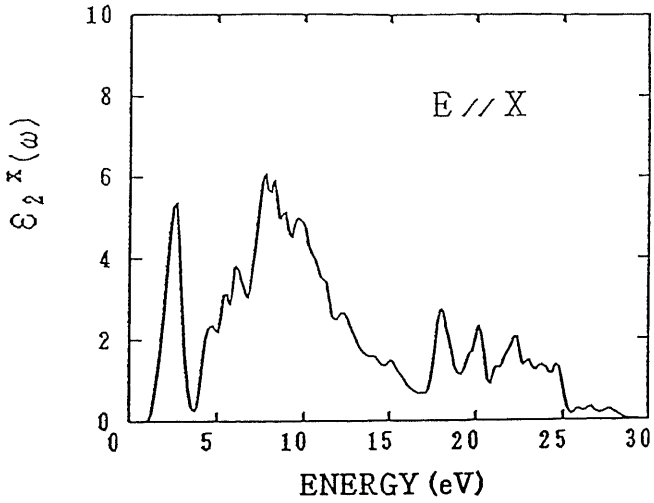
E // X
$\varepsilon_2^x(\omega)$
ENERGY (eV)

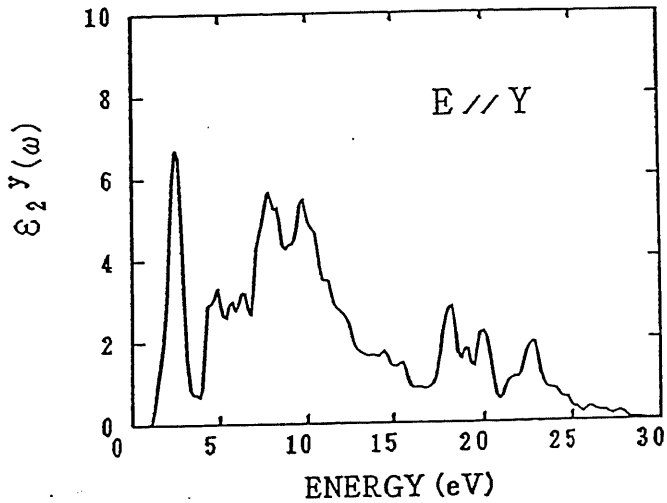
E // Y
$\varepsilon_2^y(\omega)$
ENERGY (eV)

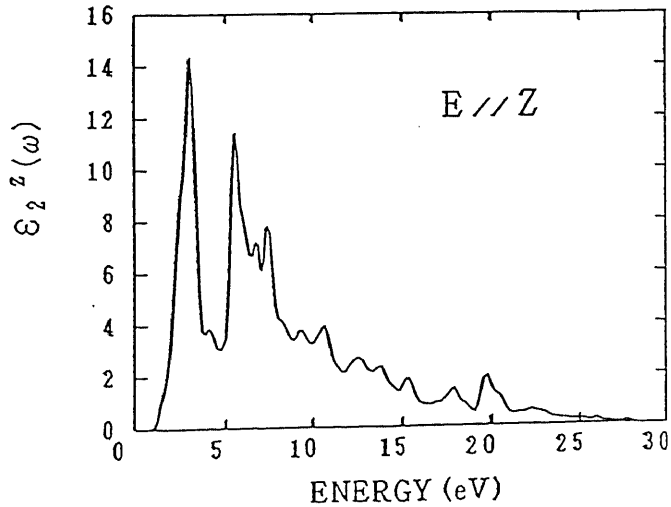
E // Z
$\varepsilon_2^z(\omega)$
ENERGY (eV)

Fig.4-11. The $\varepsilon_2^{xy}(\omega)$ spectrum for the light polarized parallel to the layer of MPS_3 family: (a)$ZnPS_3$, (b)$FePS_3$, (c)$NiPS_3$ and (d)$MnPS_3$. This is the average of the $\varepsilon_2^x(\omega)$ and $\varepsilon_2^y(\omega)$ spectra. The observed spectrum(after ref.7) is also shown by the dotted curve.

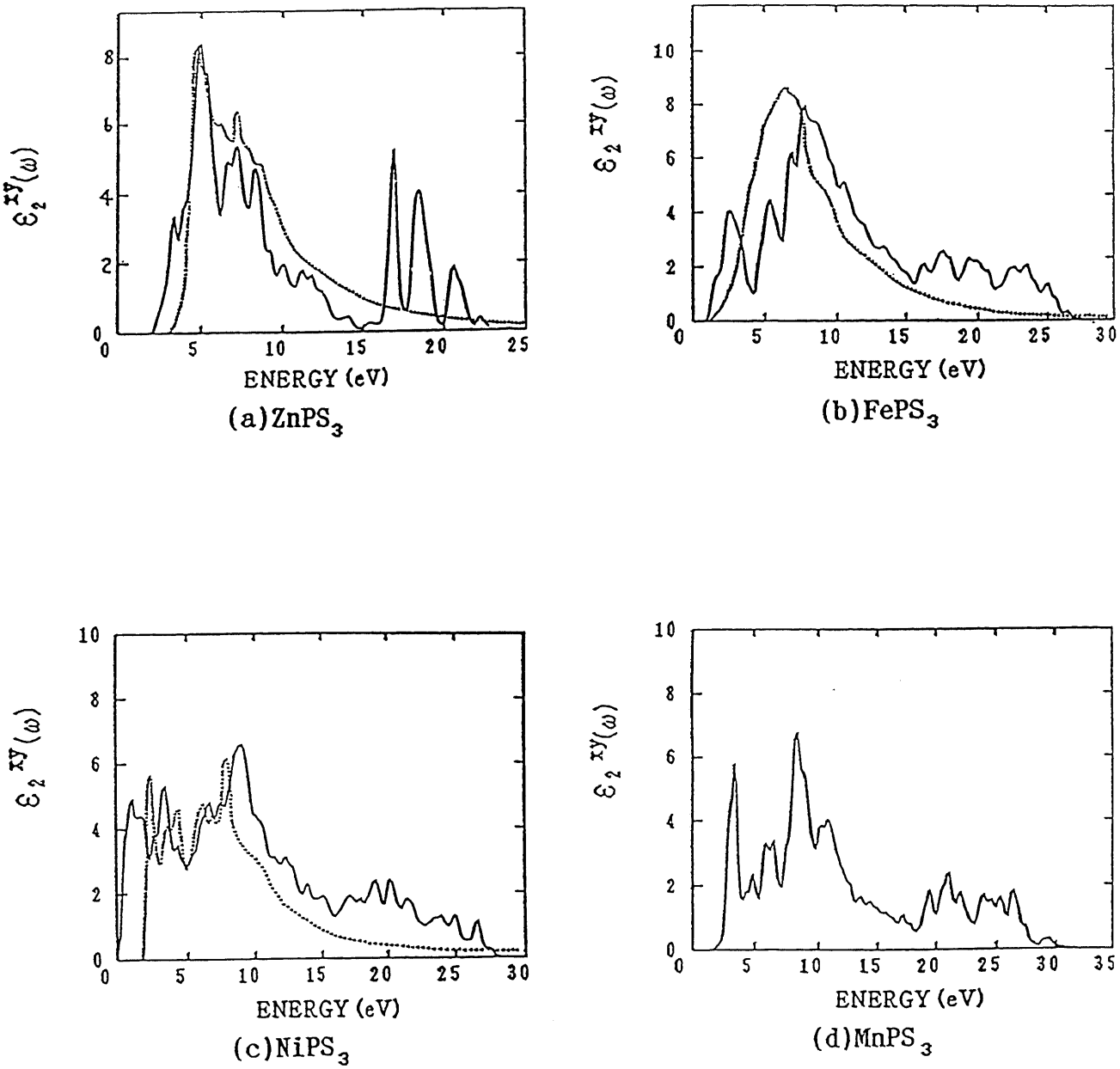

Fig.4-12. Joint density of states of MPS_3 family: (a)$ZnPS_3$, (b)$FePS_3$, (c)$NiPS_3$ and (d)$MnPS_3$. For $FePS_3$, the value of JDOS/ω^2 is very large near the 0 eV, because the band gap of $FePS_3$ is 0 eV in the present calculation.

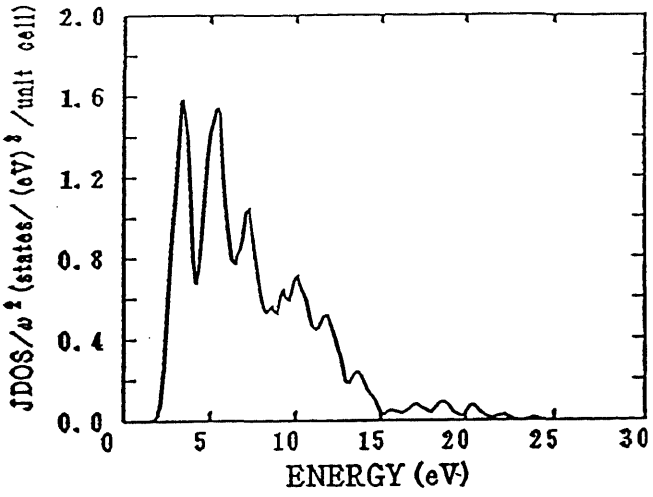

(a)$ZnPS_3$

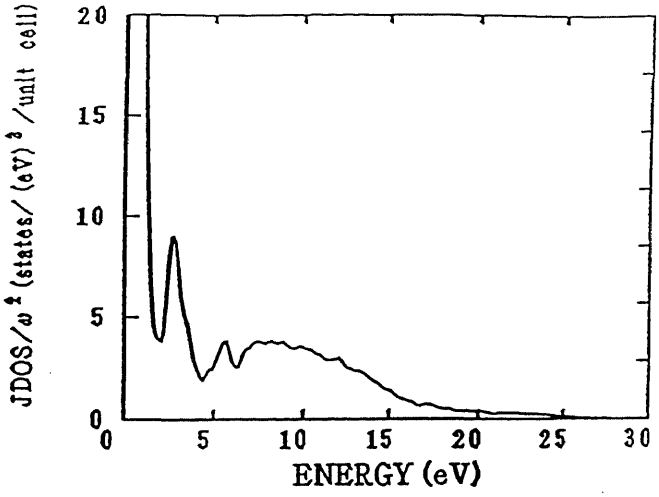

(b)$FePS_3$

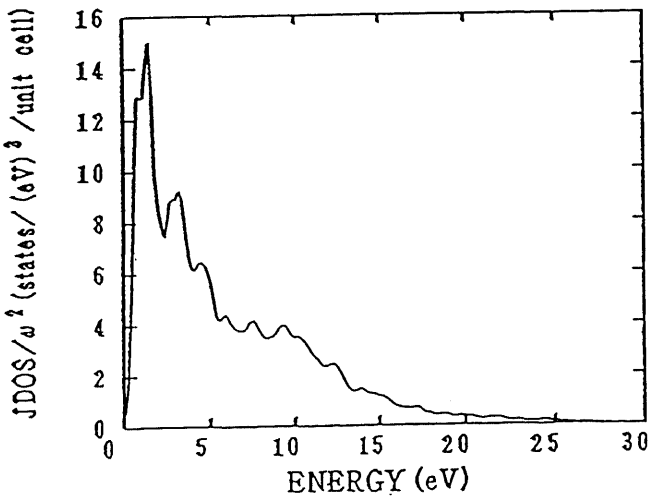

(c)$NiPS_3$

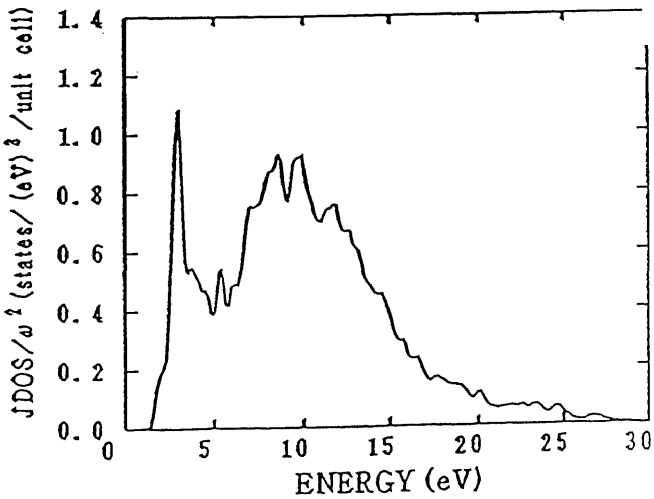

(d)$MnPS_3$

Table 2-1. Lattice parameters of MPS_3 family.

Compound	a (in Å)	b (in Å)	c (in Å)	β (in °)
$MnPS_3$	6.077	10.524	6.796	107.35[1)]
$FePS_3$	5.947	10.300	6.7222	107.16[1)]
$NiPS_3$	5.812	10.070	6.632	106.98[1)]
$ZnPS_3$	5.96	10.28	6.73	107.1 [2)]
	5.9717	10.3424	6.7565	107.139[3)]

1) After ref.12.
2) After ref.13. The band structure is calculated from these parameters.
3) After ref.14.

Table 2-2. Neel temperatures T_N of some MPX_3 family.

Compound	T_N(K)
$NiPS_3$	165
$MnPS_3$	82
$MnPSe_3$	74
$FePS_3$	116
$FePSe_3$	112

Table 2-3. Absorption edges of some MPX_3 family.

Compound	Absorption edge (eV)
$NiPS_3$	1.6
$FePS_3$	1.5
$FePSe_3$	1.3
$MnPS_3$	3.0
$MnPSe_3$	2.5
$CdPS_3$	3.5
$ZnPS_3$	3.4

Table 3-1.

Pseudopotential parameters for Zn, Ni, Fe, Mn, P and S atoms, in Rydberg unit.

Zn (The 3d electrons are included into the core.)

L	α_1	α_2	α_3	$A_1(C_1^{core})$	$A_2(C_2^{core})$	A_3	A_4	A_5	A_6
core	2.51	0.75		6.1450	-5.1450				
0	1.52	2.06	7.62	133.3925	-120.2727	2.592790	-32.91396	-22.07552	10.31245
1	1.02	1.13	1.28	68133.19	-21386.35	-46734.89	-2403.979	-9561.024	-2544.313
2	0.52	0.72	1.30	214.2509	-126.3977	-76.39794	-12.10983	-56.34877	-27.35269
spin-orbit									
1	0.46	0.70	0.86	-1.730169	-19.82481	21.62835	0.089468	2.110944	1.718862

Ni

L	α_1	α_2	α_3	$A_1(C_1^{core})$	$A_2(C_2^{core})$	A_3	A_4	A_5	A_6
core	7.60	2.74		2.6949	-1.6949				
0	1.80	2.38	3.17	767.1796	32.35041	-754.8887	-133.6142	-621.2821	-344.5597
1	1.18	2.10	2.59	246.0182	6610.423	-6815.461	-41.61576	-1851.483	-1750.638
2	2.53	23.55	26.60	4.076987	41339.53	-41386.45	-6.287621	-55486.60	-73551.80
spin-orbit									
1	0.51	1.29	1.50	-0.003324	-14.11295	14.15212	0.000770	1.642290	1.378969
2	18.01	24.17	31.75	34.81825	27.66095	-62.08451	-55.11003	-438.1564	-187.2664

Fe

L	α_1	α_2	α_3	$A_1(C_1^{core})$	$A_2(C_2^{core})$	A_3	A_4	A_5	A_6
core	6.51	1.91		2.6179	-1.6179				
0	1.67	2.06	2.33	4534.984	17813.79	-22313.06	-487.9699	-4738.150	-2599.078
1	1.22	1.77	1.96	2035.434	99159.62	-101162.3	-234.3651	-11201.37	-8951.826
2	1.95	20.17	19.00	2.922481	-278537.8	278500.7	-3.355755	-175262.1	-152378.2
spin-orbit									
1	0.28	0.40	0.51	-1.529476	-8.115585	9.678393	0.040469	0.684582	0.537337
2	15.25	23.70	30.81	2.175762	17.00275	-18.92399	-4.023834	-83.38327	-64.21139

Table 3-1.

Pseudopotential parameters for Zn, Ni, Fe, Mn, P and S atoms, in Rydberg unit.

Mn

L	α_1	α_2	α_3	$A_1(C_1^{core})$	$A_2(C_2^{core})$	A_3	A_4	A_5	A_6
core	6.03	1.63		2.7024	-1.7024				
0	1.39	1.81	2.42	518.1798	-89.96515	-396.0130	-68.51417	-268.8411	-149.8310
1	1.17	1.64	1.77	3407.673	269913.5	-273291.7	-339.4624	-20423.93	-16403.64
2	1.73	16.13	16.75	2.718595	922143.1	-922173.7	-2.775493	-273358.7	-299641.0
spin-orbit									
1	0.26	0.37	0.47	-1.306427	-7.052911	8.388640	0.031471	0.540213	0.421529
2	12.01	16.16	20.96	24.06064	27.80028	-51.68112	-25.37901	-218.4274	-102.9090

P

L	α_1	α_2	α_3	$A_1(C_1^{core})$	$A_2(C_2^{core})$	A_3	A_4	A_5	A_6
core	2.59	1.03		1.4995	-0.4995				
0	2.82	3.21	4.19	-13557.21	11697.84	1872.618	1853.900	4710.987	581.5496
1	1.83	2.15	2.51	-2514.056	-908.3026	3429.736	228.4194	1352.373	462.4933
2	2.39	2.78	3.16	72419.41	57610.65	-130025.8	-8104.344	-51018.92	-18537.18
spin-orbit									
1	0.43	0.53	0.70	-56.69114	21.64966	35.05332	1.710301	7.510671	2.425318

Sulfur

L	α_1	α_2	α_3	$A_1(C_1^{core})$	$A_2(C_2^{core})$	A_3	A_4	A_5	A_6
core	2.99	1.19		1.4261	-0.4261				
0	3.37	3.71	4.69	-42506.09	39551.16	2971.036	5428.631	11184.16	781.6639
1	2.09	2.67	3.51	-378.6493	9.849386	377.8585	58.94089	361.4033	123.9677
2	2.97	3.48	3.97	72572.55	66312.53	-138880.1	-10492.66	-68887.85	-25693.70
spin-orbit									
1	0.54	0.66	0.87	-99.25644	43.87032	55.40381	3.636713	15.25385	4.686659

Table 3-2.

Parameters of exchange-correlation energy in Rydberg unit.

Parameter	U (ζ=0)	P (ζ=1)
γ	-0.2846	-0.1686
β_1	2.1058	2.7962
β_2	0.6668	0.5222
A	0.0622	0.0311
B	-0.096	-0.0538
C	0.0040	0.0014
D	-0.0232	-0.0096

Table 3-3. Forms of Gaussian-type functions.

i	s	p_x	p_y	p_z	d_{xy}	d_{yz}	d_{zx}	$d_{x^2-y^2}$	$d_{3z^2-r^2}$
$G_i(b;r)$	1	$-\sqrt{3}x$	$-\sqrt{3}y$	$\sqrt{3}z$	$\sqrt{15}xy$	$-\sqrt{15}yz$	$-\sqrt{15}zx$	$\frac{\sqrt{15}}{2}(x^2-y^2)$	$\frac{\sqrt{5}}{2}(3z^2-r^2)$

$$[\times \frac{1}{\sqrt{4\pi}} \exp(-br^2)\ ]$$

Table 4-1. Fitting parameters of basis functions.

Carbon: 2s(1.0)2p(3.0)				Boron: 2s(2.0)2p(0.5)				Nitrogen: 2s(2.0)2p(3.5)			
$rR_{2s}(r)^{1)}$		$rR_{2p}(r)^{2)}$		$rR_{2s}(r)$		$rR_{2p}(r)$		$rR_{2s}(r)$		$rR_{2p}(r)$	
C_n	α_n	C_n	α_n	C_n	α_n	C_n	α_n	C_n	α_n	C_n	α_n
2.04	4.89	1.80	4.79	2.31	3.00	1.01	3.28	-3.13	2.65	2.95	6.16
-2.70	4.05	1.11	1.37	-2.81	2.64	0.65	0.99	2.54	2.10	1.63	1.62
0.68	0.58	0.46	0.46	0.49	0.39	0.33	0.36	0.85	0.56	0.53	0.50
0.45	0.23	0.11	0.16	0.37	0.17	0.10	0.14	0.34	0.22	0.10	0.15
0.07	0.09	0.01	0.06	0.06	0.07	0.01	0.06	0.04	0.09	0.01	0.04

Ni:3d(up-5,down-3)4s(1.0)4p(0)

Up-spin						Down-spin					
$rR_{3d}(r)^{3)}$		$rR_{4s}(r)^{1)}$		$rR_{4p}(r)^{2)}$		$rR_{3d}(r)$		$rR_{4s}(r)$		$rR_{4p}(r)$	
C_n	α_n	C_n	α_n	C_n	α_n	C_n	α_n	C_n	α_n	C_n	α_n
50.33	21.52	0.81	1.47	-0.28	0.49	49.88	21.37	0.84	1.45	-0.29	0.49
21.40	7.42	-1.39	1.01	0.29	0.38	20.96	7.31	-1.40	1.01	0.29	0.38
6.16	2.88	0.20	0.29	0.12	0.17	5.91	2.82	0.20	0.26	0.12	0.16
1.16	1.14	0.42	0.14	0.06	0.09	1.09	1.10	0.39	0.13	0.05	0.08
0.15	0.44	0.09	0.06	0.01	0.04	0.14	0.42	0.08	0.06	0.01	0.04
0.01	0.16					0.01	0.16				

Mn:3d(up-5,down-0)4s(1.0)4p(0)

Up-spin						Down-spin					
$rR_{3d}(r)$		$rR_{4s}(r)$		$rR_{4p}(r)$		$rR_{3d}(r)$		$rR_{4s}(r)$		$rR_{4p}(r)$	
C_n	α_n	C_n	α_n	C_n	α_n	C_n	α_n	C_n	α_n	C_n	α_n
26.83	14.97	-0.30	2.05	0.16	0.94	24.44	14.37	-0.23	2.02	0.07	1.07
11.53	5.35	1.46	1.32	-0.24	0.74	9.65	4.83	1.17	1.29	-0.16	0.64
3.52	2.13	-1.63	0.93	0.14	0.19	2.58	1.81	-1.40	0.86	0.13	0.20
0.73	0.87	0.46	0.14	0.08	0.09	0.48	0.69	0.44	0.13	0.08	0.09
0.10	0.35	0.12	0.06	0.01	0.04	0.07	0.26	0.11	0.06	0.01	0.04
0.01	0.14					0.005	0.10				

Fe:3d(up-5,down-1)4s(1.0)4p(0)

Up-spin						Down-spin					
$rR_{3d}(r)$		$rR_{4s}(r)$		$rR_{4p}(r)$		$rR_{3d}(r)$		$rR_{4s}(r)$		$rR_{4p}(r)$	
C_n	α_n	C_n	α_n	C_n	α_n	C_n	α_n	C_n	α_n	C_n	α_n
33.81	17.49	-0.20	2.53	0.29	0.99	32.65	17.07	-0.16	2.28	0.23	0.99
14.71	6.14	1.30	1.42	-0.37	0.85	13.62	5.82	2.60	1.21	-0.31	0.82
4.44	2.42	-1.59	0.99	0.15	0.21	3.83	2.23	-2.90	1.03	0.13	0.19
0.89	0.97	0.47	0.15	0.08	0.09	0.71	0.86	0.44	0.13	0.07	0.08
0.12	0.38	0.12	0.06	0.01	0.04	0.10	0.33	0.11	0.06	0.01	0.04
0.01	0.15					0.01	0.12				

Table 4-1. Fitting parameters of basis functions.

Zn:3d(10)4s(0.8)				P:3s(1.5)3p(3.0)				P:3s(2.0)3p(2.3)			
$rR_{3d}(r)$		$rR_{4s}(r)$		$rR_{3s}(r)$		$rR_{3p}(r)$		$rR_{3s}(r)$		$rR_{3p}(r)$	
C_n	α_n	C_n	α_n	C_n	α_n	C_n	α_n	C_n	α_n	C_n	α_n
71.79	26.80	2.72	1.52	5.77	2.30	-0.21	1.44	1.18	2.69	-0.22	1.41
31.01	9.16	-3.32	1.32	-6.57	2.11	0.40	0.66	-1.99	1.87	0.41	0.67
8.86	3.54	0.42	0.23	0.63	0.38	0.28	0.29	0.64	0.37	0.29	0.30
1.64	1.39	0.28	0.12	0.37	0.18	0.09	0.13	0.37	0.18	0.09	0.14
0.21	0.53	0.04	0.06	0.05	0.08	0.01	0.06	0.04	0.08	0.01	0.06
0.01	0.20										

S:3s(2.0)3p(4.3)				S:3s(2.0)3p(4.5)				S:3s(2.0)3p(4.6)			
$rR_{3s}(r)$		$rR_{3p}(r)$		$rR_{3s}(r)$		$rR_{3p}(r)$		$rR_{3s}(r)$		$rR_{3p}(r)$	
C_n	α_n	C_n	α_n	C_n	α_n	C_n	α_n	C_n	α_n	C_n	α_n
1.30	3.29	-0.34	1.63	1.93	3.09	-0.35	1.58	1.26	3.30	-0.37	1.50
-2.23	2.25	0.59	0.85	-2.85	2.35	0.61	0.86	-2.19	2.25	0.65	0.85
0.71	0.48	0.35	0.34	0.70	0.48	0.34	0.34	0.71	0.48	0.33	0.32
0.45	0.22	0.09	0.14	0.44	0.22	0.09	0.13	0.43	0.21	0.07	0.12
0.07	0.09	0.01	0.05	0.07	0.09	0.01	0.05	0.06	0.09	0.01	0.04

S:3s(2.0)3p(4.7)			
$rR_{3s}(r)$		$rR_{3p}(r)$	
C_n	α_n	C_n	α_n
2.22	3.05	-0.33	1.52
-3.13	2.40	0.64	0.81
0.73	0.46	0.31	0.30
0.40	0.20	0.07	0.11
0.06	0.08	0.005	0.04

1) $rR_s(r) = r \sum_{n=1}^{5} C_n \exp(-\alpha_n r^2)$, 2) $rR_p(r) = r^2 \sum_{n=1}^{5} C_n \exp(-\alpha_n r^2)$.

3) $rR_d(r) = r^3 \sum_{n=1}^{6} C_n \exp(-\alpha_n r^2)$.

Table 4-2.

Damping radii of carbon, boron and nitrogen atoms. The D_A and D_P are the damping radii of the atomic orbital and potential, respectively (in atomic unit).

Atom	$D_A(2s)$	$D_A(2p)$	D_P
C:2s(1)2p(3)	6.0	8.0	3.0
B:2s(2)2p(0.5)	7.5	8.5	3.0
N:2s(2)2p(3.5)	5.5	7.5	3.0

Table 4-3.

Damping radii of zinc, nickel, manganese, iron, phosphorus and sulfur atoms. The D_A and D_P are the damping radii of the atomic orbital and potential, respectively (in atomic unit).

Atom		$D_A(3d)$	$D_A(4s)$	$D_A(4p)$	D_P
Zn:3d(10)4s(0.8)4p(0)		4.0	6.0		2.0
Ni:3d(up-5,down-3)4s(1)4p(0)	up-state	3.95	6.90	9.05	2.0
	down-state	4.10	6.95	9.10	2.0
Mn:3d(up-5,down-0)4s(1)4p(0)	up-state	4.40	7.45	9.45	2.0
	down-state	5.50	7.55	9.60	2.0
Fe:3d(up-5,down-1)4s(1)4p(0)	up-state	4.30	7.30	9.30	2.0
	down-state	4.90	7.60	9.70	2.0

Atom	$D_A(3s)$	$D_A(3p)$	D_P
P:3s(1.5)3p(3)	5.25	6.80	2.7
P:3s(2)3p(2.3)	5.20	6.60	2.6
S:3s(2)3p(4.3)	5.00	7.20	2.7
S:3s(2)3p(4.5)	5.20	7.60	2.8
S:3s(2)3p(4.6)	5.20	7.80	2.8
S:3s(2)3p(4.7)	5.20	8.10	2.8

Table 4-4. Main features of the band structures of MPS_3 family.

Compound	Band Gap(eV)	Lower Conduction Bands	Higher Valence Bands
$ZnPS_3$	2.0 (indirect)	Zn-4s, P-3s, S-3p	S-3p
$NiPS_3$[1)]	0.6 (direct)	Down-spin Ni-3d e_g, Ni-4s, P-3s	Up-spin Ni-3d e_g
$NiPS_3$[2)]	0.5 (indirect)	P-3s, S-3p, Down-spin Ni-3d e_g	Up-spin Ni-3d e_g
$NiPS_3$[3)]	0.7 (direct)	P-3s, S-3p, Down-spin Ni-3d e_g	Up-spin Ni-3d e_g
$MnPS_3$[1)]	1.7 (direct)	Up-spin Mn-4s, 4p, P-3s, S-3p	Up-spin Mn-3d e_g
$MnPS_3$[2)]	1.4 (direct)	Up-spin Mn-4s, P-3s	Up-spin Mn-3d e_g S-3p
$FePS_3$	0.0	Down-spin Fe-3d t_{2g}	Up-spin Fe-4s Down-spin Fe-3d t_{2g}

1) For the type 1 magnetic structure.
2) For the type 2 one.
3) For the type 3 one.

Table 4-5.

Self-consistent Mulliken's charges and valencies of each ion in MPS_3 family.

Compound		Up-spin	Down-spin	Total	Spin-polarization	Valency
	Zn	5.35	5.35	10.70	0	+1.30
$ZnPS_3$	P	2.15	2.15	4.30	0	+0.70
	S_1	3.35	3.35	6.70	0	-0.70
	S_2	3.325	3.325	6.65	0	-0.65
	Ni	5.30	4.46	9.76	0.84	+0.24
$NiPS_3$[1)]	P	1.66	1.66	3.32	0	+1.68
	S_1	3.20	3.20	6.40	0	-0.40
	S_2	3.38	3.38	6.76	0	-0.76
	Ni	4.94	3.91	8.85	1.03	+1.15
	P	1.925	1.925	3.85	0	+1.15
$NiPS_3$[2)]	S_1	3.24	3.24	6.48	0	-0.48
	S_2	3.40	3.51	6.91	-0.11	-0.91
	S_3	3.51	3.40	6.91	0.11	-0.91
	Ni	4.95	3.73	8.68	1.22	+1.32
	P	1.875	1.875	3.75	0	+1.25
	S_1	3.49	3.49	6.98	0	-0.98
$NiPS_3$[3)]	S_2	3.34	3.27	6.61	0.07	-0.61
	S_3	3.27	3.34	6.61	-0.07	-0.61
	S_4	3.54	3.44	6.98	0.10	-0.98
	S_5	3.44	3.54	6.98	-0.10	-0.98
	Mn	5.38	0.72	6.10	4.66	+0.90
$MnPS_3$[1)]	P	1.60	1.60	3.20	0	+1.80
	S_1	3.47	3.47	6.94	0	-0.94
	S_2	3.44	3.44	6.88	0	-0.88
	Mn	5.34	0.61	5.95	4.73	+1.05
	P	1.60	1.60	3.20	0	+1.80
$MnPS_3$[2)]	S_1	3.50	3.50	7.00	0	-1.00
	S_2	3.46	3.465	6.925	-0.005	-0.925
	S_3	3.465	3.46	6.925	0.005	-0.925
	Fe	5.50	1.55	7.05	3.95	+0.95
	P	1.765	1.765	3.53	0	+1.47
$FePS_3$	S_1	3.35	3.35	6.70	0	-0.70
	S_2	3.38	3.48	6.86	-0.10	-0.86
	S_3	3.48	3.38	6.86	0.10	-0.86

1) For the type 1 magnetic structure.
2) For the type 2 one.
3) For the type 3 one.

Table 4-6.

The character of each peak in the density of states of MPS_3 family.

Compound	Peak	Main character
$ZnPS_3$	A	S 3s, P 3s
	C	P 3p, S 3p, Zn 3d
	D_1	Zn 3d t_{2g}
	D_2	Zn 3d e_g
	E	S 3p
	F	Zn 4s, P 3s, S 3p
	G	P 3p, S 3p
$FePS_3$	A	S 3s
	B	P 3s
	C	S 3p
	D_1^+	up-spin Fe 3d t_{2g}, S 3p
	D_2^+	up-spin Fe 3d e_g
	E	up-spin Fe 4s, down-spin Fe 3d t_{2g}
	D_1^-	down-spin Fe 3d t_{2g}
	F	P 3s
	G	down-spin Fe 4s, P 3p
	D_2^-	down-spin Ni 3d e_g, up-spin Fe 4p
	H	P 3p, down-spin Fe 4p
$NiPS_3$	A	S 3s
	B	P 3s
	C	S 3p
	D_1^+	up-spin Ni 3d t_{2g}
	D_1^-	down-spin Ni 3d t_{2g}
	D_2^+	up-spin Ni 3d e_g
	D_2^-	P 3s, S 3p, down-spin Ni 3d e_g
	G	P 3p, Ni 4s
	H	Ni 4p
$MnPS_3$	A	S 3s
	B	P 3s, S 3p
	C	S 3p
	D_1^+	up-spin Mn 3d t_{2g}, S 3p
	D_2^+	up-spin Mn 3d e_g
	E	up-spin Mn 4s 4p, P 3s, S 3p
	F	P 3p, down-spin Mn 4s
	G	down-spin Mn 4p
	D_1^-	down-spin Mn 3d t_{2g}
	D_2^-	down-spin Mn 3d e_g

Table 4-7.

The main features in the $\varepsilon_2(\omega)$ spectrum for the light polarized parallel to the layer: (a)$ZnPS_3$, (b)$FePS_3$, (c)$NiPS_3$ and (d)$MnPS_3$. The experimental value is after ref.7. The calculated value is the average of the $\varepsilon_2^x(\omega)$ and $\varepsilon_2^y(\omega)$ spectra. The probable assignment is also indicated. M^+ and M^- denote the up-spin and down-spin transition metals, respectively; $3d_1$ and $3d_2$ are the 3d t_{2g} and 3d e_g states, respectively.

(a) $ZnPS_3$

Experimental		Calculated		
Energy(eV)	Features	Energy(eV)	Features	Assignment
4.4	shoulder[a)]	3.4	peak	S 3p → Zn 4s
5.0	double peak	4.0	shoulder	S 3p → P 3s
5.75	shoulder[a)]	4.9	peak	S 3p → S 3p
6.3-6.4	peak	5.3	shoulder	S 3p → S 3p
7.25	peak	6.6	peak	S 3p → P 3p
7.8	peak	7.2	peak	S 3p → P 3p
8.6	peak	8.3	peak	P 3p → P 3s
9.2-9.5	shoulder	9.1	shoulder	Zn 3d→ Zn 4s
11.5[b)]	shoulder	10.0	small peak	Zn 3d→ P 3s
12.7[b)]	peak	11.2	small peak	Zn 3d→ S 3p
15.5[b)]	peak	11.7	small peak	Zn 3d→ S 3p
16.7[b)]	shoulder	12.3	shoulder	Zn 3d→ P 3p
18.3[b)]	shoulder	14.1	shoulder	Zn 3d→ P 3p
		16.9	peak	S 3s → S 3p
		18.5	peak	S 3s → S 3p
		20.6	peak	S 3s → S 3p
		22.1	shoulder	P 3s → P 3s

a) Resolved in the reflectivity spectrum.

b) Clearly present in the $\omega^2\varepsilon_2(\omega)$ spectrum.

(b) $FePS_3$

Experimental		Calculated		
Energy (eV)	Features	Energy (eV)	Features	Assignment
4.3	shoulder	1.7	shoulder	$Fe^{+}3d_2$/ $Fe^{+}4s$ →
5.4	shoulder	2.5	peak	$Fe^{-}3d_1$
6.3-6.4	peak	5.4	peak	S 3p → $Fe^{-}3d_1$
7.25	peak	6.9	peak	$Fe^{+}3d_2$→
7.8	shoulder	7.7	peak	Higher conduction
8.6	shoulder	8.3-8.5	shoulder	bands
9.2-9.5	shoulder	9.7	shoulder	or
12.4[b)]	peak	10.5	peak	Lower S 3p, $Fe^{+}3d_1$→
15.3[b)]	shoulder	11.8	shoulder	Lower conduction
17.5[b)]	shoulder	13.1-13.3	shoulder	bands
		16.2	small peak	
		17.6	small peak	S 3s, P 3s →
		19.6	small peak	
		22.6	small peak	
		23.5	small peak	Conduction Bands
		25.0	small peak	

(c) $NiPS_3$

Experimental		Calculated		
Energy (eV)	Features	Energy (eV)	Features	Assignment
2.15	peak	1.1	peak	Ni^+ $3d_2$ →
3.3	peak	1.7	shoulder	Ni^- $3d_2$
4.0	peak	2.7	shoulder	Ni^- $3d_1$ →
5.0	shoulder	3.5	peak	Ni^- $3d_2$
5.75	peak	4.3	shoulder	
6.3-6.4	peak	6.7	peak	Ni^+,Ni^- 3d →
7.25	peak	7.6	shoulder	conduction
7.8	shoulder	8.9-9.1	peak	bands
8.6	shoulder	10.1	shoulder	or
9.2-9.5	shoulder	11.5	shoulder	S 3p →
12.4[b)]	shoulder	12.3	peak	conduction
18.3[b)]	shoulder	13.9	peak	bands
		15.0	shoulder	
		17.1	small peak	
		17.9	small peak	
		19.1	peak	P 3s,S 3s →
		20.1	peak	
		21.4	small peak	conduction
		23.9	small peak	bands
		25.0	small peak	
		26.6	small peak	
		27.3	small peak	

(d) $MnPS_3$

Calculated Energy (eV)	Features	Assignment
2.1	shoulder	$Mn^+ 3d_2$ →
3.3	peak	Mn^+ 4s,4p
4.9	small peak	S 3p →
5.9	peak	Lower conduction
6.5	peak	bands
8.4	peak	$Mn^+ 3d_1$ →
8.9	shoulder	Mn^+ 4s,4p
10.3	peak	Lower S 3p →
10.8	peak	
13.7-14.4	shoulder	Conduction bands
17.2	small peak	
19.4	small peak	
21.1	small peak	S 3s, P 3s →
22.0	small peak	
23.9	small peak	
24.5	small peak	Conduction bands
25.3	small peak	
26.4	small peak	
29.4	small peak	

Table 5-1.

The experimentally observed band gaps(after ref.21) and magnetic moments of transition metals(after ref.1) for MPS_3 family. The calculated results are also listed.

Compound		$MnPS_3$	$FePS_3$	$NiPS_3$	$ZnPS_3$
Band gap (eV)	Experimental	3.0	1.5	1.6	3.4
	Calculated	1.7	0.0	0.5	2.0
Magnetic moment (μ_B)	Experimental	5.98	4.94	3.9	0
	Calculated	4.66	3.95	1.03	0

Table 5-2.

The sizes of the exchange splitting (Δ_S) and the ligand field splitting (Δ_L) of the transition metal 3d states. The calculated spin-polarizations of the transition metals are also listed.

Compound	$MnPS_3$	$FePS_3$	$NiPS_3$	$ZnPS_3$
Δ_S(eV)	12.3	7.7	2.0	0
Δ_L(eV)	3.9	5.1	3.5	1.1
Spin-polarization(μ_B)	4.66	3.95	1.03	0